Dissertation:

Investigation into the use of a novel respiratory monitor for gated radiotherapy of lung tumours

Thesis submitted in accordance with the requirements of the University of Liverpool for the degree of Doctor in Philosophy

By:
Tat Ming Chow, M.S.
Department of Physics, University of Liverpool, UK
Department of Physics, Clatterbridge Centre for Oncology, UK

Advisors:
Philip Mayles, Ph.D,
Head of Physics, Clatterbridge Centre for Oncology, UK
Alan Nahum, Ph.D,
Visiting Professor, Department of Physics, University of Liverpool, UK
Research Physicist, Clatterbridge Centre for Oncology, UK
Paul Nolan, Ph.D,
Professor, Department of Physics, University of Liverpool, UK

March 2010

Abstract:

Lung cancer is the leading cause of death through malignant neoplasms for men and women in the United Kingdom. Respiratory motion complicates thoracic radiotherapy during imaging and radiation delivery. Current lung-tumour radiotherapy yields poor outcomes. These outcomes would be improved if the dose to the tumour could be increased. One of the reasons why this is currently difficult or impossible is because large margins have to be added to the tumour to ensure that the tumour receives the full dose even if it moves due to respiration. These large margins mean large volumes of normal lung are irradiated, which limits the amount by which the tumour dose can be increased. Several motion compensation techniques have been developed to reduce the margins. These techniques reduce the doses to normal tissues, thereby reducing treatment toxicity and allowing dose escalation to the tumour. One of the techniques is Gated radiotherapy (Gating) in which the radiation beam is turned ON and OFF depending on the part of the breathing cycle the patient is in.

The Department of Clinical Engineering at the Royal Liverpool and Broadgreen University Hospital has developed the Liverpool Respiratory Rate Meter. It is a battery-powered, hand-held instrument which displays the respiratory rate of a patient. In this project, the device has been further developed and adapted for respiratory gating purposes. The applications of the developed system in gated radiotherapy were studied.

The impact of audio coaching was investigated by analysing the breathing samples of 9healthy volunteers using audio coaching. It was found that audio coaching increased the amplitude of breathing in most of the volunteers. Despite this, audio coaching reduced the irregularity in most of the subjects.

12 patient respiratory motion traces, each of them 30 seconds in length, were collected from 5 lung cancer patients at Clatterbridge Centre for Oncology. The Experimental Respiratory Monitor (ERM) was compared with a commercial system the real-time position management (RPM) system[1]) in terms of the synchronisation of the gating signal with tumour movement visible on fluoroscopy. For amplitude gating, baseline drift of the ERM was a limiting factor which made it unsuitable for use in controlling gating, if the baseline of the tumour motion drifts by a large amount.

---

[1] Varian Medical Systems, Palo Alto, CA

From the fluoroscopy study, it was shown that the performance of the ERM in amplitude gating mode was worse than that of the commercial system because the magnitude of the respiratory motion is not precisely represented by the ERM signal. As an alternative to amplitude gating, phase gating could be used to trigger the gating signal. The use of the Extended Kalman Filter (EKF) and Auto-correlation algorithm to derive a phase gating signal was investigated with the aim of improving the gating performance of the ERM.

Due to the systematic phase lag between the respiratory signals and the target motion as well as the control delay between the acquisition and control system, a number of prediction algorithms (Neural Networks, Adaptive linear prediction, Neural Fuzzy Systems and Extended Kalman Filter) have been evaluated. It has been shown that, Adaptive linear prediction was preferred. By applying predictive gating to the datasets of the fluoroscopy study, it has been shown that the residual motion was reduced by a certain amount in most of the datasets in amplitude gating.

Acknowledgements:

I would like to thank Dr. Philip Mayles & Dr Alan Nahum, my advisors, have truly been a source of inspiration. With their constant encouragement, support and fruitful discussions in past 4 years, I finally reach the state of writing the acknowledgements!

This paper would not have been possible without the constant support of my parents, friends and fellow schoolmates for their patience and encouragement.

Stephen Elmer, Peter Pryce, Alison Scott and Helen Mayles have provided assistance in numerous ways which helped to make this investigation successful.

I want to express my gratitude to Dr John Litter, Angela Heaton for coordinating the experiments for this project.

I wish to thank Sue Nixon for her administrative support. Thanks to Clatterbridge Centre for Oncology for the facilities to support this investigation.

Thanks to all my friends in Liverpool, Hong Kong Taiwan and the United States for their encouragement, concern and support (especially at the time of writing up this thesis).

Finally, thanks to the many friends (too numerous to mention) who I met in the physics Department and elsewhere in the Institute.

Abbreviations:

ERM	Experimental respiratory Monitor
RRM	Respiration Rate Monitor
RPM	Varian Real-time Position Management
EOI	End of Inhale
EOE	End of Exhale
DFT	Discrete Fourier Transform
stdev, SD	standard deviation
AWA	Adaptive Window Approach
AP	Anterior-Posterior
AV	Audio Video (usually for describing Coaching)
RMS	Root Mean Square values
rRMS	Relative Root Mean Square values (related to the Root Mean Square value of Total motion)
RMSE	Root Mean Square Errors
nRMSE	Normalized Root Mean Square Errors
%DC	Percentage duty cycle, eg: 10%DC. 20%DC, etc.
LINAC	Linear accelerator
GTV	Gross Tumour Volume
PTV	Planning Target Volume
CTV	Clinical Target Volume
ITV	Internal Target Volume

For all the respiratory plots presented in this document, local maxima always represent the End of Inhale, while local minima always represent the End of Exhale.

Contents

List of Figures:

List of Tables:

1. Introduction

1.1. Background

This project is motivated by the need to improve lung cancer radiotherapy, so it is appropriate to begin with the challenges faced.

1.1.1. Lung cancer incidence, Lung Cancer survival rate

According to the statistics report of Cancer Research UK, there were about 37000 new cases of lung cancer in 2003 in the UK (Lung Cancer and Smoking - UK 2007). It is the most common cancer in the world with each year approximately 1.4 million people diagnosed with lung cancer and it accounts for 12% of all types of cancers. It is also the most common cause of death from cancer, accounting for 18% of all deaths from cancer worldwide (Parkin *et al* 1999).

Lung cancers fall into two main categories: around 20% are small cell lung cancers (SCLC) and the remainder are non-small cell lung cancers (NSCLC). The main types of NSCLC are squamous cell carcinoma, adenocarcinoma and large cell carcinoma, accounting for approximately 35%, 27% and 10% of all lung cancer cases respectively in the UK (National Institute for Clinical Excellence 2005).

1.1.2. The treatment of different types of lung cancer

1.1.2.1. Treatment of Non-Small Cell Lung Cancer (NSCLC)

Surgery is the main curative treatment for NSCLC and early assessment of the patient to see if the tumour is operable is essential. Only 20-30% of patients may be eligible for radical surgery (Tackling cancer in England 2004).Occasionally radiotherapy with radical intent is used instead of surgery to treat local disease. The definitive treatment for local operable disease has traditionally been surgery which is potentially able to eradicate the tumour completely. The reason for treatment failure, however, is often not the local treatment but rather the spread of the tumour to other sites. For inoperable patients radiotherapy can offer a satisfactory alternative to surgery, but its efficacy is limited by the inability to deliver a curative dose

1.1.2.2. Treatment of Small Cell Lung cancer (SCLC)

SCLC tumours progress rapidly and untreated patients survive on average for less than three months from the time of diagnosis. (Lung Cancer and Smoking - UK 2007)Chemotherapy is the mainstay of treatment: radical surgery is rarely an option due to the systemic nature of the disease. Although radiotherapy reduces the risk of local recurrence, the patient frequently dies from metastatic disease. To attempt to reduce the risk of metastasis, prophylactic cranial irradiation is sometimes used for patients with advanced disease who have a high risk of brain metastases (Slotman *et al* 2007) and chemotherapy is also used to reduce metastatic spread. Where cure is not possible radiotherapy can help to control symptoms. The 5-year survival for patients with SCLC is about 5% (Minna & Schiller 2008).

1.1.2.3. The use of radiotherapy in treating lung cancer

Radiotherapy is used for patients for whom surgery is too dangerous or who have tumour(s) in a location which is difficult for surgeons to reach. For some stage 3 lung cancers where the cancer has spread locally (eg: into chest wall or diaphragm) and the tumour is still small, the clinician might suggest the use of radiotherapy instead of surgery. Radiotherapy is also good as palliative therapy for relieving chest symptoms such as pain and coughing and pain in bones to which the cancer has spread. There are 3 reasons for radiotherapy rather than surgery:

1. The patient is unfit for surgery (poor lung functions, serious cardiovascular disease.

2. The tumour is inaccessible.

3. The patient refuses surgery

However, recently it has been shown with Stereotactic Body Radiotherapy in which high doses are given in few fractions, radiotherapy results are similar to surgery (Onishi *et al* 2004, Nyman 2006).

1.2. Lung anatomy and respiratory physiology

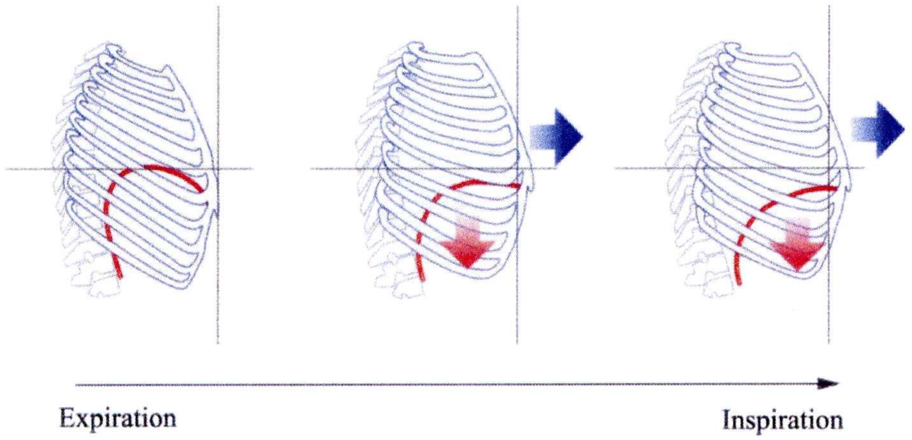

Figure 1-1A: schematic drawing of the mechanism of breathing: The above illustration shows the movement of the ribs, sternum and diaphragm in the inspiration phase of breathing. Beginning with the end of exhale on the left-hand-side figure, the diaphragm is highlighted in red and the rib cage is indicated by deep blue. The horizontal axis of the grid indicates the initial position of the diaphragm, while the vertical axis of the grid indicates the initial position of the rib cage. The red and blue arrows in the subsequent figures indicate the direction of the movement of the diaphragm and the rib cage respectively. As the breathing phase progresses towards inspiration, the diaphragm goes down and the rib cage expands to increase the volume of the lung.

1.2.1.1. Mechanism of breathing:

The primary function of the lung is to deliver oxygen to the alveoli and remove carbon dioxide. This is accomplished by the flow of gas in and out of the lungs. The differences in pressure cause by changes in lung volume, force gas in and out of the lungs in a respiration cycle.

During inhalation, the lungs expand. By Boyle's Law, the pressure of the gas in the lungs decreases below the atmospheric pressure and thus air flows into the lungs. The diaphragm (which forms the floor of the thoracic cavity) contracts to increase the superior-inferior dimension of the thoracic cavity, whilst other respiration muscles such as the internal and external intercostal muscles increase the anterior-posterior and lateral dimensions by expanding the ribcage (figure 1-1).

Unlike inspiration, expiration is a relatively passive process and muscle contraction does not necessary happen (Tortora 2006). Expiration is a result of the elastic recoil of the chest wall and lung, which have a natural tendency to spring back after they have been stretched. During expiration, both diaphragm and intercostal muscles relax with the ribcage returning to its normal position, which raises the intra-thoracic pressure and forces gas out of the lungs.

1.2.1.1.1. Lung volumes

Respiration can be described in terms of four different volumes (Ganong 2003):

1. Tidal Volume (TV) is the amount of gas inspired or expired in a normal breath.

2. Inspiratory Reserve Volume (IRV) is the amount of gas that can be inhaled by maximal effort after a normal TV.

3. Expiratory reserve volume (ERV) is the amount of air that can be exhaled by maximal effort after a normal TV.

4. Residual volume (RV) is the amount of air remaining in the lungs after a maximum expiration.

1.3. Literature review:

1.3.1. Respiratory Monitoring and compensation of respiratory motion in radiation delivery

Respiratory motion can cause problems during image acquisition and treatment planning as well as in radiation delivery when treating lung tumours.

Many studies have been performed to study lung tumour motion. (Shen *et al* 2003, Jiang *et al* 2003, Keall 2001, Hugo 2003, Hugo 2002, Bortfeld *et al* 2002,Bortfeld *et al* 2004).These studies report that tumour movement can vary between a few millimetres and several centimetres. The effect of respiration motion on imaging is both to generate artefacts and to make the position of the tumour uncertain. Standard imaging methods do not accurately delineate the extent of tumour movement (Shimizu *et al* 2001, Vedam *et al* 2003, van Herk *et al*2000, Ritchie *et al* 1994, Ford *et al* 2003, Balter 1996, Giraud *et al* 2002). In treatment planning, a margin is needed to ensure adequate coverage of the tumour(the margin of the tumour displacement in addition to the clinical target volume (CTV)) for treatment delivery. The additional margin added to the CTV forms the Planning Target Volume (PTV). The development of 4D-CT has made it possible to define the volume of tumour excursion during a respiration cycle on the CT images relating to a patient's fixed anatomic landmarks. This volume is considered as the internal target volume (ITV) as defined by the International Commission on Radiation Units and Measurements (ICRU) report 62 (1999). Adding standardized margins to account for respiratory motion may increase the volume of healthy lungs receiving high radiation dose. There is a direct correlation between the radiation dose and the probability of achieving local control of the tumour. However, the maximum dose that can be delivered to the tumour is limited by the tolerance of the normal tissues that surround it. Therefore, limiting respiratory motion can potentially allow the dose to the tumour to be increased without increasing damage to normal tissues. There are several techniques that are being used to account for respiration motion.

Table 1-1: Magnitude of Lung Tumour motion due to respiration.

Studies	**Modality**	**Tumour Motion (mm)**	
Shirato et al 2000	Fluoroscopy	8.3±1.2	(peak to peak)
Ford *et al* 2002	Fluoroscopy & CT	13.5-19.9	(90% excursion)
Vedam *et al* 2003	Fluoroscopy	2.4-6.0	(SD)
Starkschall *et al* 2004	CT	5.1-17.6	(peak to peak)
Hoisak *et al* 2004	Fluoroscopy	1.1-27.6	(peak to peak)
Tsunashima *et al* 2004	Biplane digital radiography	2.2 to 14.7	(peak to peak)
Ahn *et al* 2004	Fluoroscopy	9.7-18.2	(peak to peak)

Respiratory motion has been measured using various imaging techniques such as ultrasound, fluoroscopy, CT and MRI (Ford *et al* 2002, Shen *et al* 2003, Jiang *et al* 2003, Keall *et al*2001, Hugo *et al*2003, Hugo *et al*2002, Bortfeld *et al* 2002, Bortfeld *et al*2004). With these images, significant differences were noted between quiet (shallow) breathing and deep breathing. Table 1-1 lists a number of studies from which we may conclude that the range of lung tumour motion is less than 30 mm.

Margins are added to the CTV for variations in tissue position, size and shape as well as inter and intra-fraction variation in patient position and beam position to form the Planning Target Volume (Antolak *et al* 1999 Engelsman *et al* 2005).Typical margins for lung treatments are of the order of 1–2 cm (Hanley *et al* 1999).

Most institutions do not have techniques for reducing respiratory motion, so larger margins are used to account for the tumour motion due to respiration motion. Larger margins account for the variations and uncertainties and prevent under dosage to the tumour. However, larger margins also result in an increased volume of normal tissue irradiation.

There are various approaches to deal with tumour motion, such as, gating (to irradiate the tumour when it is within a pre-defined spatial location) (Kubo and Hill 1996, Keall *et al* 2001), beam tracking (a robotic mechanism to adjust and align the beam with the tumour in real time) (Schweikard *et al* 2000, Neicu et al

2003) and passively restricting the respiratory motion (Stromberg *et al* 2000, Remouchamps *et al* 2003, Hanley *et al* 1999).

1.3.2. Respiratory Gating

Respiratory gating is a method that is used to limit the effect of respiratory motion during imaging and radiation delivery without interruption of the patient's breathing.

The gating signal is used to trigger the radiation beam. The period that the radiation beam is enabled is called the *gating window*. The position and duration of the gating window is determined by using external surrogates or internal markers to monitor the target position. For external surrogates, gating can be delivered by two different techniques: amplitude gating or phase gating. In amplitude gating, the radiation beam is enabled whenever the respiration signal is within a pre-defined window of relative positions. For phase gating, a phase signal is calculated by an algorithm from the respiration signal. The radiation beam is activated when the phase of the respiration signal is within a pre-defined phase window. The ratio of the duration of the gating window to the overall treatment time is called the duty cycle. In most cases the tumour is not completely static in the gating window and this movement when the beam is on is referred to as "residual motion". In general, the residual motion will increase with the duty cycle.

Gating has the advantage, compared to techniques involving the restriction of the range of respiration, that lung cancer patients who have reduced lung function can breathe freely without holding their breath.

When a surrogate is used to monitor breathing for gating, the tumour position is inferred by the breathing signal of the surrogate. The correlation between the tumour and the surrogate in a simulation session is assumed to remain the same in future treatment sessions. Therefore, the tumour and the surrogate must be monitored long enough to ensure they are reliably synchronized and detect possible drifts and long-term variations. Monitoring should also be repeated throughout the course of treatment.

Gating modalities: devices/systems for monitoring breathing

1.3.2.1. Monitoring of chest wall and abdominal movement:

This technique relies on the repeatability of the correlation between the tumour location and the external surface, an assumption that has been investigated in several studies (Vedam *et al*2003, Hoisak *et al*2004, Tsunashima *et al*2004, Koch *et al*2004, Ahn *et al*2004).Vedam *et al.* (2003) analysed 63 breathing signals from 8 volunteers and found that external motion (abdominal wall Motion) was mostly correlated to diaphragm motion regardless of session and coaching method. It was found that the correlation coefficient between the external motion and the tumour varies from patient to patient.

The Varian Real-time Position Management (RPM) system has been widely discussed in publications. The system involves placing an Infrared reflective marker on the chest wall or abdomen. The reflective marker is illuminated by infrared emitting diodes and the resulting images are captured by a camera and processed by a desktop computer, resulting in a breathing trace (Mageras *et al* 2001, Ford *et al* 2002). Abdomen surface displacements do not always correlate with tumour position. Phase shift or delay and baseline drift have been observed (Shimizu *et al* 2001, Mageras *et al* 2001).

1.3.2.2. Spirometer:

Zhang *et al* 2003 presented using a Bernoulli-type Spirometer for breath monitoring. The spirometer was a bi-directional differential pressure sensor that converted the flow into a pressure signal. This signal was then converted to a voltage, digitized to a reading value, and transferred to a control computer. They stated that a spirometer correlated to the target position by measuring lung volume changes and had less setup variation. A nose clamp and a mouth piece were used to ensure the accuracy of air-flow measurement. However, studies of respiratory physiology have shown that the nose clamp and mouth piece increase the tidal volume of breathing (Gilbert *et al* 1972, Askanazi 1980, and Tobin 1983a). Tidal volume has a direct relationship with the motion of the tissues of the lung.

1.3.2.3. Temperature sensor:

Temperature sensors, usually being placed just below the nostrils, monitor the temperature of the gas flowing in and out of the nose. The temperature signal of the sensor corresponds to the room temperature when inhaling and the lung temperature when exhaling. Kubo & Hill (1996) presented the technical aspects of using two types of temperature sensor (thermocouple and thermistor) for respiratory monitoring in gated radiotherapy. It was found that both of these correlated well with the pneumotachograph and strain gauge. For patient comfort, temperature sensors are preferred over a pneumotachograph. A thermocouple has also been used as a breathing monitor for 4D CT reconstruction (Wolthaus *et al* 2008).

1.3.2.4. Strain Gage

A strain gauge attached to a band wrapped around the patient's chest can be used to detect the abdominal surface tension change (Okumura 1994, Minohara 2000). Kubo& Hill(1996) analyzed various sensor systems to monitor respiratory motion to obtain a surrogate for motion information to use as a gating signal. The strain gauge was described as reliable and inexpensive and proved to be more comfortable than the pneumotachograph. Special caution on the tightness of the tension belt is needed. A tight belt would restrict the thorax movement, while a loose belt has a tendency to move (or slip) around the thorax, resulting in in-accurate measurement (Mazika & Swan 2007).

1.3.2.5. Internal surrogate: Image guidance technique for gating

Shimizu *et al*2001, Shirato *et al*2000 & 2003 , Seppenwoolde *et al*2002, Shirato *et al*1999 have described the use of internal gold markers to gate the radiation beam. The markers are tracked using an x-ray system 30 times per second. When the markers are within a predetermined location, as determined from the x-ray imaging system, the linear accelerator is triggered to irradiate the tumour.

Since the tumour may not be easily identified and tracked under fluoroscopy, gold seed markers are inserted into the tumour, to increase the accuracy of tracking the tumour. For example, the Cyberknife system uses two orthogonal x-ray images from x-ray tubes mounted in the floor of the room. In order to identify individual fiducial markers, it is important that the markers are not placed superimposed on each other in 45° oblique views (Kothary *et al* 2009).To achieve this two skin entry sites may be needed.

Shirato *et al* 2000 measured the dose rates of two diagnostic X-ray tubes at 120 kV with a pulse width of 4 ms with thermoluminescence dosimeters. The dose rates were 10.8 mGy/min at the entrance and 0.8 mGy/min at the exit. Assuming 2-min diagnostic exposure for a daily irradiation of 2 Gy in 40% duty cycle, the additional X-ray dose, due to real-time tracking, ranges from 0.208 to 21.48×10^{-3} Gy. This amount corresponds with 0.02–2% of the total prescribed dose. The extra dose was small compared to the dose to the PTV. However, the highest dose occurs at the skin surface, which is usually not part of the PTV.

Localization with a fiducial marker directly within lung tumours is considered an accurate way of aiding in gated radiotherapy because it directly marks the tumour position (Shimizu *et al* 2001, Shirato *et al* 2006). The placement of fiducials within lung tumours can be achieved either transcutaneously (under either fluoroscopic or CT guidance) or transbronchially through bronchoscopy-based approaches.

The main disadvantage of transcutaneous approaches is the risk of pneumothorax, estimated to be in the 20–30% range, similar to the pneumothorax rate associated with transcutaneous needle biopsies of lung lesions (Cox *et al* 1999, Fish *et al* 2006).Various studies have shown needle biopsy induced pneumothorax rates between 8% and 38% (Topal and Ediz 2003, Geraghty *et al* 2003, Laurent *et al* 2000). These results make many clinicians reluctant to perform marker implantation in the lung. However, the risk of pneumothorax using the transbronchial approach is negligible compared to the transcutaneous approach (Kupelian *et al* 2007).Most of the gold markers remained in place during the treatment (Imura *et al* 2005). However, for certain types of tumours, it was difficult to keep the gold markers in place throughout the treatment period (Harada *et al* 2002). The marker moved from the inserted position within 24 hours in four tumours; (two were central tumours and two were peripheral tumours in the left superior segment)and after a week in one patient with a central tumour. Hence, implanted markers are not feasible for all patients and the patient must be able to tolerate the implantation procedure.

Berbeco *et al* (2005b) have suggested using the fluoroscopic images for gating based on motion-enhanced tumour images of the lungs without implanted markers. At the end of inspiration, the lung fills with air. Thus, the radiological path-length through the lung shortens (in contrast to End of expiration with long path-length), giving brighter fluoroscopic intensities. Hence, the temporal change in intensity represents the breathing cycle and was used to trigger the radiation beam when the target was within the desired location.

1.3.3. Respiratory Synchronized Radiotherapy/Real-time tumour-tracking

The principle of respiratory synchronized radiotherapy is to follow the tumour with the radiation beam (Keall *et al* 2001, Schweikard *et al* 2000).In tumour motion synchronization, the position of the tumour is detected by either visualization of the internal structure or implanted markers. In some of the cases, a lung tumour is possible to detect directly in fluoroscopic images acquired simultaneously. However, most lung tumours are not easily visible (by clinician or computer vision) under fluoroscopic imaging. In such cases, implanted fiducial markers (in or near the tumour) are used to track the position of the tumour. Due to the high atomic number of gold, gold fiducial markers were utilized in the study of Murphy *et al* (2000) and Shirato *et al (*2000), such that the dose to the fluoroscopy imaging field can be reduced.

To reduce the irradiation of healthy tissue surrounding the target volume, a miniature implantable radiofrequency coil that can be tracked electromagnetically in three dimensions from outside the patient has been used (Seiler *et al.* 2000, Balter *et al* 2005). The electromagnetic approach could provide an alternative to the use of radiological imaging to track the tumour position.

In real-time tumour tracking, the treatment beam is on throughout the respiratory cycle and unlike gated treatments, the treatment time is not increased.

This technique may reduce NTCP by reducing the internal margin and increase tumour control by dose escalation.

There is still a considerable amount of software and hardware investment required for respiration-synchronized radiotherapy. The treatment planning system needs to account for the dosimetry regarding the changing lung volume, because the normal treatment-planning imaging study used to calculate the dosimetry is in one static configuration. The anatomy and the air volume in the lung are continually changing during the treatment session. Hence, the relative positions of tumour, normal tissue, and critical structures change. These position changes affect the attenuation of the treatment beam and affect the dose distribution of the whole treatment plan.

1.3.4. Active control of respiration motion

There are two benefits of using active control techniques:

- The target is immobilized so that diaphragm motion and position variability can be reduced.
- Increasing the volume of the lungs (in Inspiration Breath Hold) to reduce the fractional amount of normal tissue being irradiated (Stromberg *et al* 2000, Remouchamps *et al* 2003, Hanley *et al* 1999). This potentially reduces normal tissue complication probability (NTCP). These techniques may therefore help in dose-escalation radiation treatments for lung cancer patients.

1.3.4.1. Deep Inspiration Breath Hold

Deep Inspiration Breath Hold (DIBH) is a technique trying to reproduce the state of maximum inhalation (Remouchamps *et al* 2003, Hanley *et al* 1999, Mah *et al* 2000). The manoeuvre begins with the patient in quiet tidal breathing, followed by slow deep inspiration and slow deep expiration and then another slow deep inspiration to maximal inspiration level and breath hold.

Several studies have been performed using DIBH to reduce the movement of lung tumours due to respiration. Hanley *et al* 1999 compared the treatment plan for DIBH and free breathing. The volume of lung receiving more than 25 Gy was reduced by 30% while respiration gating only reduced the volume by 18% compared to no intervention. DIBH could also reduce the density of the lung by 26% on average. Hence, there could be a potential to decrease the dose of the normal tissue of the lungs.

Target immobilization and expanded lung volume (reduced density) are the important features of the breath hold technique. Increasing lung volume will reduce the fractional amount of normal tissue being irradiated which should reduce normal tissue complications.

1.3.4.2. Voluntary Breath Hold (Subject Initiated Breath-Hold)

In Voluntary Breath Hold, the patient plays the role of the sensor, detector and beam controller. The patient holds the breath at a predetermined specific position in the breathing cycle while at the same time presses a notification button. The therapist then activates the treatment beam. When the prescribed dose has been delivered, the treatment bream stops. The treatment beam can also be stopped by the patient or the therapist to interrupt the treatment. The technique was verified by a fluoroscopy study by Kimura *et al (*2004). Kimura *et al* used the voluntary breath-hold technique with a spirometer to evaluate the reproducibility of organ position by using CT scans. The volunteer was asked to hold his breath at end-inspiration or end-expiration, whichever felt more comfortable. The conclusion of this study was that voluntary breath hold has relatively good interfraction and intrafraction reproducibility, especially for end-expiration subjects. Intrafraction reproducibility of tumour position in the cranio-caudal direction was 4.0-3.5 mm at the end-inspiration phase and 2.2-2.0 mm at the end-expiration phase.

1.3.4.3. Active Breathing Control

An ABC device monitors the flow of breath and uses valves to control the inspiration and expiration independently. The clinicians can specify the flow direction and the lung volume for closing the valves and the duration of breath hold. There have been several published studies on the use of this technique to treat lung (Cheung *et al* 2003, Koshani *et al* 2006, Wilson *et al* 2003), breast cancer (Frazier *et al* 2004) and Hodgkin's disease (Stromberg *et al* 2000).When training for ABC, the patient has a visual feedback of the lung volume and the level of intended breath hold (Wong *et al* 1999). The patient is notified when the ABC device will be enabled and the valve closes. The patient must be comfortable with holding his or her breath for the period during which the valve is closed, as well as being able to cope with repeated breath holds.

1.3.4.4. Breathhold

Techniques such as ABC and DIBH might be demanding for the elderly patient population or those having reduced lung function. Moreover, patients who cannot follow instructions are unsuitable for this technique (Rosenzweig *et al* 2000).

Voluntary breath hold tries to solve this problem by letting the patient choose the time to hold their breath. However, in the study of Barnes *et al (*2001), 2 of the 10 subjects were observed to have continuous diaphragm motion during voluntary breath hold, even though they believed they were holding their breath. This mode of treatment relies heavily on the patient's ability to understand and perform a reproducible breath hold, maintain it for at least 10 s, and simultaneously operate the hand-held switch.

1.3.4.5. Forced Abdominal Compression

Abdominal compression can be used to limit the motion of the diaphragm. The patient is placed in a body frame (or three sided box). The frame allows a plate on a threaded pillar to be screwed down so as to compress the abdomen. Patient immobilisation is improved by the use of a compression device such as a metal plate (Wulf *et al* 2000, Negoro *et al* 2001). The frame is comprised of three parts: a body shell, laser markers and a small abdominal pressing plate. The body shell is made up of a rigid frame and a flexible part called a vacuum pillow, which when evacuated maintained the patient's body contour and became rigid enough to support the patient. A small abdominal plate was pressed on the patient's upper abdomen to suppress large movements of the diaphragm and to reduce the tumour's movement during respiration. Negoro *et al.* (2001) studied this technique with 18 lung cancer patients. With free breathing, they found that ten of the patients had motion between 8 and 20 mm, which was reduced to 2 to 11 mm using abdominal compression. Motion was reduced while maintaining normal respiration. This technique also increased the accuracy of daily setup(with standard deviations of field placement errors of 3.5 mm in longitudinal, 2.2 mm in the anterior–posterior and 3.9 mm in the lateral directions (Wulf *et al* 2000) One difficulty encountered while using the abdominal compression technique was the inability to detect the patient's rotation along the body axis and not all patients can tolerate it.

1.3.5. Variable nature of respiration

Inter-cycle (Breath-to-breath) variations can be represented by tidal volume and the inspiratory/expiratory durations. Sometimes correlation is established between tidal volume and the inspiratory/expiratory durations (known as correlated variations). (Bruce *et al* 1996, Bechbache *et al* 1979 and Kay 1975) They can also be affected by uncorrelated random variations (known as white noise). The breathing pattern is also affected by periodic oscillations which aim to regulate the oxygen supply and non-periodic fluctuations (eg: psychological and environmental changes).These variations can be the result of a number of factors: such as central neural mechanisms, anatomic variabilities, genetic variation, pulmonary afferent activities and/or chemoreflex mechanisms.

Shea *et al* 1992 demonstrated that the forebrain activity (related to sleep and awakeness) or comfort level (related to the patients comfort) affect breathing patterns in diseased patients. The study utilized a respiratory inductance plethysmography (RIP) device to study breathing-pattern differences between patients and the possible factors of the differences.RIP is a device used to measure changes in chest and/or abdominal volume.[2]The study was performed on 50 healthy volunteers and measured by RIP twice a day on two consecutive days. It was found that different people breathe in different ways under defined conditions and even in the absence of behavioural or forebrain influences (i.e., during sleep), the differences persist. The study of 9 pairs of twins showed that the twins breathe with similar patterns. This supports the conclusion that there is a possible genetic influence on breathing pattern.

---

[2] It works by putting a loop of wire around the chest/abdomen of the subject. A current then applied through the loop of wire generates a magnetic field normal to the orientation of the loop. A change in the area enclosed by the loop creates an opposing current within the loop directly proportional to the change in the area. (Mazeika & Swanson 2007)

Tobin *et al.* 1983a measured the breathing of 47 young (ageless than 50) and 18 old (age greater than 60) normal subjects utilizing respiratory inductive plethysmography. It was observed that rhythm was more irregular for old subjects.

A similar study by Tobin *et al.* 1983b compared the breathing of normal subjects, asymptomatic smokers, asymptomatic and symptomatic asthmatic patients and patients with chronic obstructive pulmonary disease, restrictive lung disease and pulmonary hypertension. It was shown that diseased subjects have larger variations in breathing pattern components than normal subjects. Lung cancer patients have impaired lung function (or part of their lung was removed by surgery) and it is therefore likely that such patients have larger breathing pattern variations.

1.4. How the Experimental Respiratory Monitor Works

1.4.1. Introduction to the Experimental Respiratory Monitor

The Department of Clinical Engineering at the RLUBH has developed the Liverpool Respiratory Rate Meter (RRM). It (Figure1-2) is a battery-powered, hand-held instrument which displays the respiratory rate (in the unit of breaths per second) of a patient sampled over the previous 30 seconds. The system produces a signal related to the patient's instantaneous state of respiration from which is derived the respiration rate displayed on the LCD monitor. In this project, the device was further developed and adapted it for respiratory gating proposes. This section described information of the original design of the RRM. It covers the physical aspects, electronic design and software programs involved in obtaining the breathing signal.

Figure 1-2: The Respirate, a respiration rate measuring device adopted as a respiration gating device.

1.4.2. Electronic design of Experimental Respiratory Monitor device:

The device is composed of a transducer (Figure 1-3), Analog to Digital converters, a Microcontroller, an LCD display and a Bluetooth port(Figure1-4). The transducer of the RRM is a sensory device attached to the air mask to measure the temperature of the mask cavity. It is made of a piece of Piezo-electric film and a signal amplifier. Piezo-electric film is sensitive to both temperature change and mechanical movement/vibration. The breath transducer is based on a rigid piezo-ceramic film acting as a *change-in-temperature* detector located in the side-wall orifice of a standard supplementary oxygen face mask. The respiratory rate is displayed on an LCD. The Analog to Digital converter (ADC) is built into the microcontroller for digitising the amplified piezo signal. A microcontroller with built-in timer is used to control the timing of ADC sampling and handle the Bluetooth communication.

The microcontroller in the main compartment, is a Programmable Interface Controller made by Microchip Technology, utilizes a 4MHz crystal. The system is powered by a 9V battery. It has a port for connecting the transducer, a speaker and a LCD screen to output the internal state and an on/off switch. The serial-port version has an integrated circuit (IC) chip to handle RS232 communication, while the Bluetooth version has a Bluetooth component with the IC, antenna and a reset switch. The transducer compartment houses a Piezo sensor, a low-pass filter circuit (for Anti-aliasing of the analogue to digital sampling) and an amplification circuit. The LCD displays the current breathing rate and the battery state.

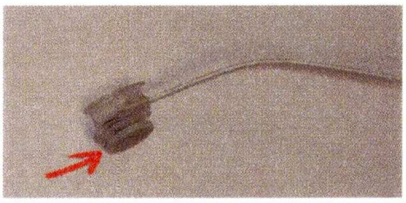

Figure 1-3: The transducer of the RRM which is connected to a port located on the upper face of the orange box (Figure 1-2).

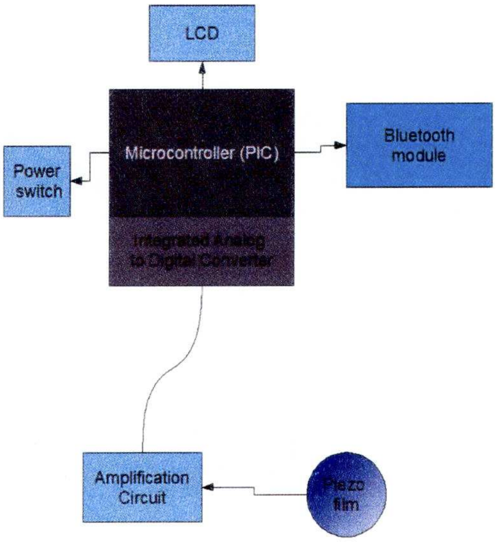

Figure 1-4: System Diagram of Electronic Design of RRM

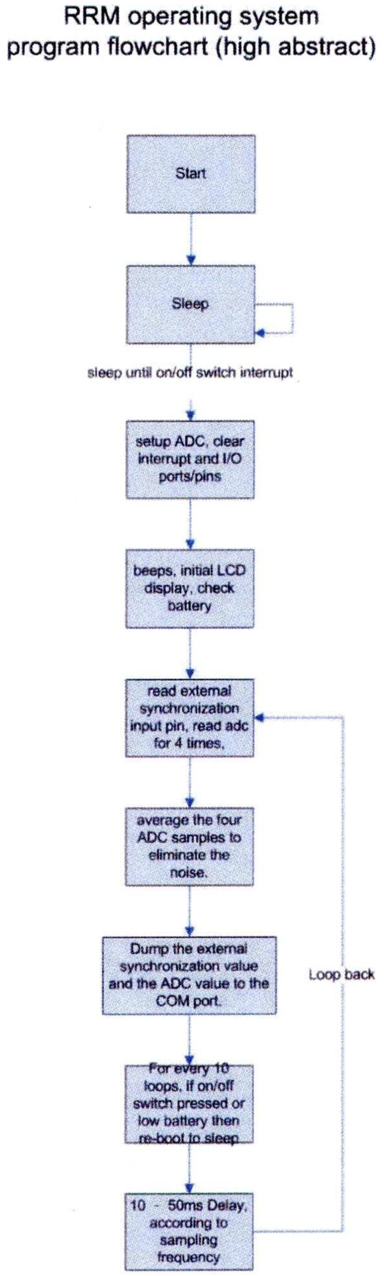

Figure 1-5: Flowchart of the Operation System of the RRM.

1.4.3. Operating systems of the Experimental Respiratory Monitor device:

The operating system (OS) of the RRM is written in micro-C and then compiled into binary code of the specific PIC. On supplying the circuit broad with electricity, the operating system starts to run (Figure 1-05). When the system starts, it goes into "sleep" mode. If the user presses the power button, the program wakes up, clears the registers, initialises the timer, and sets up the peripherals and I/O pins. After system initialization, the OS sends a pulse to the buzzer to indicate that it has been switched on and then displays a start-up pattern on the LCD display. The OS then reads the external synchronization input and then reads the ADC for 4 times to average the four values to eliminate noise. The data are then transmitted through the Bluetooth port to a PC. The OS then will go into an infinite loop of "reading and transmitting" until the battery runs out or the on/off switch is pressed again.

1.4.4. The transducer

The transducer of the ERM is a sensory device attached to the air mask to measure the temperature of the mask cavity. The temperature sensor is made of piezo-ceramic film.

1.4.5. Piezoelectric ceramics

When a piece of piezoelectric ceramics is stressed mechanically by a force, it generates an electric charge. If the electrodes are not short-circuited, a voltage associated with the charge appears. Mechanical compression or tension on a poled piezoelectric ceramic element changes the dipole moment, creating a voltage. (figure1-6).

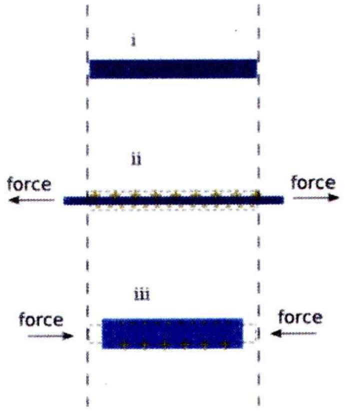

Figure 1-6i,ii,iii: compression force(iii) and tension force(ii) change the thickness of the piezo ceramic. Net charges are formed on the top and bottom plane.

The ceramic element converts the mechanical energy of compression or tension into electrical energy. Values for compressive stress and the voltage generated by applying stress to a piezoelectric ceramic element are linearly proportional to the compressive stress up to a material-specific stress limit. The piezo ceramic was also been use for the production and detection of sound in microphones and speakers, generation of high voltages in lighters.

The pyroelectric effect of the piezo ceramic dominates the signal response of the detection. When hot air blows through the detector, it absorbs thermal energy, which raises the temperature of the material, thereby inducing an electrical signal. Piezo ceramic exhibits a current response that depends on the rate of temperature change.

1.4.5.1. Response of the piezo sensor to a thermal step function

In breath hold radiotherapy, the patients hold their breath for a few seconds. The radiation beam is on during the breath hold period. The volume of air in the lung would increase to a level and hold relatively steady for a few seconds and then back to its original level. This process is a step-up and then step-down sequence.

A thermal flux passes through the piezo sensor in the form of a step function. Initially, the element is at a uniform temperature, the net charge between the two piezo plates is zero. When it is exposed to thermal radiation in the rising edge, its front plate expands, causing a stress induced charge. As the heat flux passes through the sensor, the sensor tends to return to thermo equilibrium. Therefore, its rear(second) plate would expand and the net charge between the two films will decrease. If the duration of the heat flux is long enough (flux duration tends to infinity), the net charge will not reduce to zero because there is a charge induced by the leakage of thermal flux from the second film.

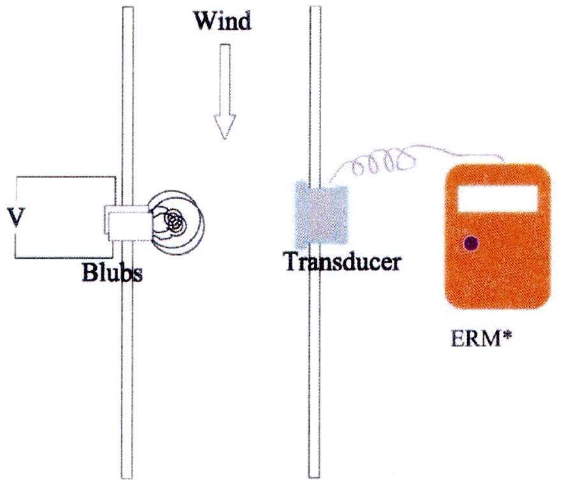

Figure 1-7: The above diagram illustrates the experimental setup of testing the response of the transducer by heat transfer through radiation. The heat was given out from the light bulbs and their brightness was controlled by a DAC. Airflow at room temperature was used to cool the setup

A light-bulb phantom was used to measure the response of the piezo electric sensor to changes in temperature. The phantom was a black box with a fan and 4 light-bulbs. The fan caused a constant flow of air at room temperature while the brightness of the light bulbs was variable. The voltage of the light-bulbs was controlled by a Digital to Analogue Converter. The transducer was placed close to the light bulbs (~3cm).

The voltage from the transducer and the light-bulbs was measured by an Analogue to Digital Converter (PICO ADC-11) and the voltage was plotted against time (represented by the number of samples) as shown figure 1-8. The sampling frequency was 50Hz.

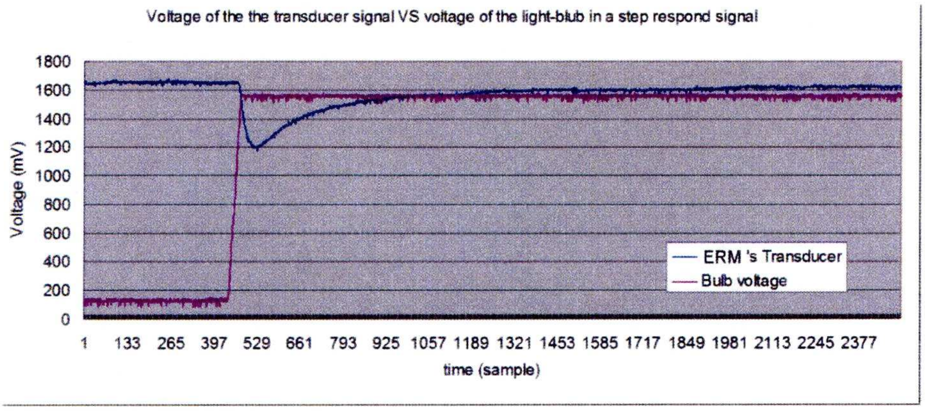

Figure 1-8: Step response of the piezo-electric transducer of the ERM.

The magenta trace is the voltage applied to the light bulbs and the dark blue trace is the voltage of the transducer. Both signals were sampled by an Analog to Digital Converter. The horizontal axis is the time measured in terms of the number of samples. There were 50 samples each second.

When the light bulb's voltage was subjected to a step change, the signal from the piezo-electric sensor drops to a certain level and then gradually rises back to its original level (figure 1-8).

The current is discharged through a load resistor connected in parallel with the piezo sensor.

1.4.6. Summary of breathing signal detection by the Experimental Respiratory Monitor device

Figure 1-9 shows how the system operates. The air flow in the air-mask creates a temperature change on the ceramic film. This leads to a net charge (and potential difference) created in the piezo film. The potential difference signal is then low-pass filtered to minimize the effect of the vibration of air flow. It is followed by power amplification and analogue to digital conversion.

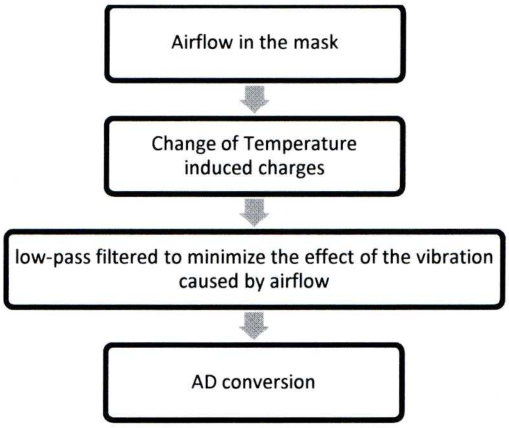

Figure 1-9: The flowchart of interaction between the airflow and the electronic devices of ERM.

1.4.7. The controlling software of the Experimental Respiratory Monitor system:

The ERM's control system and utilities are a set of tools, developed in Java[3], which handle the Bluetooth serial communications, flow control, absolute time synchronization and data logging. It also displays the input signals for visualization feedback for the operator.

The ERM sends data to a workstation in the format of "AAA,BB\n", where AAA is the reading of the transducer and BB is the respiration rate. The device works on a fixed sampling rate and does not send any time signal to the workstation. The data packets are time stamped immediately when they are received by the workstation. The program runs on a Windows XP workstation with 1.7GHz Intel processor. The sampling rate of about 10Hz is within the capability of the processor, despite the multi-tasking behaviour of the operating system. An investigation was performed to verify the transfer delay between the workstation and the device. 5 breathing signals each lasting for 2 minutes were obtained by the ERM. For all the testing data samples received, the time differences between any subsequent timestamps were within a variation of 4ms. The standard deviation of the above time differences was 1.03 ms, which was insignificant when compared to the 100ms sampling period of the device. Any data sample would be rejected if it showed a deviation larger than 100ms, which is the value of the sampling period. Hence, the connection between the ERM and the workstation was reliably synchronized.

---

[3] Sun Microsystems, Inc. Santa Clara, California

2. Development and Applications of the Experimental Respiratory Monitor (ERM)

The ERM is adapted from a respiratory rate meter. The respiratory rate meter is designed to detect the zero-crossing of the breathing signal. In order for the device to be useful for gated radiotherapy, a signal that is correlated with the movement of the moving object is required. One of the aims of this chapter is to investigate the characteristics of the sensor, the transducer (which forms an important part of the device) and the whole monitor system.

2.1. Measurements

2.1.1. How the piezo sensor responds to changes in temperature in the air mask

Figure 2-1: The bare piezo sensor

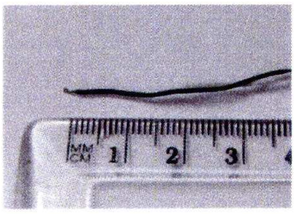

Figure 2-2: The J-type thermocouple

2.1.1.1. A bare piezo sensor

In order to measure the temperature of the piezo-electric sensor, a thermocouple was placed next to it in the mask as shown in figure 2-4.It was a J-type thermocouple calibrated in a water bath and its potential difference was found to have a linear relationship with absolute temperature in the range 20° C to 40° C range (correlation coefficient R=1).

Figure 2-3 shows the relationship between the potential difference and the temperature of the thermocouple. The piezo sensor used in this experiment was a bare piezo sensor which did not have a plastic layer protecting the piezo plate.

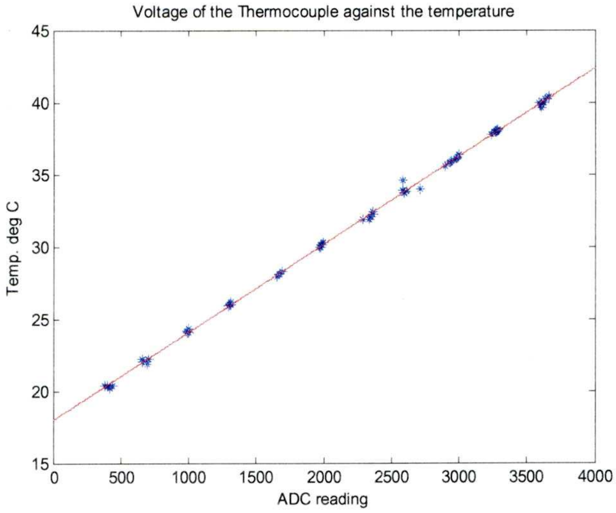

Figure 2-3: The temperature and voltage relation between the J-type thermo couple used in this experiment.

The thermocouple was calibrated in a temperature controlled water bath. The measurement of the thermocouple was amplified and sampled by an Analogue to digital converter (ADC). The ADC reading ranged from 0 to 4095, representing from 0V to 2V input range. A reading of 2000 on the horizontal axis represents about 1V potential difference measured from the output of the amplification circuit.

The thermocouple and the piezo sensor were connected to separate operational amplifier circuits.

6 breathing traces were collected from 2 healthy volunteers. They were asked to breath normally for 2 minutes. The room temperature was 25° C throughout the experiment.

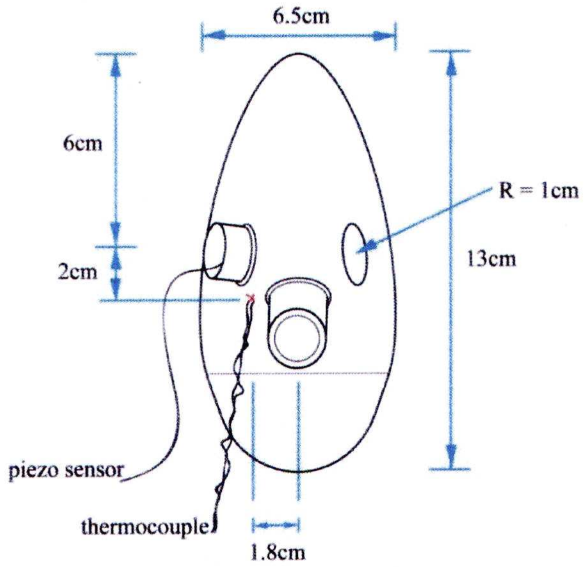

Figure 2-4: Position of the thermocouple and the piezo sensor in the air mask

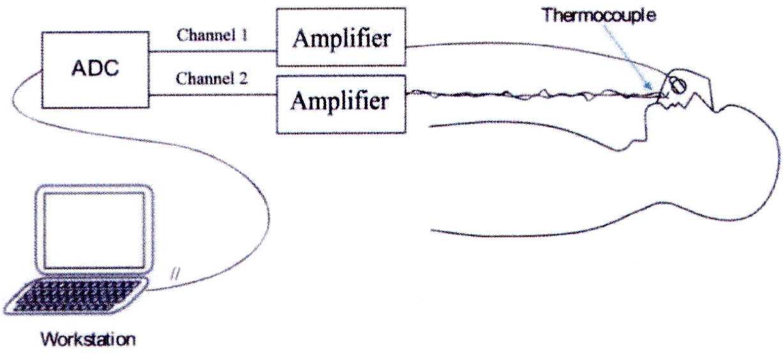

Figure 2-5: System diagram of the thermocouple and piezo sensor experiment. The thermocouple and piezo sensor were put inside the air mask. Their signals were amplified and then sampled by an analogue to digital converter.

The phase delay of every session was measured by the cross-correlation function. Then, the correlation between the thermocouple and the piezo-electric sensor (after phase shift) were measured and are shown in the table 2-1.

Table 2-1The time delay and the correlation between the thermocouple and the bare piezo sensor

		Delay of Thermocouple (s)	Correlation
Volunteer-1	**Session-1**	0.36	0.82
	Session-2	0.40	0.74
	Session-3	0.52	0.81
Volunteer-2	**Session-1**	0.36	0.90
	Session-2	0.40	0.85
	Session-3	0.48	0.89
Volunteer-3	**Session-1**	0.27	0.87
	Session-2	0.36	0.91
	Session-3	0.34	0.75
Volunteer-4	**Session-1**	0.43	0.76
	Session-2	0.46	0.83
	Session-3	0.32	0.90
	mean	0.39	0.84
	SD	0.07	0.06

The bare piezo sensor was then replaced by the transducer of the ERM (figure 2-1). The difference between the bare piezo sensor and the ERM transducer are: (1) the transducer has a protective layer of plastic to cover up the piezo plate and (2) the amplifier circuit and the low-pass filter are integrated within the transducer enclosure. The result of the time delay and the correlation between the thermocouple and the transducer are shown in Table 2-2:

Table 2-2The time delay and the correlation between the thermocouple and the transducer of the RRM

		Delay of Thermocouple (s)	**Correlation**
Volunteer-1	**Session-1**	0.40	0.81
	Session-2	0.44	0.81
	Session-3	0.48	0.79
Volunteer-2	**Session-1**	0.32	0.80
	Session-2	0.20	0.81
	Session-3	0.28	0.89
Volunteer-3	**Session-1**	0.34	0.78
	Session-2	0.37	0.81
	Session-3	0.47	0.86
Volunteer-4	**Session-1**	0.48	0.87
	Session-2	0.39	0.75
	Session-3	0.28	0.82
	mean	0.37	0.82
	SD	0.09	0.04

As it was not ethical to take x-ray images of the normal volunteers, it was not possible to relate the signals to internal organ motion. However, the above data shows that the piezo sensors (both the bare sensor and the protected sensor) respond faster to temperature change than the thermocouple. The average time lag of the thermocouple was 0.39 s (bare)and 0.37 s (protected sensor). The piezo sensors have an average of 0.84(bare) and 0.82 (protected sensor) correlation coefficient with the thermocouple.

Time delay between the thermocouple and the piezo sensor.

There has been an average of ~0.4s of lag in the thermocouple signal. One of the possible reasons for this relates to the different way of perceiving heat. The piezoelectric sensor measures the change of temperature (ΔT), while the thermocouple measures the Temperature (T). We tried to prove this relationship by differentiating the thermocouple signal, and find out the time lag. We found the average time lag of the thermocouple is then -0.03 s (bare) and 0.01 s (protected sensor). These values are zero within the experimental uncertainty.

The difference in time lag between the bare and the protected sensorare zero within the experimental uncertainty. Hence, the protective membrane has no significant effect on the piezo sensor.

The signal of the bare piezo sensor is noisy (an example is shown in figure 2-6a), but still maintains a reasonable representation of the breathing cycle. To show the correlation between the two signals, the signals of the thermocouple and the piezo sensor were filtered by low-pass filter and shifted by a time-lag value (such that their peaks match each other).

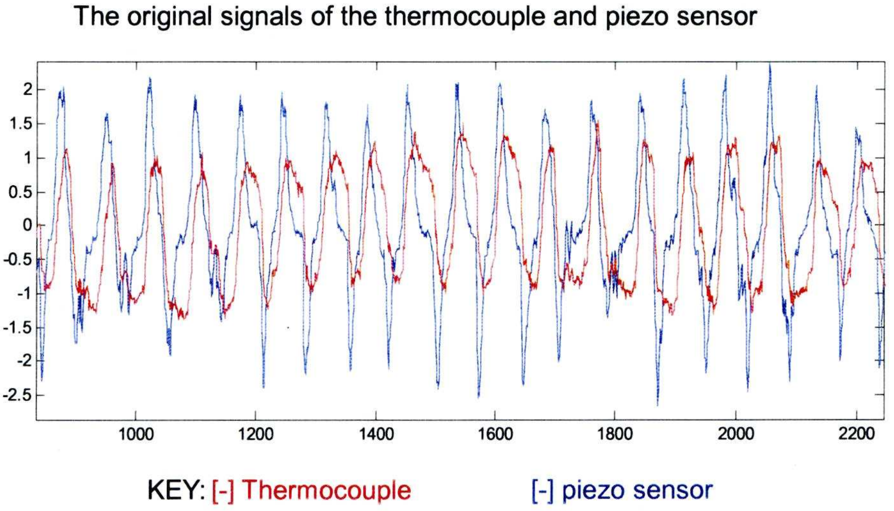

(a)

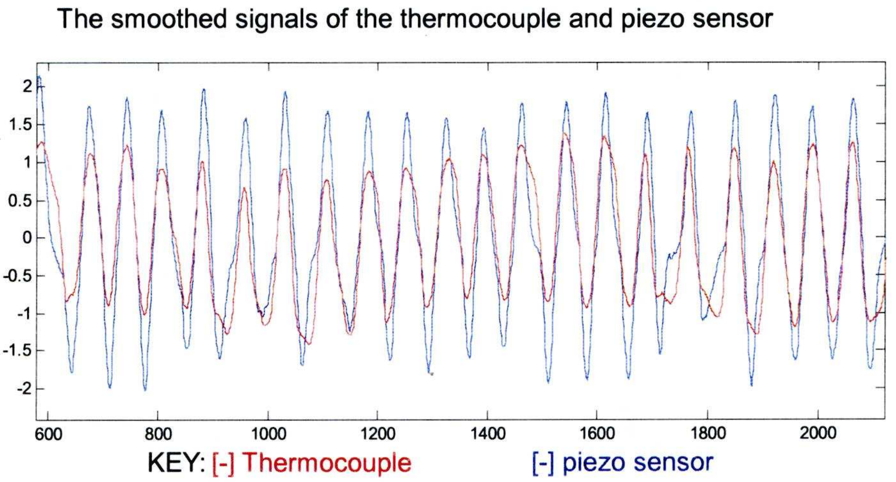

(b)

Figure 2-6: The above chart shows the breathing signal obtained from the thermocouple (red trace) and piezo sensor (blue trace). The original signals are show in figure a. The signals in Figure b were filtered by a 15 step moving average filter. The phase shift between the signals is adjusted, such that the correlations can be easily observed.

2.1.2. The signal amplifier and noise filter in the Experimental Respiratory Monitor

2.1.2.1.

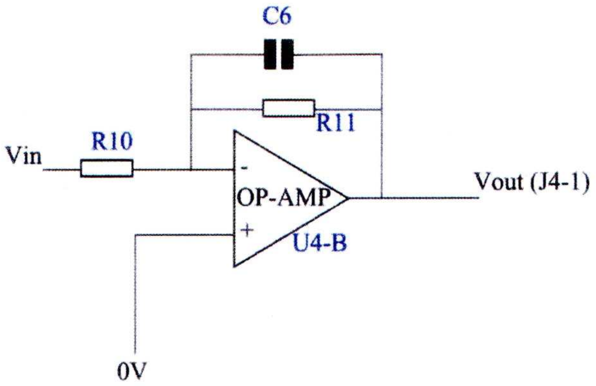

Figure 2-7: The lowpass filter circuit of the transducer. A first order lowpass filter is constructed by putting a capacitor C6 in parallel with the feedback resistor R11.

2.1.2.2. Noise Filter and Anti-aliasing Filter

When air flows past the piezo ceramic film it creates vibrations. These vibrations are relatively high in frequency (when compared with the temperature change). The signals of both the air-flow vibration and the temperature are picked up by the sensor. Since only the temperature signal is of interest, a low-pass filter is used to remove the air vibration signal. The lowpass filter removes the high frequency while preserving the breathing signal. The filter also acts as Anti-aliasing Filter to restrict the bandwidth of the signal prior to sampling by the AD converter.

The circuit broad of the transducer measures 11x11mm^2 only. Most of the space has been occupied by the Operational Amplifier chip with Dual In-Line package. A first order filter was used because of space restrictions in the prototype.

Although the signal of the piezo-electronic sensor can be processed by the onboard micro-controller, the amplitude of the noise signal can saturate the input of the Analogue to Digital Converter of the device. It is therefore necessary to remove the noise from the signal before the analogue to digital conversion. The low pass filter circuit is located inside the transducer. It is a first order low-pass filter with an operational amplifier and a capacitor across the feedback resistor (figure 2-7). This has the effect as the frequency rises of increasing the level of feedback as the reactive impedance of the capacitor falls. The impedance of the feedback X_f of the circuit for a frequency f is:

$$X_f = \frac{1}{2\pi f C + \frac{1}{R11}} \tag{2.1}$$

where $R11$ is the value of the feedback resistor and C is the capacitance of the feedback capacitor.

The frequency response for different capacitance values is plotted in figure2-8 for the frequency range from 0.01 Hz to 10 kHz.

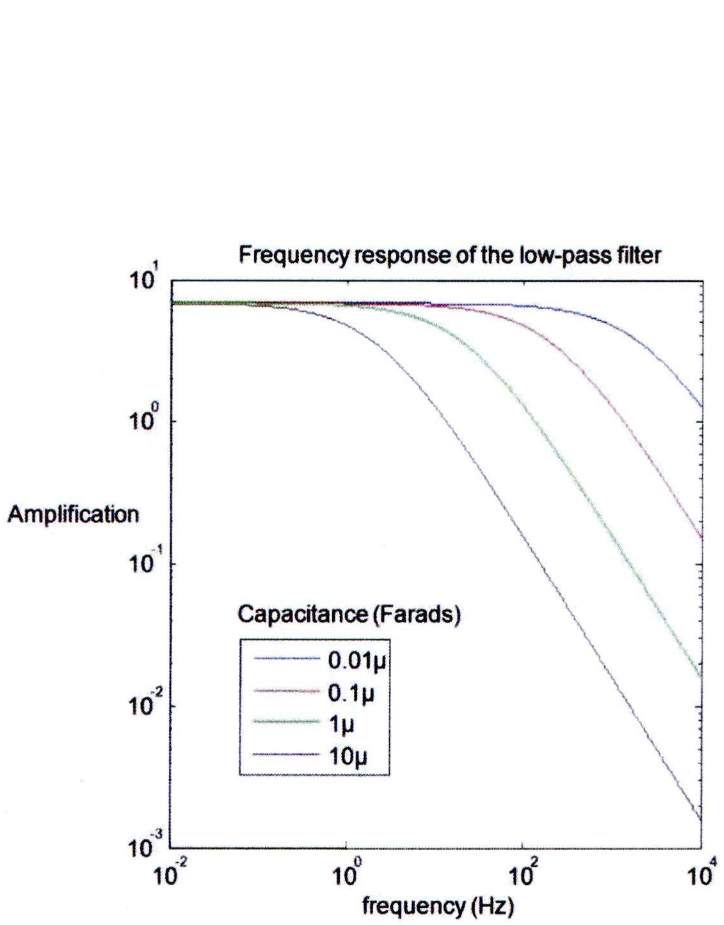

Figure 2-8: The frequency response of the Operational Amplifier for different values of feedback capacitor

The frequency of the respiration signal ranges from 0.5Hz (30 breaths per minute) to 0.1Hz (6 breaths per minute). The system should therefore be linear within this range. The original 0.1µ F capacitor (*C6*) was therefore replaced with a 1µ F capacitor.

2.1.2.3. Evaluation of the amplification of the original design

It was found that if the subject breathed deeply the output of the operational amplifier would saturate (figure 2-9). The peaks and the troughs of the signal could therefore be significantly distorted.

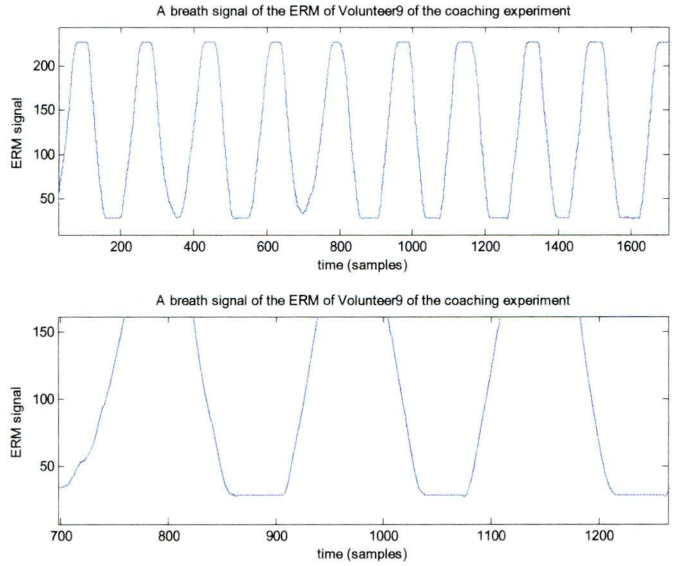
A breath signal of the ERM of Volunteer9 of the coaching experiment

A breath signal of the ERM of Volunteer9 of the coaching experiment

Figure 2-9: An example of the saturation of the breath signal of the ERM. The upper chart is the full signal. The lower chart is a magnified view of the troughs of the 700th to 1300th samples.

The amplification of the operational amplifier needed to be adjusted such that the output is within the range of the supply voltage. R11 was replaced with a 1MΩ variable resistor in the serial port (earlier) version of the ERM. The updated circuit board is shown in Figure 2-10. It was found that the replacement provided satisfactory output in the cases of high respiration tidal volume. The Bluetooth (newer) version of the ERM provides no access to the circuit in the transducer cavity; therefore, its amplifier circuit remains unchanged.

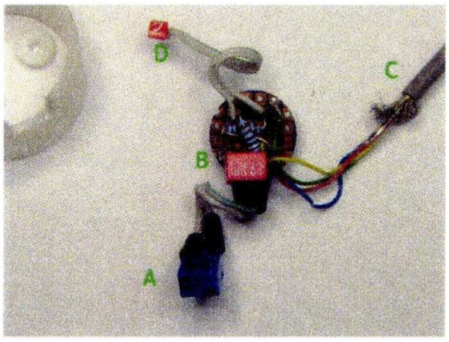

Figure 2-10: The circuit board of the modified Transducer. (A)The feedback Resistor R11, (B) the 1µF feedback capacitor, (C)the connecting wire to the microcontroller and (D) the connecting wire to the piezo sensor.

2.2. Chapter summary

The Experimental Respiratory Monitor (ERM) was found to have high correlations with the temperature in the air mask. It has been found that the piezo sensor of the ERM has no difference in responses time as the thermocouple. The Noise/Anti-aliasing Filter and the amplification circuit was modified to minimize distortion. There was no evidence to show any effect of the protective membrane of the piezo sensor.

3. Coached and Natural Breathing Study

3.1. Introduction:

Managing respiratory variations for treatment planning and delivery is an important issue, especially in the treatment of lung cancer patients .Respiratory motion causes some problems during imaging (Shimizu *et al* 2001, Vedam *et al* 2003, van Herk *et al* 2000, Ritchie *et al* 1994, Ford *et al* 2003, Balter *et al* 1996) and treatment (Keall *et al* 2004, Yu *et al* 1998, Bortfeld *et al* 2002, Chui *et al* 2003, Jiang *et al* 2003). During CT image acquisition, respiratory motion may cause artifacts and blurring. Thus, the identification and delineation of the internal structures would be compromised. Extra margins are added to the target volumes to ensure adequate dose to the tumour and larger margins are needed where the target volume is moving. This may lead to normal tissues receiving more dose when compared with a static internal structure.

The accuracy and application of gating techniques is dependent on the regularity of the respiratory motion. Respiratory motion varies between cycles, sessions and patients (see Chapter 1.2: Lung anatomy & respiratory physiology). Breathing coaching is a solution to improve the reproducibility and regularity of patient respiration (Kini *et al* 2003), which in turn will improve the delivery of respiratory motion compensation techniques and thereby reduce the size of the margins required. The work performed in this chapter is to investigate the impact of coaching on the variability of respiratory motion. A novel method of measurement was applied to measure breathing pattern variations. The breathing pattern variations of natural breathing and audio coaching (using the Varian RPM system, Varian Inc., Palo Alto, CA) were evaluated for 9 volunteers. The usefulness of the ERM for breathing monitoring was also evaluated and compared with the Varian RPM system.

Audio coaching involves giving an audio instruction at regular intervals to guide the patient (or subject) to breathe. The Varian RPM system was setup in the Clatterbridge Centre for Oncology. The system outputs the audio instruction to a pair of computer speakers, with a recorded voice giving “breathe-in” and “breathe-out” messages. The Varian RPM program displays the breathe-in and breathe-out intervals on the screen. The repetition rate of the audio prompt was chosen to match the subject’s natural respiration rate without coaching. The rate would be reduced by the operator if the subject could not keep up with the audio prompt.

3.2. Regularity of Coached and Natural breathing in Healthy Volunteers

Healthy people’s breathing behaviour was measured using two respiration monitoring systems following different protocols. The experiment involved 9 healthy volunteers who were relatives of cancer patients. The average sampling duration of the datasets was about 200 seconds. The ERM respiratory device and the Varian respiratory device were used to measure the breathing.

The Varian RPM system tracks the vertical position of a pair of infrared reflective markers on a small lightweight marker block. The markers are circular with about 5mm diameter. After setting up the patient's position for the treatment, the marker block is placed on the patient's chest or the abdomen, depending on the magnitude of the movement. On some of the subjects, the motion of the marker was so small that the Varian RPM failed to generate an accurate voice coaching. The Varian RPM system receives live infrared video images of the markers from a CCD tracking camera. The vertical motion of the markers due to patient's breathing is then detected and recorded every 1/25 second by a digital image analysis and video tracking software program running on a Windows XP workstation. We used a pair of speakers connected to the computer's sound card. The audio prompting coached the volunteers to breathe-in or breathe-out at periodic intervals.

3.3. Methodology:

The Varian RPM system was used to monitor the thorax displacement and the ERM was used to monitor the airflow at the patient's mouth. An infrared reflective marker box was put on the thorax of the volunteer, who was also wearing an oxygen mask with the ERM's transducer attached. An image of the set up is shown in figure 3-1.

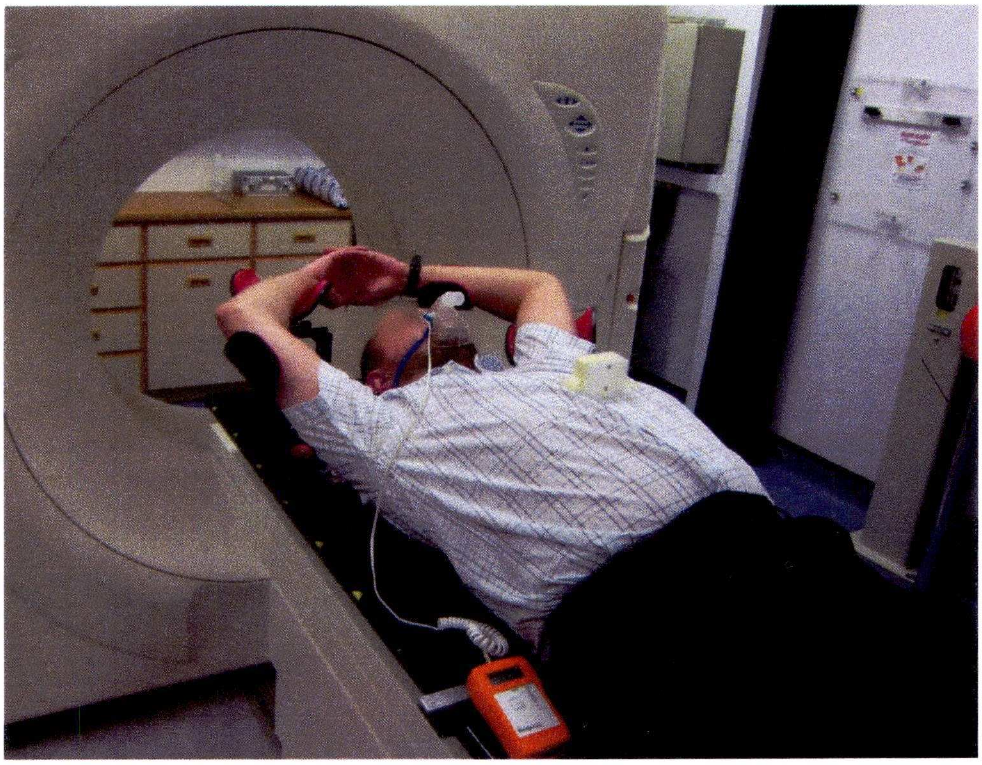

Figure 3-1: The Infrared reflective marker box of the RPM system) was put on the thorax of the volunteer who was also wearing an oxygen mask with the ERM's transducer attached.

3.3.1. Synchronization:

The ERM device and the Varian RPM system need to be synchronized in order to compare the signals. The Varian system has no preset synchronization with other breathing monitoring devices. There is an "Enable gating" button on the user interface of the RPM program to trigger the gating feature of the system. When it is enabled, the system triggers the gating pulse. For the interface to the CT scanner a short pulse is generated by closing a switch on a relay board connected to the workstation. The time and duration of the pulse is logged in a specific field of the patient data file. A simple device was created to monitor the triggering signal from the RPM system so that when the RPM program triggered the CT scanner, the ERM system could also detect and log the pulse. To achieve this, A PICO ADC11[4] was connected into the parallel port of the ERM workstation. The output from the relay of the Varian gating system was recorded with an ADC. At the end of each experiment, there were two pairs of signals, ie (1) the Varian breathing signal and its corresponding gate triggering signal, and (2) the ERM signal and its triggering pair. The ERM's signal was sampled at 10Hz, while the Varian RPM was sampled at 25Hz. Hence, an up-sampling operation is needed, such that the ERM signals can be synchronized with the Varian signals. The ERM's signals were up-sampled by 2.5 times to match the frequency of the Varian RPM signal. This was followed by a low-pass filter where a moving average filter with 5 samples-length was used. The two signals were then aligned by referencing to the CT trigger signals.

A synchronization device was built for this experiment to provide a safe way to obtain the signal given out by the Varian gating workstation to the CT scanner. The detailed design and operation of the synchronization of the device is presented in the Appendix (Chapter 3.7).

In this healthy volunteers study, breathing signals were acquired from 9 volunteers in coached and natural breathing mode. Each volunteer participated in up to 4 sessions. For the first session, the RPM reflective marker box was placed either on the chest or the abdomen. For this session, the volunteer breathed naturally (no

---

[4] *PICO Technology Ltd. UK ADC11.*an analog to digital converter connect to the parallel port of a computer.

coaching applied). At the end of the first session the Varian RPM system calculates the period of the subject's respiration. For the second session, audio coaching was applied. The period of repetition of the coaching was set with reference to the value obtained in the first session, so that the volunteer was given the audio coaching instructions based on the frequency of their own breathing. The coaching frequency would be further adjusted if the volunteer was not able to comply with the repetition rate of the instructions. The third and fourth sessions were a replication of the first and second sessions, but the marker block was put on a different part of the chest. Among the sets of signals from the two marker positions, the set of breathing signals with larger marker displacement in the natural breathing mode was used for analysis. However, in some of the sessions, the displacement of the reflective marker was so small that, the Varian RPM program was not able to detect a breathing cycle. In such circumstances it would not be possible to use gating either for the initial CT scan or for treatment. While it is probable that the tumour motion would be sufficiently small that gated treatment would not be necessary, the inability to carry out a 4D CT scan would make it difficult to verify the lack of movement. With the ERM an adequate signal was always visible.

3.3.2. Measurements:

The following quantities were measured to evaluate the regularity of the breathing:

3.3.2.1. Variation in Breathing Patterns:

For each subject, the variations of breathing patterns in coached and natural breathing modes were evaluated using the output of both the RPM and the ERM. The variation of the respiration signal was measured by a novel metric defined as the "sum of the standard deviation of the breathing patterns". Using the Hilbert transformation, the phase of the signal, *x(t)*, was determined retrospectively.

For a normalized breathing signal $x(t)$, the Hilbert transform is operated by convolution of $x(t)$ with the Hilbert kernel $\mathfrak{H}(t)$ followed by :

$$\mathfrak{H}(t) = \frac{1}{\pi t} \tag{3.1}$$

The Hilbert instantaneous phase $\theta[t]$ becomes:

$$\theta(t) = tan^{-1}(\frac{\mathfrak{H}(t) * x(t)}{x(t)}) \tag{3.2}$$

,where '*' is the convolution operator. For more information about the Hilbert Transform, please see Chapter 5.2.2.

The signal was then broken up into a number N_t of breathing cycles. In each cycle i, the signal x_i was re-sampled at constant intervals of phase. It was done by linear interpolation of x_i at every phase value θ_q for $1 \leq q \leq 20$. θ_q was a linear spaced vector in the range of $-\pi$ to π. θ_q is given by:

$$\theta_q = -\pi + \frac{2\pi}{20} \cdot q \tag{3.3}$$

For each value of q the standard deviation σ_q of the $x_i(\theta_q)$ in every breath cycle i was calculated. σ_q is given by:

$$\sigma_q = \sqrt{\sum_{i=1}^{N_t} \frac{(x_i(\theta_q) - mean(x_i(\theta_q)))^2}{N_t}} \tag{3.4}$$

where *mean(.)* is a function to calculate the mean.

The sum R_s of all the values of the standard deviation σ_q of the phase slots is defined as:

$$R_s = \sum_{q=1}^{20} \sigma_q \tag{3.5}$$

Irregularities in respiratory motion patterns lead to higher standard deviation values. Hence, R_s is a reasonable estimator of the irregularity of the breathing signal.

3.3.2.2. Variation in Periods

A single breath cycle is defined as the samples between two neighbouring local maxima. The breathing period is defined as the mean of time durations of all the cycles in the signal. A point is considered to be a valid maximum if it has the maximal value, and was preceded (to the left) by a value lower by the RMS of the whole signal. After a valid maximum has been found, the algorithm would search for a trough and iterates until the end of the signal.

3.3.2.3. Delay/Time lag between the Varian RPM and ERM

The time lag between the breathing signal of the Varian RPM and the ERM was measured by the position of the global maximum of the cross correlation of the two signals. It is a measure of the similarity of two waveforms as a function of the time-lag applied to one of them.

3.4. Results:

Out of the 9 volunteers, Volunteers-7 and 8 were not able to follow the audio-coaching instructions and fell asleep.

3.4.1. Mean of breathing period:

The mean value of the period as measured by Hilbert phase segmentation of the breathing signal from the ERM and the Varian RPM is listed in the following table:

Table 3-1The mean period of the breathing signals in natural and coaching mode of breathing.

	Mean of Period (seconds)			
	Natural		**Coached**	
	ERM(s)	**Varian(s)**	**ERMs)**	**Varian(s)**
Volunteer-1	5.4	5.3	5.6	5.5
Volunteer-2	7.8	7.8	8.3	7.8
Volunteer-3	3.5	3.5	5.5	5.5
Volunteer-4	4.3	4.3	5.6	5.6
Volunteer-5	5.3	5.3	6.9	6.8
Volunteer-6	4.2	4.3	6.6	6.6
Volunteer-7	5.3	5.2	8.5	8.8
Volunteer-8	8.7	9.3	6.8	6.8
Volunteer-9	6.3	6.3	7.1	7.1

The mean of the breathing period of the 9 volunteers, measured by the ERM, ranged from 3.5 to 8.7 seconds in the natural breathing sessions.

In the Audio Coached sessions, the mean of the breathing period, measured by the ERM, ranged from 5.5 to 8.5 seconds.

The mean difference between the Varian and ERM measurements in both coached and natural breathing mode is 0.1s (with standard deviation 0.2), This difference is very small and can be neglected.

For the sessions of Volunteers-7 and -8, the subjects had fallen asleep during the experiment, so that the subjects did not follow the audio instructions.

3.4.2. The RMS of the position of the Varian RPM marker & the ERM signal:

The section of breathing signal during which the subject had fallen asleep, as well as the section during which the ERM measurement was saturated has been removed from the signal. The RMS of the breathing signal of the ERM and the Varian RPM in natural and coached breathing are listed Table 3-2. In coached breathing mode, 8 out of 9 volunteers had larger respiratory motion measured by the ERM, while 7 out of 9 volunteers had larger respiratory motion measured by the Varian system. Volunteer-8 had a decreased RMS of breathing which is related to the decrease in the breathing period.

Table 3-2 : The RMS of the breathing signals in Natural and Coaching mode of breathing. The units of the ERM signal are arbitrary and the signal ranges from 0 to 255.

	RMS of the breathing signal			
	ERM (0-255)		**Varian (cm)**	
	Natural	**Coached**	**Natural**	**Coached**
Volunteer-1	15.0	25.3	0.30	0.36
Volunteer-2	28.5	42.2	0.31	0.36
Volunteer-3	12.9	43.5	0.20	0.28
Volunteer-4	17.2	25.2	0.20	0.24
Volunteer-5	15.9	37.8	0.41	0.39
Volunteer-6	15.9	25.4	0.18	0.23
Volunteer-7	43.9	52.3	0.12	0.18
Volunteer-8	84.1	43.4	0.98	0.80
Volunteer-9	58.3	86.9	0.47	0.75

3.4.3. The Variations of breathing pattern

Since every volunteer had different RMS amplitude of their breathing signal, the sum of the standard deviations of the breathing pattern (Rs) of each volunteer was normalized by the RMS amplitude of their breathing signal. With the fallen-asleep and saturated samples removed, the normalized "Rs" values of natural and coached breathing modes measured by the two monitoring systems are shown in figure 3-2.

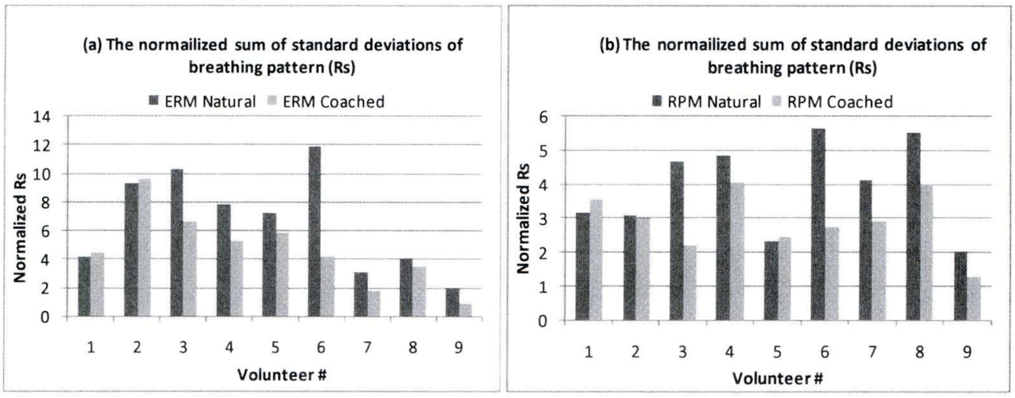

Figure 3-2: The comparison of pattern variation in Coached and Natural breathing: The normalized sum of the standard deviations of the breathing pattern (Rs) of (a) the ERM and (b) Varian RPM.

From the breathing signal of the Varian RPM, reduction in the variation of the breathing pattern was observed in the sessions of Volunteer-2, 3, 4, 6, 7, 8 & 9. From the breathing signal of the ERM, reduction in the variation of the breathing pattern was observed in the sessions of Volunteer-3, 4, 5, 6, 7, 8 & 9. Audio coaching generally decreased the normalized Rs values with $p=0.049$ by ERM and $p=0.026$ by the Varian RPM. An example of the improvement in the regularity of Volunteer-6 is shown in Figure 3-3 where the amplitude is plotted against the phase. Figure 3-4 plots the amplitude against time. The increase in regularity when changing from natural breathing (Figure 3-4a) to coached breathing (Figure 3-4b) can be found on the figure.

The measurements from the Varian RPM and the ERM were not consistent in Volunteers-2 & 5. The measurements of the two devices were not significantly differed in Volunteer-2. For volunteer-5, the baseline of the RPM signal drifted by a small amount in coaching mode, resulting a larger value of R_S. However, in Volunteer 3,4,6,7 & 9, the benefit of audio coaching was significant, with 34% - 65% reduction in the normalized Rs value.

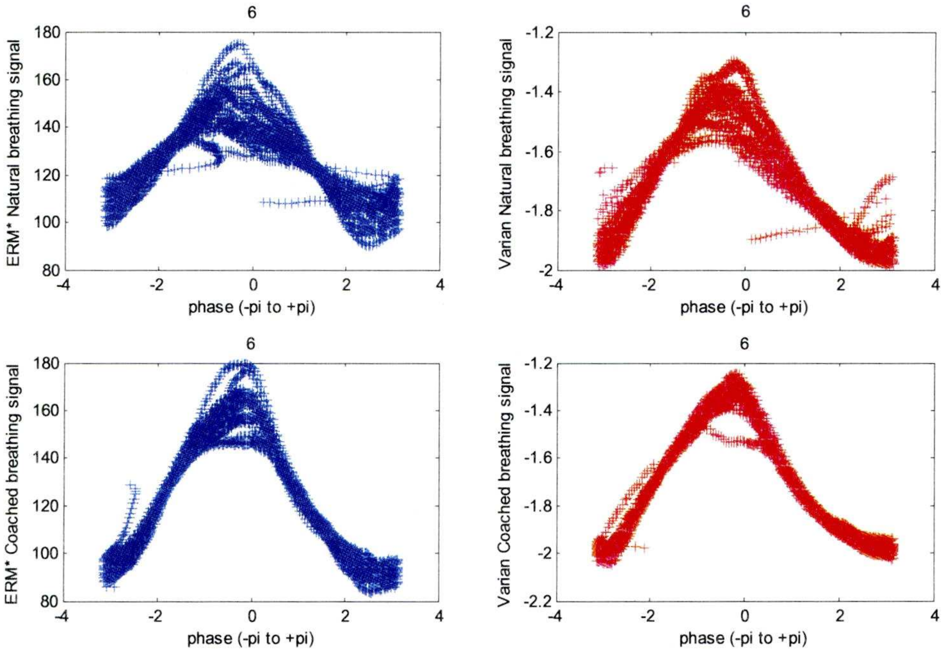

Figure 3-3: Distribution of breathing signal according to the Hilbert phase.The amplitude-phase distributions of Volunteer-6 are shown on the above four charts. The charts on the top were collected from the samples of Natural breathing, while the charts at the bottom are coached breathing. The blue charts on the left hand side are the breathing signal collected by the ERM, while the red charts on the right hand side are the breathing signal collected by the Varian RPM.

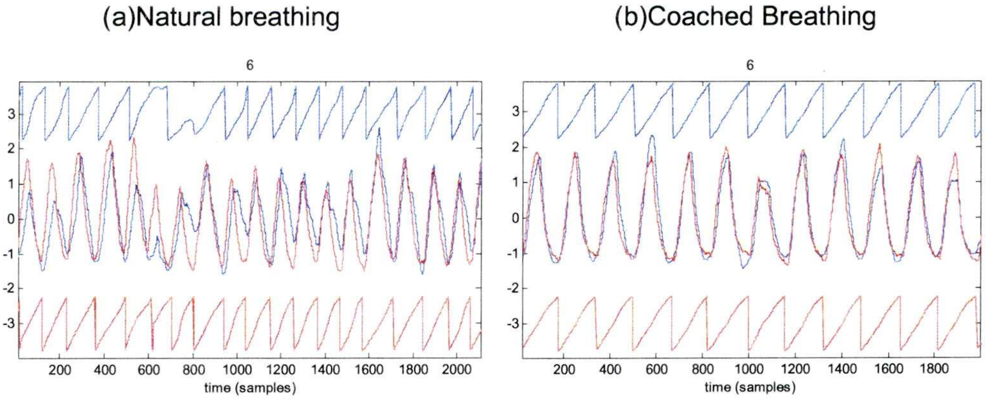
(a)Natural breathing

(b)Coached Breathing

Figure 3-4: The breathing signal and its Hilbert phase of Volunteer-6 in (a) natural breathing mode and (b)coached breathing mode. The blue trace on the top is the phase of the ERM breathing signal. The blue trace in the middle is the ERM breathing signal. The red trace in the middle is the Varian RPM breathing signal. The red trace at the bottom is the Hilbert phase of the Varian RPM breathing signal. The scale of the phase signals was adjusted, so that they could be fitted into the same graph. The horizontal axis is the time axis. The signals were sampled at 25Hz

3.4.4. The time lag between the ERM and the Varian RPM

The time lag between the ERM and the Varian RPM was calculated by cross-correlation for each session. The results are shown in the following table, in which a position value represents the ERM signal lagging the Varian RPM signal:

Table 3-3: The time lag between the ERM and the Varian RPM. A position value represents the ERM signal lagging the Varian RPM signal

The time lag between the ERM and the Varian RPM		
	Natural (s)	**Coached (s)**
Volunteer-1	-0.32	0.2
Volunteer-2	-0.48	-0.28
Volunteer-3	0.36	-0.52
Volunteer-4	0.08	-0.04
Volunteer-5	-0.16	-0.24
Volunteer-6	0.36	0.2
Volunteer-7	0	-0.52
Volunteer-8	0.24	0.16
Volunteer-9	0.12	-0.04
Median	0.08	-0.04
Interquartile range	0.4	0.44

The time lag of the ERM relative to the Varian RPM ranged from -0.48 to 0.36 seconds in Natural breathing mode and -0.52 to 0.20 seconds in coached breathing mode. The difference in lag values owes to the breathing behavior of individual patient.

3.4.5. The correlation between the breathing signals of the ERM and Varian RPM:

The correlation between the breathing signals of the ERM and Varian RPM is listed Table 3-4:

Table 3-4 The correlation between the breathing signals of the ERM and Varian RPM

The correlation between the breathing signals of ERM and Varian RPM:		
	Natural	**Coached**
Volunteer-1	0.88	0.87
Volunteer-2	0.85	0.75
Volunteer-3	0.66	0.64
Volunteer-4	0.95	0.97
Volunteer-5	0.93	0.82
Volunteer-6	0.74	0.95
Volunteer-7	0.70	0.52
Volunteer-8	0.56	0.85
Volunteer-9	0.96	0.97

The correlation between the breathing signals of the ERM and the Varian RPM ranged from 0.56 to 0.96 in Natural breathing mode and 0.52 to 0.97 in coached breathing mode

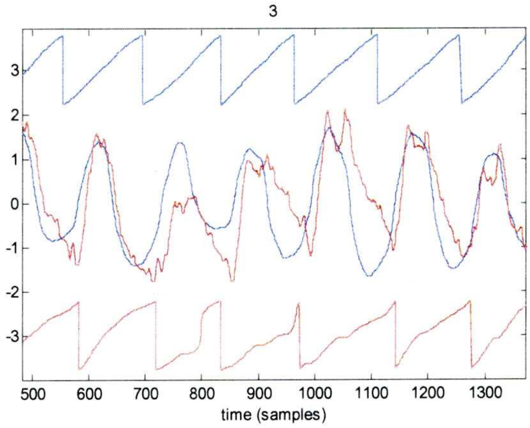

*Figure 3-5: Breathing signal and its Hilbert phase of Volunteer-3 in **coached** breathing -mode.The breathing signals from the 500th to 1350th samples (20s-54s) are shown on the chart. The blue trace on the top is the phase of the ERM breathing signal. The blue trace in the middle is the ERM breathing signal. The red trace in the middle is the Varian RPM breathing signal. The red trace at the bottom is the Hilbert phase of the Varian RPM breathing signal. The horizontal axis is the time axis. The signals were sampled at 25Hz, ie 1000 samples represents 40 seconds.*

High correlation was found between the ERM and the Varian RPM breathing signal in most of the sessions. However, in the sessions of Volunteer-3, the correlation was 0.66 for Natural breathing (figure 3-5) and 0.64 for coached breathing. In the case where the volunteer fell asleep, despite the disagreement in the long exhales (which caused the low correlation), both the ERM and the Varian system measured the normal breathing very well in the session of Volunteer-7 (figure 3-6).

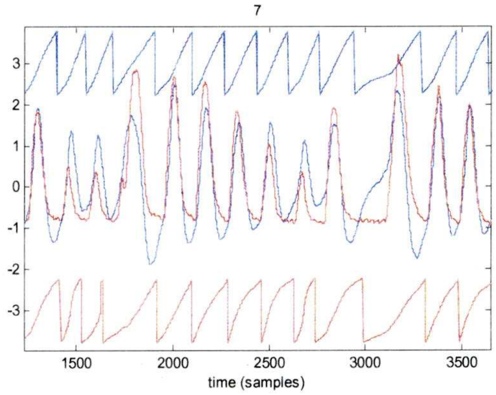

Figure 3-6: breathing signal and its Hilbert phase of Volunteer-7 in ***coached*** *breathing mode.The breathing signals from the 1400^{th} to 3600^{th} samples (70s-144s) are shown on the chart. The blue trace on the top is the phase of the ERM breathing signal. The blue trace in the middle is the ERM breathing signal. The red trace in the middle is the Varian RPM breathing signal. The red trace at the bottom is the Hilbert phase of the Varian's breathing signal. The horizontal axis is the time axis. The signals were sampled at 25Hz.*

3.5. Discussion:

All those volunteers who had an increase in breathing period when coaching was used also had an increase in the amplitude of breathing. The remaining 1 out of the 9 had a reduction in breathing period and a decrease in breathing amplitude.

It may be a result of the body mechanism to maintain a constant supply of oxygen. An audio coaching rate which is lower than the natural breathing rate would increase the amplitude of breathing, because the body needs to maintain a constant supply of oxygen (Priban 1963). As the frequency of gas exchanges decreases, the amplitude of breathing must increase to maintain the same volume of gas exchange. Another possible reason is that, when the subject deliberately breathes in and out, the muscle contracts more rapidly (when compared to Natural breathing), and it results in a larger breathing amplitude.

Haasbeek *et al* (2008) studied the 4DCT of 21 patients and found that audio coaching generally led to an increase in the average total lung volume in the three end of exhale phases (with the breathing cycle divided into 10 phases). A reduction in lung volume was only observed in 3 patients. The total tumour movement was also measured in the 4DCT, in which audio-coaching led to an increase in tumour movement in most of the cases. The finding of Haasbeek *et al* was in agreement with our results. By assuming that the motion of the tumour correlates with the motion of the abdomen, the amplitude of the tumour motion follows the increase in the standard deviation of the breathing signal. The increase in the volume of the lung increased the airflow passing over the transducer of the ERM, and the amplitude of the ERM signal increases.

George *et al* (2006) investigated 311 breathing signals (using the Varian RPM system) from 24 patients. The breathing signals were used to evaluate the residual motion. The conclusion was that audio-coaching tended to cause the amplitude to increase as compared with the effects of Natural breathing and Audio-Visual feedback. Audio coaching also significantly increased the residual motion in Inhale phase gating. Our findings agree with George *et al.* Despite the increase in amplitude when audio coaching is applied, our work is different in that the regularity of breathing was also evaluated. The variations of the breathing patterns (normalized Rs) were reduced in most of the volunteer sessions. 4D CT scans, which are widely applied in the planning of gated radiotherapy (Starkschall *et al* 2004, Shih *et al* 2004), can help to determine the mean tumour position, tumour range of motion for treatment planning and the relation of tumour trajectory to other organs. Since the 4D data construction requires several cycles of respiration, regular breathing would introduce less artefacts on the 4D image (Ford *et al* 2003, Vedam *et al* 2004b). Coaching can potentially help to maintain regular respiration during the acquisition. Patients with a regular respiration pattern often exhibited a corresponding constant phase relationship between the surrogate and the tumour motion (Vedam *et al* 2003). Coaching could also help to maintain relatively stable correlation between the surrogate and the tumour so that gating can be reliably delivered.

In our experiment, the volunteers found it to be more comfortable to have a slower than normal rate of breathing. This may be because when the subjects were asked to breathe in and out they naturally breathed more deeply. This inevitably resulted in the amplitude increase which is directly proportional to residual motion in gated radiotherapy. In order to minimize this effect, the operator should choose an audio coaching repetition frequency which is as close to the natural rate of breathing as possible.

There were 2 subjects that fell asleep during the experimental sessions. This would be unlikely to occur in real clinical practice, but a breathing monitoring mechanism to monitor the regularity of the breathing of the subject is essential. A breathing monitoring algorithm utilizing the ERM device has been developed in Chapter-7.2 to address this problem.

The measurements of the ERM and the Varian RPM were mostly in agreement with each other in terms of the mean breathing period and the RMS value of the breathing amplitude. Hence, the ERM could be used as a replacement for the Varian RPM for comparing the stability of breathing. The aim of coaching was to increase the stability of breathing. With the ERM device, it is possible to determine whether coaching should be applied to a specific patient and to compare the effect of different coaching techniques.

Limitations on Sample size

The original purpose of the healthy volunteer experiment was a pilot study of the procedures of using the ERM as a breathing monitor. The results showed that the correlations between the ERM and the RPM was larger than 0.5 ($p<0.01$) in both coached and natural breathing. Therefore, this supported the next phase of study of applying the device on patients (Chapter 4).

Regardless of coaching rate, the coached motions are more regular than natural breathing (paired T-test on R_S: $p=0.02$ by ERM and $p=0.01$ by Varian). However, one of the volunteers had a reduced rate of coaching, while the remaining 8 samples had increased coaching rates. It was statistically significant to argue that, with a decreased coach rate, audio coaching increases the regularity ($p=0.03$ by ERM) as well as the amplitude ($p<0.01$). The data was not sufficient to show a statistically significant difference in the effect of a reduced coach rate.

The above conclusion is based on the assumption that the data are normally distributed. Owing to the sample number, it is difficult to prove this. In such cases, the Wilcoxon signed-rank test is used to test the statistical significance on the differences of the medians. The result of the test shows that the medians differ ($p=0.04$ by the ERM).

However, the null hypothesis cannot be rejected for the data (R_S) measured by the Varian RPM ($p=0.08$). This suggests that either more data are needed or the Varian RPM cannot detect differences of this magnitude. The p value is not far away from the critical value (0.05). Hence, a difference is likely to be found if there were more samples.

3.6. Conclusions:

In this study, the breathing signals of 9 volunteers were investigated using the ERM and the Varian RPM system. Despite the increase in amplitude of breathing, there was an increase in regularity (ie decrease in normalized Rs) after audio coaching was applied. The ERM was found to be a good tool to measure the breathing period and breathing pattern variations. In addition, it is easy to set up when compared to finding the best position on the thorax to attach the reflective marker of the Varian RPM system. The ERM signal was also found to be well correlated with the Varian RPM signals. The breathing signal of the ERM can represent the End of Inhale/Exhale position as well as having a smooth transition between the two positions. Hence, it has the potential to be used as a respiratory monitoring device for triggering the gating signal in gated radiotherapy. An investigation of this is presented in Chapter 4.

3.7. Appendix

3.7.1. Synchronization device:

A Synchronization device was designed and built to extract the gating signal sent out from a logic board in the Varian RPM workstation. The Varian RPM system generates a gating signal by the PCI logic board to trigger the CT scanner (figure 3-7). The PCI board on the Varian workstation would close and connect pin-1 and pin-9, which are operated by the relay on the PCI board. The synchronization device connects the workstation and the CT scanner (figure 3-8). The potential difference across the coil of the relay of the synchronization device was 12V when it was closed; and 0V when it was open. A variable potential divider was connected in parallel to the coil of the relay. An Analog to Digital Converter was connected to the variable potential divider to detect the change in potential difference. A photo of the device is shown in figure 3-9.

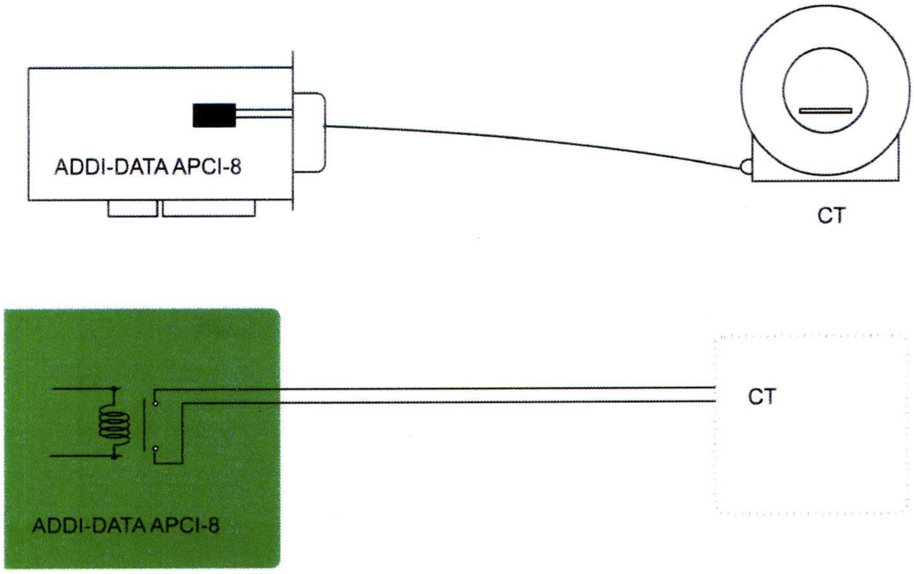

Figure 3-7: (upper figure) Normal Connection between the CT scanner and the PCI logic board on the Varian RPM workstation. When the relay box is not used, the relay board directly triggers the CT scanner.(bottom figure)

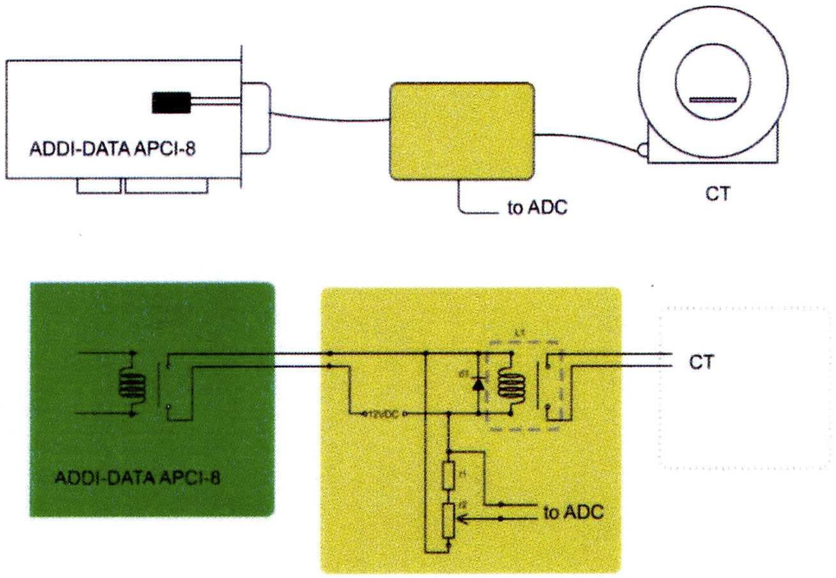

Figure 3-8: Connection between the CT scanner and the PCI logic broad on the Varian RPM workstation. When the relay box is used, the relay board triggers the CT scanner with a secondary relay.

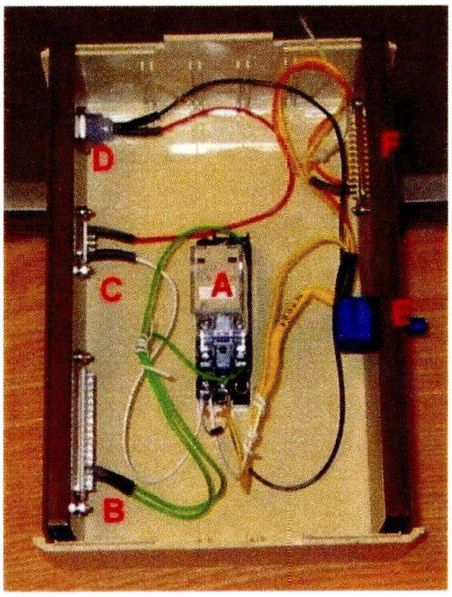

Figure 3-9: A photo of the synchronization device when it is opened. A:relay, B: connector to the CT scanner, C:connector to the Varian workstation, D:power, E:output voltage (to the ADC) adjustment, F:connector to ADC

4. Fluoroscopy Investigations of the Experimental Respiratory Monitor (ERM) system in Gated Radiotherapy

The experiments in Chapter 3 showed that the breathing signals of the ERM were cyclic and seemingly following the breathe motion. It might therefore be used for producing gating signals. However, without any information about internal organ motion, the degree of synchronization between the ERM signal and the internal motion was still unknown. The synchronization between the ERM and the internal motions was therefore investigated using tumour and diaphragm motion, which were determined from digitized fluoroscopic image sequences acquired during treatment simulation.

In this chapter, the ERM was first evaluated by the correlation of the gating signal with the movement of internal structures, which were visible in fluoroscopic image sequences. Secondly, the residual motions of the targets in amplitude gating were compared using different gating parameters. The aim was to evaluate the performance of the ERM as a breath monitoring device for gated radiotherapy and to compare the accuracy of synchronisation of the potential gating signals with the underlying tumour and diaphragm motion.

4.1. Methodology

Five patients with lung cancer were included in this study. The subject setup was the same as in the healthy volunteer experiment of Chapter-3, except that Audio coaching Visual feedback was provided to Patient-1 by displaying the patient's respiratory signal on a small screen mounted near the subject. For each patient, two fluoroscopy sequences were taken. In the first sequence, the radiation beam was positioned in the Anterior-Posterior direction. In the second session, the beam was positioned in the Left-Right direction. The coaching period parameter was set with reference to the value obtained from the first session so that the patient was given audio coaching instructions based on their own breathing period. The coaching instruction period was further adjusted if the patient was not able to comply with the repetition frequency of the instructions.

4.1.1. Subjects and datasets

For each patient, the internal organ movements were traced in two directions (the plane perpendicular to the LR and the AP directions respectively). There were 5 patients in total (Table 4-2). One (Patient-1) of the patients had been classified by the medical consultant as suitable for gating, because the range of movement was large and the GTV was clearly visible under the fluoroscopy. For this patient the breathing patterns shown by the Varian RPM system in the free breathing sessions were irregular, so both audio and visual coaching was used to help the patient to breathe more regularly. Thus, the movements were recorded in free-breathing (natural) mode and audio-video coached mode, resulting 4 recorded image sequences for this patient. In total there were12 sets of data from the 5 patients. 10 sets of the data sets were free breathing and 2 sets were coached breathing(Table 4-1).The duration of each data sample ranged from 20 to 30 seconds. One of the patients, Patient #3, had already completed treatment. For this patient it was difficult to delineate the tumour because the treatment had successfully reduced the visibility of the tumour. In this case the position of the tumour was estimated based on the movement of the blood vessels and bronchioles near the GTV location.

Table 4-1: Treatment Information of subjects. The above table show the treatment status of the patient when they participated in the experiment, their tumour position and their age

Subject Information:			
Patient number	**Treatment status**	**Tumour position**	**Age**
1	Ongoing	Right-mid-Lobe	60
2	Ongoing	Right-upper-Lobe	65
3	Completed	Right-mid-Lobe	80
4	Ongoing	Right-Lower-Lobe	86
5	Ongoing	Right-Lower-Lobe	71

Table 4-2: Field directions of Datasets. Patient-1 had both Natural and coached breathing sessions. For each breathing mode, fluoroscopy images were available from two beam directions: Anterior-Posterior (AP) and Lateral

Recorded Datasets (session reference number):				
Patient number	**Natural breathing**		**Coached breathing**	
	AP	**Lateral**	**AP**	**Lateral**
1	Dataset-P1a	Dataset-P1b	Dataset-P1c	Dataset-P1d
2	Dataset-P2a	Dataset- P2b	Nil	Nil
3	Dataset- P3a	Dataset- P3b	Nil	Nil
4	Dataset- P4a	Dataset- P4b	Nil	Nil
5	Dataset- P5a	Dataset- P5b	Nil	Nil

The fluoroscopy system was an amorphous silicon flat panel treatment simulator. When operated with the Varian RPM, it records up to 30 seconds of fluoroscopy video which is synchronized with the Varian RPM. The patient setup was identical to the healthy volunteers in Chapter-3.

4.1.2. Synchronization

The ERM device and the Varian RPM system need to be synchronized in order to compare the signals. The Varian system has no inbuilt synchronization feature to connect with other breathing monitoring devices. However, it generates a data file which logged the displacement of the marker block, the phase, the enable-gating trigger and the time. The system takes samples at 25Hz and each reading has a time stamp. The timestamp is the time counts in milliseconds since the user enabled the marker tracking by pressing the mouse button, which is the trigger to switch on the image processing process which tracks the position of the reflective marker block on the infrared image.

A synchronization mechanism was designed for this experiment. A*PICO ADC11* analog to digital converter was connected to the parallel port of the ERM's workstation. The input of the ADC was connected to the switch of the button of the mouse to detect the state of the button-click. The signal obtained from the ADC was time stamped, so the ERM device can be synchronized with the Varian RPM's marker block.

The Varian RPM has a frame grabber to capture the screen of the fluoroscope monitor. A digital clock program (Figure 4-1), which refreshes every 20 ms, showed the system clock at the corner of the screen of the fluoroscope monitor. The clock of the fluoroscope control computer and the ERM workstation were synchronized by Network Time Protocol[5]before each experiment. The time on each frame was manually recorded and combined with the target positions.

---

[5] A Visual Basic program was developed for synchronization of system time between two Windows-XP computers.

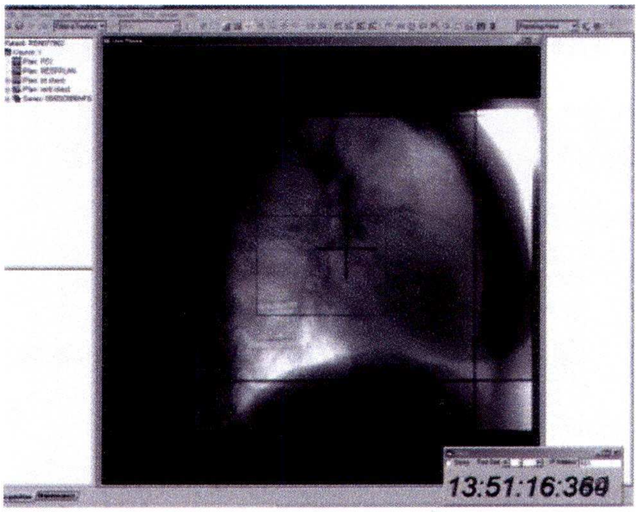

Figure 4-1: A screen capture showing the clock at the lower right hand corner. The clock is used as a reference of time stamp for the internal motion.

4.1.3. Data Processing

For each session, 3 collections of signals was obtained: the fluoroscopic image sequence, the Varian RPM system and the ERM signal. The goal of processing the data was to obtain a set of synchronized signals (in relation to the absolute time):

- the amplitude signal of the two gating modalities,
- the phase signal of the RPM
- the motion signal of the centre of the tumour and the diaphragm.

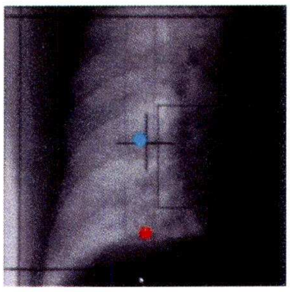

Figure 4-2: Tracking points of the diaphragm and the centre of the tumour on the fluoroscopy image. The dot in light blue was registered as the centre of the tumour and the dot in red was registered as the position of the diaphragm.

For each image in the fluoroscopy sequence, 1) the centre of the tumour and 2)a point, usually the highest point in the centre of the diaphragm (Figure 4-3), were identified by a member of our clinical staff. The tracking of position of the above two features in each image sequence was repeated three times and then followed by seven-step moving average filter.

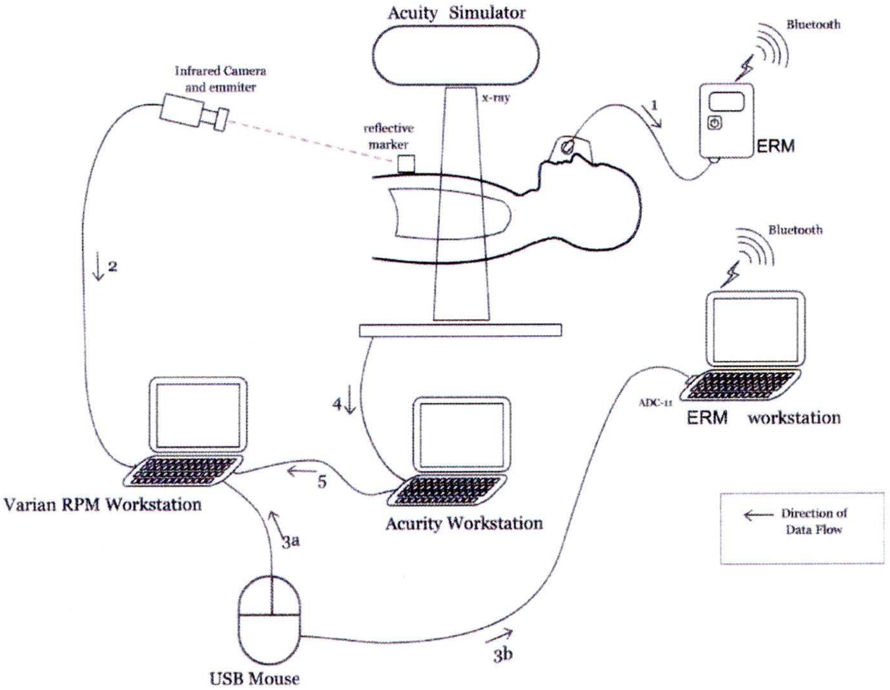

Figure 4-3: Schematic diagram of the synchronization and data flow of the different systems involved. The Varian RPM system includes the IR camera, reflective marker, workstation and the USB mouse. The Acuity Fluoroscopy system includes the X-ray unit, imaging panel and the control workstation. The ERM system includes a control workstation with Bluetooth connection, the ERM and a face mask. The arrow indicates the direction of interaction (a signal transfer from the end of the arrow to the head of the arrow). The numbers next to the arrows represents the interaction sequence (the order of interaction) starting from arrow Number 1 in the upper right corner.

Three systems were running in parallel while the patient was undergoing fluoroscopic imaging (Figure 4-4). The system clock of the Acuity Workstation and the ERM Workstation were synchronized at the beginning of in each session. The breathing signal was transferred by the transducer to the ERM (Figure 4-4 Arrow #1). The data was sent to the ERM Workstation and time-stamped to the system clock. (Figure 4-4 Arrow #2) The Varian RPM Workstation captured the motion of the reflective markers located on the patient's chest/abdomen. (Figure 4-4 Arrow #3a) When the Varian Workstation triggered tracking of the reflective marker, (Figure 4-4 Arrow #3b)the same trigger signal was also sent to the ERM's Workstation. (Figure 4-4 Arrow #4)The fluoroscopy images were displayed on the screen of the Acuity Workstation. (Figure 4-4 Arrow #5) A frame grabber which is part of the Varian RPM system captured the fluoroscopy image from the Acuity Workstation.

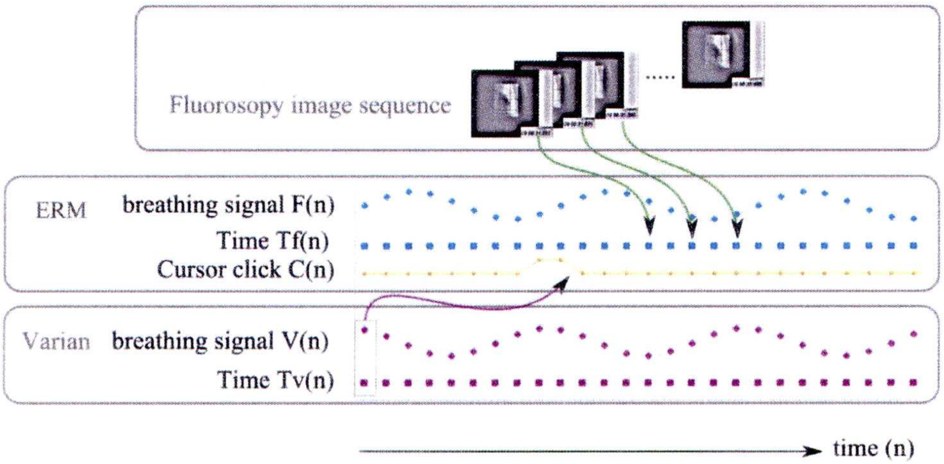

Figure 4-4: Schematic drawing of the associations and synchronizations of data series from different systems.

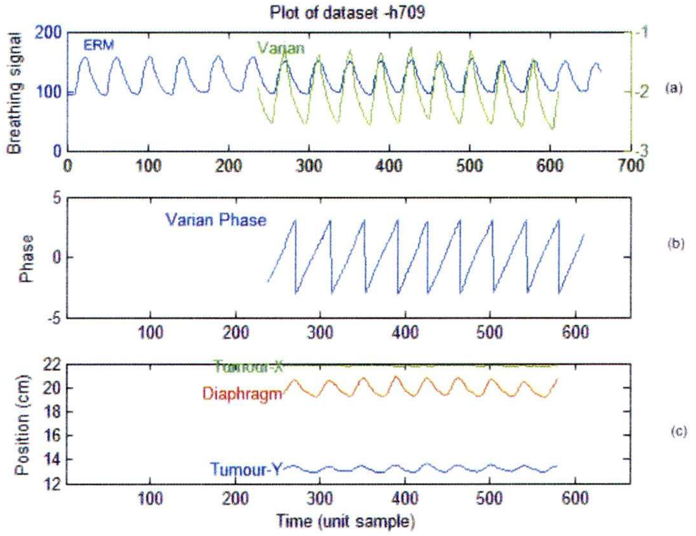

Figure 4-5: Plot of the dataset of Patient-2 against absolute time. (a)The upper figure shows the breathing signal of ERM and Varian RPM. (b) The middle figure shows the original phase of Varian RPM. (c) The bottom figure shows the Tumour and Diaphragm motion. The Sampling Frequency(Fs) of the dataset was 8.3Hz.

There were 3 datasets collected in each session (Figure 4-5): the fluoroscopic image sequence, the ERM's data file and the Varian Data file. The timestamp of ERM (Tf[n]) and Fluoroscopy (Ti[n]) were absolute time, while the Varian (Tv[n]) was relative time. Tv[n] is the count in milliseconds since the user pressed the mouse button, which is recorded in mouse-click signal C[n]. There were absolute time timestamps on every frame of the fluoroscopy image, so the image sequence can be synchronized with the dataset. An example of the final dataset is shown in Figure 4-6. Only those signals which are overlapping the motion signals (bottom chart of Figure 4-6) were used for gating simulation.

4.1.3.1. Internal motion traced by Fluoroscopy imaging

The tracking of the position of the tumour and the diaphragm on the fluoroscopy image was done manually. In order to decrease the error in identifying points on the fluoroscopy frames, the tracking was repeated three times. The motions of the internal structures were measured by averaging the three traces of the internal structures.

The following signals were recorded:

1. the horizontal motion of the diaphragm,
2. the vertical motion of the diaphragm,

3. the horizontal motion of the centre of the tumour,
4. the vertical motion of the centre of the tumour.

Excluding the horizontal motions of the diaphragm

Since the diaphragm can be seen as a coronal structure on the anterior-posterior (AP) view and it mainly moves in the inferior-superior (IS) direction, the change in position in the left-right (LR) and AP directions would be relatively small when compared to the IS movement. For this reason only the IS motion of the diaphragm was studied.

4.1.4. Problems of tumour tracking

The fluoroscopy image is the density of the internal structure projected on the image plane. The projections of every organ overlap each other. It is not always possible to identify and outline the position of an organ in the image. Due to the lack of depth information in the image, we cannot guarantee that the tracking point is coplanar with the tumour. Thus the tracking point may be in a different position from the tumour.

The fluoroscopy image sequence was coded using the Intel Indeo video codec, which is a lossy codec. The compression setting is built into the Varian RPM software which cannot be modified by users. The delineation of the tumour might be affected by the artefacts caused by the video codec.

4.1.5. Unit of measurement of the internal motion

A computer generated grid is projected onto the fluoroscopy image with a grid size corresponding to 1cm at 100 cm from the radiation source. The amplitude of movement was measured as a number of pixels in the image. To determine the amplitude of movement it was necessary to calculate the number of pixels corresponding to 1cm at 100cm. A correction was applied if the tumour was not at 100cm from the source. The internal motions on the fluoroscopy images were calculated by dividing the pixel count (length) by the number of pixels corresponding to one small unit on the cross axis gridline (Figure 4-6). The length of one small unit on the cross axis gridline represents 1cm. Among all the sessions of samples, the length of a real object of 1 cm, when projected on the captured fluoroscopy image sequence, ranged from 15 to 18 pixel count.

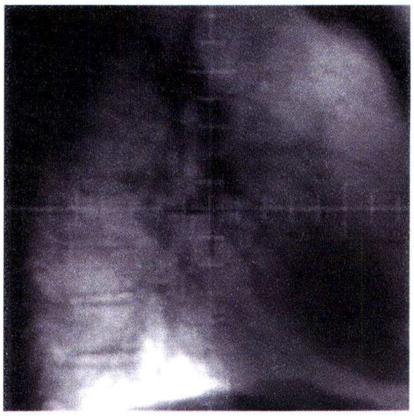

Figure 4-6: A screen capture of the monitor screen of the Fluoroscopy workstation showing the absolute scale of the movement. Each small unit of the ruler represents 1cm at 100cm from the source.

The uncertainty of the motion data *Si* was estimated by the Root Mean Square Error of the signal of the 3 delineations. The uncertainty of the motion of the diaphragm in the sagittal direction was 0.10cm. The uncertainty of the motion of the tumour was 0.21cm in the sagittal direction and 0.10cm laterally. The values were obtained by the RMSE of the three delineations (Chapter 4.1.3.1).

4.1.6. Gating Simulation

We performed a gating simulation using the amplitude gating technique. The 12 datasets of breathing signals and internal organ motions were used. The LANIC beam systematic latency was assumed to be zero that the computation and control delay were not taken into account. The latency will be investigated in Chapter 6. In 10%, 20% 30 % and 40% duty cycle, the residual motion of a point representing the tumour was evaluated.

4.1.7. Gating windows

In amplitude gating simulation, the beam is enabled when the breathing trace goes beyond a threshold $\check{T}$. For gating at the end of expiration (EOE) position, the beam will be enabled when the signal is lower than $\check{T}$. For gating at the end of inspiration (EOI) position, the beam will be enabled when the signal is above $\check{T}$. A suitable threshold $\check{T}$ was used for each position (EOE or EOI) of gating and for different duty cycles. 10%, 20%, 30% and 40% duty cycles were simulated, which were likely to be the usual duty cycle in clinical practice. The value of the amplitude-gating threshold $\check{T}$ was adjusted such that the portion of beam on time(measured in %) was closest to the chosen duty cycle. The optimum amplitude-gating threshold $\check{T}$ for breathing signal x at position φ for duty cycle γ is calculated by:

$$\check{T}|_{\gamma,\varphi,x} = \min(\frac{\ell(G_{\varphi}[\check{T},x])}{\ell(x)} - \gamma)$$

where *min*() is a function returning the minimum value of the input series, ℓ is a function giving the length(or the time duration) of an input signal and $G_{\varphi}[\check{T},x]$ is the residual motion signal when the beam is enabled around the φ position (φ can be either EOE or EOI), x is the amplitude signal of the gating modality.

The residual motion $G_{\varphi}[\check{T}, x]$[6] at the extreme position φ with threshold $\check{T}$ for a gating signal $x = \{x_i |\ 1 \leq i \leq \ell(x)\}$ is calculated by:

$$G_{\varphi}[\check{T}, x] = \begin{cases} \{x_i |\ \forall\, x_i < \check{T}\} & for\ \varphi = \text{"EOE"} \\ \{x_i |\ \forall\, x_i > \check{T}\} & for\ \varphi = \text{"EOI"} \end{cases}$$

where "EOE" is the End of Exhale and "EOI" is the End of Inhale gating; x_i is the i^{th} element of the gating signal x.

4.1.8. Evaluations of the effect of gating

Given a motion series *Y(t)* defined as the position of an object over time. The Root Mean Square (RMS) about its mean position is given by:

$$rms(\, Y[t]) = \sqrt{\sum_{t=0}^{N} \frac{(\, Y[t] - \overline{Y[t]})^2}{t}}$$

where $\overline{Y[t]}$ is the mean of series *Y*[*t*] and N is the length of the series *Y*[*t*].

The aim of gating is to reduce the residual motion of the tumour when the radiation beam is enabled. In the form of mathematics, its aim is to reduce the fluctuation of the motion series. Residual motion is defined as the motion of the tumour when the beam is enabled. In a conventional treatment without gating, the beam is enabled during the whole treatment. In gated radiotherapy, the beam is enabled for a portion of the time (eg: 40% of the treatment duration), and the residual motion is limited to the motion that occurs when the beam is enabled.

---

[6] G[.] is the residual motion in the gating window. An example of G is shown in the bottom chart of figure 4-7.

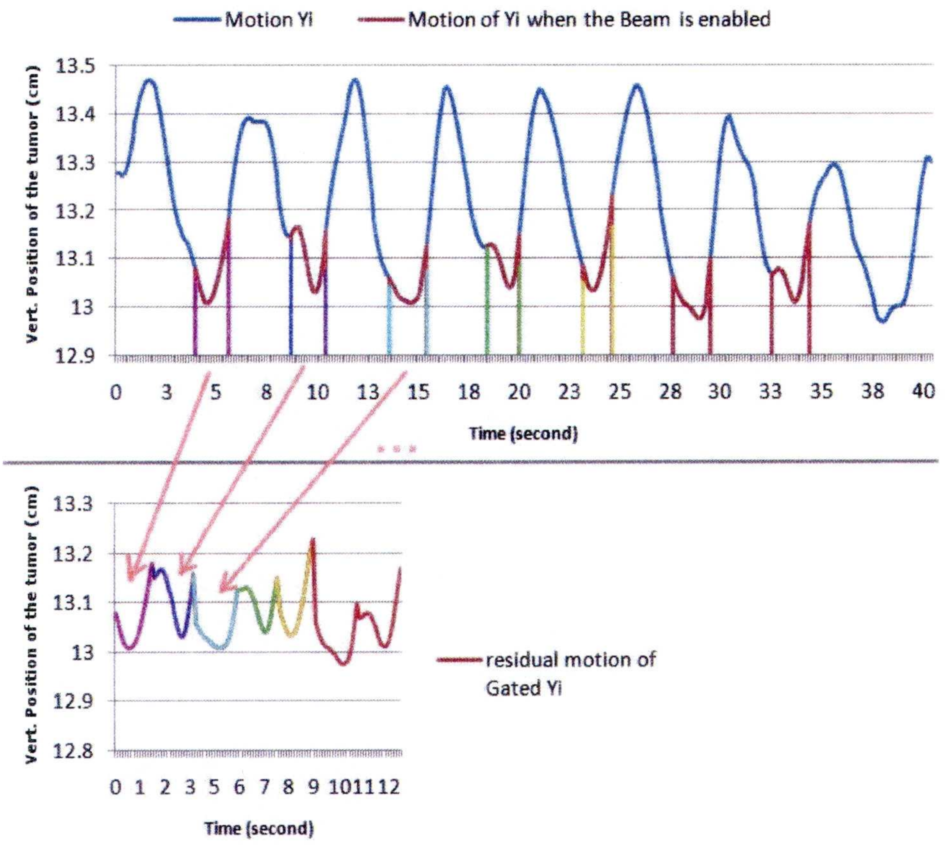

Figure 4-7: This diagram illustrates the formation of the residual motion series.The blue trace of the upper chart shows the sagittal position(Y-coordinate) of the tumour of one of the sessions. The vertical axis is the position of the tumour and the horizontal axis is the time in second(s). The red trace segments of the upper curve indicate the position of the tumour when the beam is enabled. On the lower chart, the beam-enable segments are truncated together and form the residual motion series. The colours (magenta, purple, cyan, green and yellow) of the segments are used to indicate the truncation of different segments.

In Figure 4-7, the upper trace is the sagittal position of the tumour over time. This can be called "the Total motion" of the tumour. The lower trace is formed by the position (motion) of the tumour when gating is used and the beam is enabled. This can be called "the residual motion of gating". The efficiency of the gating technique can be evaluated by the RMS of residual motion about its mean position in the gating window.

When comparing the effect of different gating parameters over a group of patients, the Total motion (RMS of the tumour motion Y_i as shown in the blue curve of Figure 4-8) was used as a factor for normalizing the residual motion of gating.

When the relative Root mean square value (rRMS) of motion is zero, gating removes all the motion of the target. When the relative standard deviation of motion is one, gating makes no difference as gating is disabled. The relative standard deviation of motion of gating rRMS of an internal motion y_i using gating modality x_s is defined as:

$$rRMS = \frac{std(\,G(y_i, x_s))}{std(\,y_i)}$$

where std() is a function returning the standard deviation of a series, y_i is the series of positions of the internal structure, $G(y_i, x_s)$ is a series of residual motion of gating when x_s is used as the breathing signal.

For tumour motion, the relative standard deviation of motion rRMS is calculated by:

$$rRMS = \frac{\sqrt{std(\,G(y_{TX}, x_s))^2 + std(\,G(y_{TY}, x_s))^2}}{\sqrt{std(\,y_{TX})^2 + std(\,y_{TY})^2}}$$

where std() is a function returning the standard deviation of a series, y_{TX} is the series of horizontal positions of the tumour, y_{TY} is the series of vertical positions of the tumour, $G(y_{DX}, x_s)$ is the residual horizontal motion of gating when x_s is used as the breathing signal and $G(y_{DY}, x_s)$ is the residual vertical motion of gating when x_s is used as the breathing signal.

4.2. Results and Discussions:

4.2.1. Internal motion

Figure 4-8 shows the RMS of motions of internal organs in all the 12 sessions measured by the fluoroscopy image sequences.

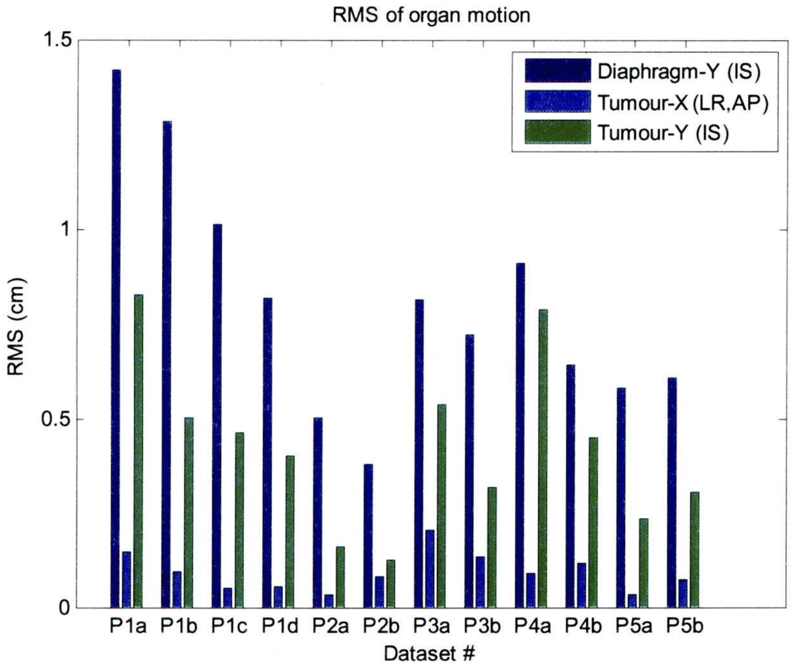

Figure 4-8: Motion of internal structures of 12 sessions. The RMS of Diaphragm-Y Inferior-Superior, Tumour-X (LR, AP) and Tumour-Y Inferior-Superior motions were shown.

The RMS value of the motions of the diaphragm ranged from 0.38 to 1.42 cm vertically. The RMS of the horizontal tumour motion ranged from 0.03 to 0.20cm (LR) and 0.05 to 0.13 cm(AP). The RMS of the vertical tumour motion ranged from 0.12 to 0.83cm.

Among all the datasets, extreme positions and fields, the RMS of IS motion of the diaphragm were larger than those of the tumour. The diaphragm's IS motion is on average 209% of the tumour's IS motion averaged over all natural breathing sessions. Patient-1 exhibited the largest amplitude internal motions. The average RMS of IS motion of the tumour and diaphragm of Patient-1 is 274% of Patient-2.

The result implies that the room for reducing residual motion of the residual motion of the tumour in the IS direction is large. In comparison with the magnitude of the IS motions, the horizontal motions (AP and LR) were not large. In Patient-4 (dataset-P4a and P4b on Figure 4-8), the tumour was located close to the diaphragm (Figure 4-9). The RMS amplitude of tumour IS motion was close to that of the diaphragm. It was therefore more likely to benefit from motion compensation techniques, due to the relatively large diaphragm movement.

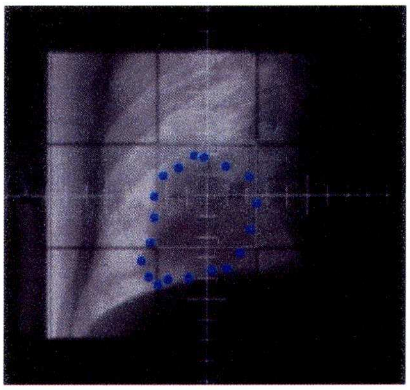

Figure 4-9: The location of tumour of Patient-4 was close to the diaphragm. As a result, the IS motion magnitude of the diaphragm was similar to that of the tumour.

4.2.2. Correlation of the ERM signal with the motion of internal structures

The delay and the correlation coefficient of the internal motions for the two different breathing monitoring devices are shown in Table 4-3 and Table 4-4. The values shown are the mean and standard deviation over all the 12 sessions of dataset.

Table 4-3: Delay of internal organ motions and different breathing monitoring devices (ERM and Varian RPM).The values are measured in seconds and a positive value means the time the device is lagging behind the internal motion.

Delay of internal organ motions and breathing monitoring devices		
Organ (direction)	**ERM (mean ±SD)**	**Varian (mean ±SD)**
Diaphragm (IS)	0.25 ±0.12	0.12 ±0.14
Tumour (LR)	0.18 ±0.10	0.06 ±0.10
Tumour (AP)	0.32 ±0.10	0.18 ±0.15
Tumour (IS)	0.34 ±0.11	0.20 ±0.16

Table 4-4Correlation coefficients of internal organ motions and different breathing monitoring devices (ERM and Varian RPM).

Correlation of internal organ motions and breathing monitoring devices		
Organ (direction)	**ERM (mean ±SD)**	**Varian (mean ±SD)**
Diaphragm (IS)	0.87 ±0.07	0.96 ±0.04
Tumour (LR)	0.69 ±0.12	0.73 ±0.13
Tumour (AP)	0.67 ±0.18	0.67 ±0.25
Tumour (IS)	0.81 ±0.07	0.90 ±0.09

Both breathing monitoring systems showed a significant time lag with respect to the internal motion. The ERM has a mean lag as large as 0.14 seconds behind the Varian RPM system. The tumour has a mean time lag of ± 0.07 seconds (depending on the direction) compared to the diaphragm.

There were 2 sets of data for each patient (4 datasets for Patient-1). Comparing the time lags within different datasets of any patient, the “breathing signal to motion signal” time lags were within 0.12 second in 4 out of the five patients. That means, the breathing monitors could maintain a stable synchronization with most of the patients. If a prediction algorithm were used it may be possible to compensate for the delay.

4.2.3. Variations of End of Inhale and End of Exhale positions

The variations in the extremes of movement were measured by the standard deviations of the EOE and EOI positions of the diaphragm and tumour motions. The results are shown in Figure 4-10. On the average, EOI had larger variations than EOE: 0.26 versus 0.11cm on the diaphragm and 0.17 versus 0.12cm on the of tumour (IS) motion.

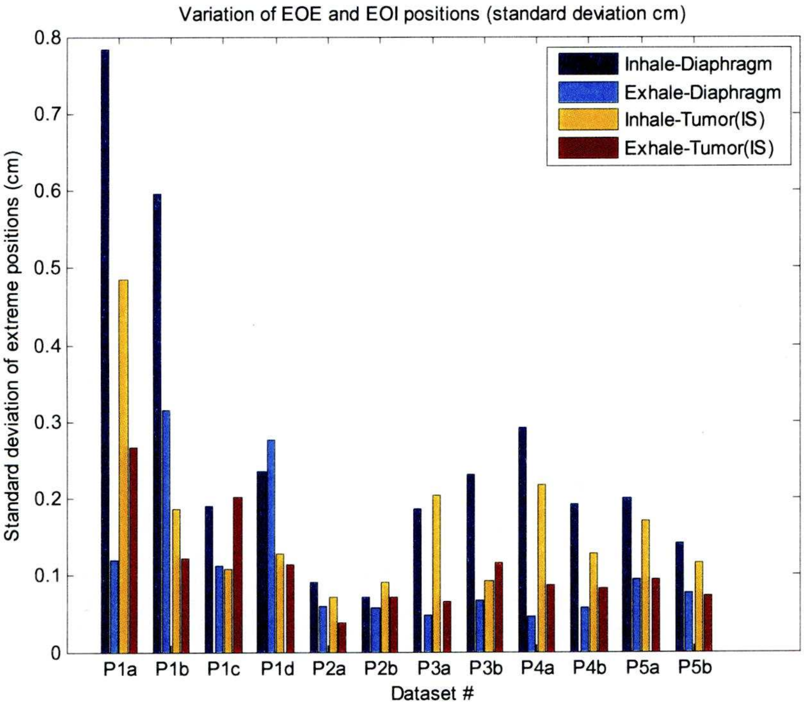

Figure 4-10: Standard Deviation of position of End of Inhale and Exhale positions of the diaphragm and tumour.

4.2.4. The impact of audio coaching visual feedback of Patient-1

Patient-1 had been audio coached with visual feedback. The study enabled us to compare the impact of the audio-coaching visual feedback technique with natural breathing.

According to the displacements of the diaphragm and the trajectory of tumour (P1a vs P1c and P1b vs P1d in Figure 4-8), the RMS of the total motion was reduced by a significant amount in all directions (Table 4-5).

Table 4-5: Reduction of Internal motions (RMS) when AV coaching was applied in two sessions of different imaging fields.

Percentage Reduction of Internal motion (RMS) by AV coaching			
AP field		**Lateral field**	
Organ (direction)	**% reduction**	**Organ (direction)**	**% reduction**
Diaphragm (IS)	27%	Diaphragm (IS)	36%
Tumour (LR)	65%	Tumour (AP)	42%
Tumour (IS)	44%	Tumour (IS)	20%

AV coaching reduced the variations of the EOI positions in the IS direction of both the tumour and the diaphragm. The reductions are showed in Table 4-6. However, there was no significant reduction in the variations in End of Exhale. The reductions of variations are shown in Table 4-7.

Table 4-6: Reduction of EOI variations when AV coaching was applied in two sessions of different imaging fields.

Reduction of EOI variations (cm)			
AP field		**Lateral field**	
Organ (direction)	**% reduction**	**Organ (direction)**	**% reduction**
Diaphragm (IS)	78%	Diaphragm (IS)	60%
Tumour (LR)	23%	Tumour (AP)	16%
Tumour (IS)	77%	Tumour (IS)	31%

Table 4-7: Reduction of EOE variations when AV coaching was applied in two sessions of different imaging fields.

Reduction of EOE variations			
AP field		**Lateral field**	
Organ (direction)	**% reduction**	**Organ (direction)**	**% reduction**
Diaphragm (IS)	6%	Diaphragm (IS)	12%
Tumour (LR)	-4%	Tumour (AP)	71%
Tumour (IS)	24%	Tumour (IS)	7%

4.2.5. Amplitude Gating Simulation

For a 20% duty cycle, the ERM reduced the average RMS amplitude of the diaphragm residual motion (over the 12 datasets) from 0.81cm (non-gated) to 0.33cm for EOI gating. When gating in the EOE position, the averaged RMS amplitude of the residual motion with gating was 0.26cm. The residual motion increased as the duty cycle increased.

The means (of 12 datasets) of the rRMS amplitude of the residual diaphragm and tumour motion across different duty cycles are shown in Figure 4-11a (for EOE positions) and Figure 4-11b (for EOI positions).

Both the Varian RPM and the ERM were effective for reducing residual motion, while the Varian RPM had an average of 10% further reduction in the rRMS.

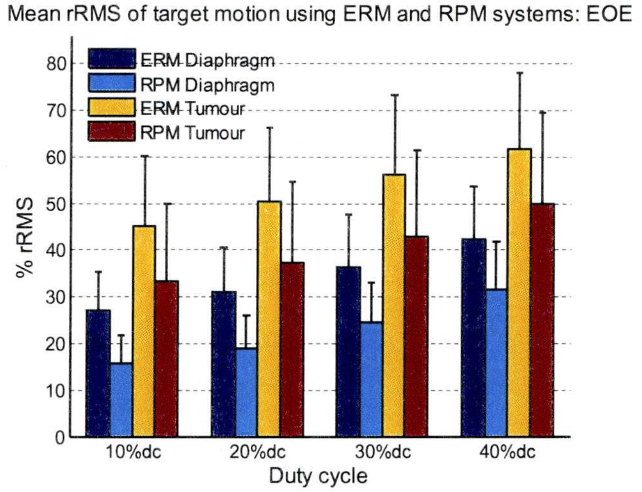

(a)

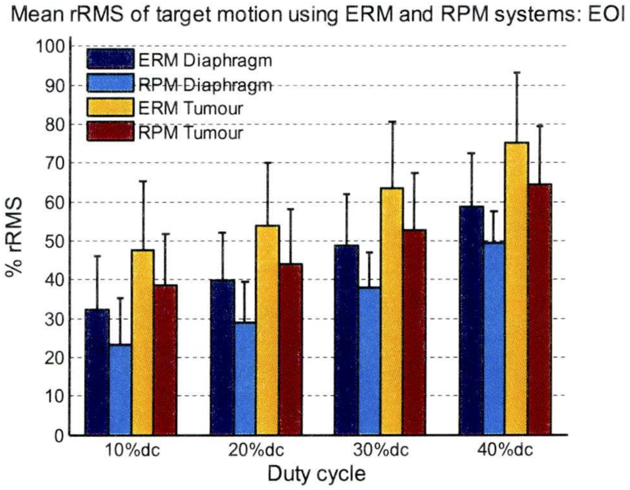

(b)

Figure 4-11: This diagram shows the mean of the rRMS amplitude of the residual diaphragm and tumour motion across different duty cycles using the ERM and Varian RPM systems. The height of the bars represents the % rRMS value. Bars are grouped into different duty cycles. The colour of the bar representing the kind of monitoring system and the phase position of gating. The error bars show one standard deviation. (a)Mean rRMS in the EOI position; (b) Mean rRMS in the EOE position.

Effects of Large (40%) and small (10%) duty cycle on the tumour motion in the SI direction.

Residual motion in EOE

The average difference between a 10% and a 40% duty cycle was 17%± 9% (measured by both devices).

Residual motion in EOI

The average difference between a 10%-duty-cycle and a 40%-duty-cycle was 28.1%±12% (measured using the ERM system) and 26%±10% (measured using the Varian RPM).

The differences in the rRMS for large and small duty cycles ranged from 5% to 60% rRMS, suggesting that some patients were more likely to benefit from low duty cycle, while for some of them the size of the duty cycle did not have significant impact (under the assumption that the tumour amplitudes are similar).

Table 4-8: The difference of rRMS between EOE and EOI measured by ERM and Varian RPM. A positive value indicate EOE has larger residual motion The value following the ± signs is the SD

Difference of rRMS residual motion of Tumour IS motion between EOE and EOI		
Duty cycle	**Reduction**	
	ERM	**Varian**
20%	-4%±18%	-7%±18%
30%	-8%±19%	-11%±20%
40%	-14%±19%	15%±19%

Gating in Exhale and Inhale

For duty cycles between 10% and 30%, EOE and EOI showed no significant difference. For higher duty cycles (40% duty cycle), the difference between EOI and EOE was also not significant, with an average 15%±20% more reduction. The different is caused by the variation in the EOI positions. An example of EOI variations of Dataset-P2a in 20% DC is shown in figure 4-12. In the dataset, the EOI positions have larger variations when compared to the EOE positions.

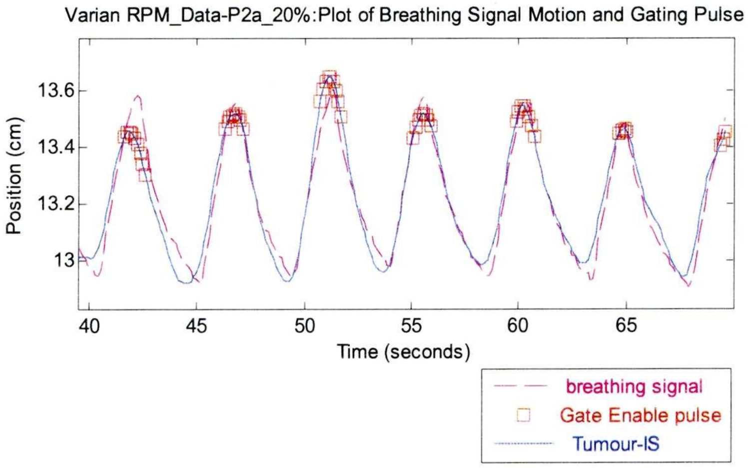

Figure 4-12: The variations of EOI. The Varian signal is shown in magenta and the gating signal by the red squares.

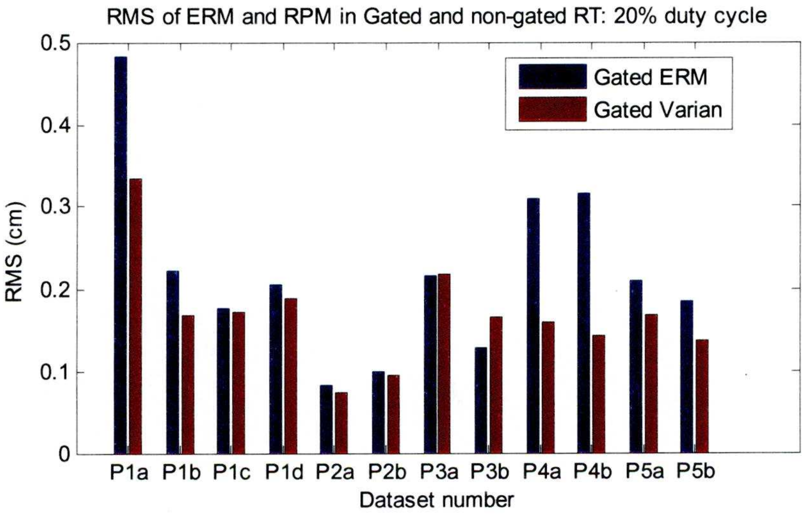

Figure 4-13: This diagram shows the RMS of the tumour motion with gating using the ERM and Varian RPM systems at the EOI position for a 20% duty cycle.

For most of the datasets, the differences in residual motion between the Varian and the ERM systems were not significantly different. There were some datasets which the difference in residual motion between the Varian and the ERM was significant.

To avoid repetition, the discussion here is focussed on the residual motion for a 20% duty cycle (figure 4-13). On average, the Varian RPM produces lower residual motion than the ERM ($p=0.02$). In particular, the difference between the two monitoring systems was large in Dataset-1a 4a and 5a. On average, in those datasets, the Varian RPM outperformed the ERM by a margin of about 0.15cm, but for the other datasets, the two systems produced equivalent results. The effect of the time lag between the two respiratory monitoring systems is shown in Figure 4-15.and Figure 4-12. The monitor signal (magenta curve) is shown in figure 4-15, the delay of the ERM signal (4-15a) caused the gating signal to be delayed relative to the motion, while the Varian RPM signal (figure 4-15b) was aligned accurately with the motion signal (blue curve).

The difference (ΔrRMS) of rRMS between the ERM and the Varian RPM versus the phase difference (Δt) between the two systems is shown in Figure 4-14. For each dataset, ΔrRMS is defined as the residual motion rRMS of the ERM minus that of the Varian RPM; while Δt is defined as:

Δt= the systematic delay between the Varian RPM and the tumour SI motion

- the systematic delay between the ERM and the tumour SI motion

The correlation coefficient between (ΔrRMS) and (Δt) was 0.67 ($p=0.017$) in the EOE and 0.83 ($p<0.01$) in the EOI. The correlation between ΔrRMS and Δt are shown in figure 4-14.

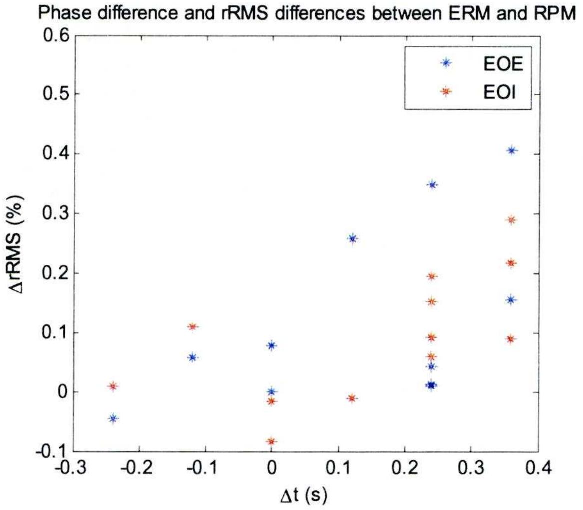

Figure 4-14: The relationship between the systematic delays and residual motion in 20% duty cycle on the EOE position.

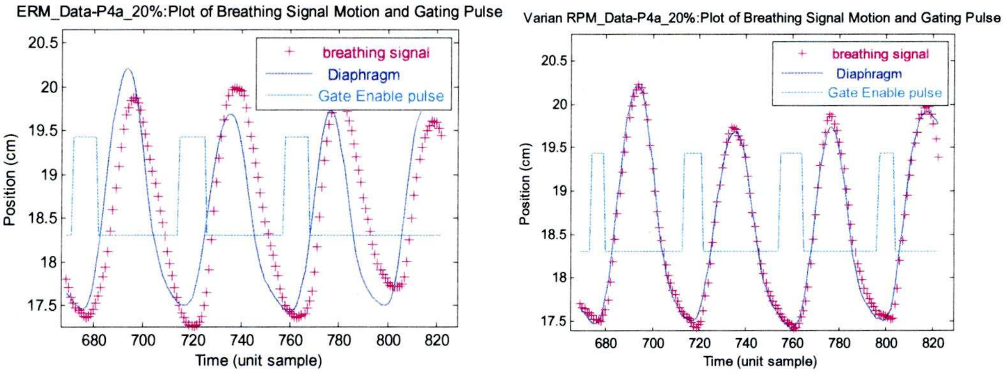

(a) (b)

Figure 4-15: A comparison of the monitor signal and amplitude gating signals between the ERM and the Varian RPM system for a 20% duty cycle on the EOE position. (a) shows the ERM's signal in magenta and the gating signal in cyan. (b) shows the RPM's signal. A delay is apparent in the ERM figure, in which the gating signal is shifted slightly towards the right hand side.

The ERM's breathing signal has an average delay of about 0.22±0.11 seconds compared to the diaphragm and 0.31±0.11 seconds compared to the tumour IS motion. As a result, the gating window did not include positions which were most stable during the breathing cycle. Another example of a systematic delay is shown in Figure 4-16, where the ERM's breathing signal (magenta in the upper chart) has a delay in relation to the diaphragm (blue in the upper chart), so that the gating window (cyan in the upper chart) is shifted towards the right hand side of the EOE position.

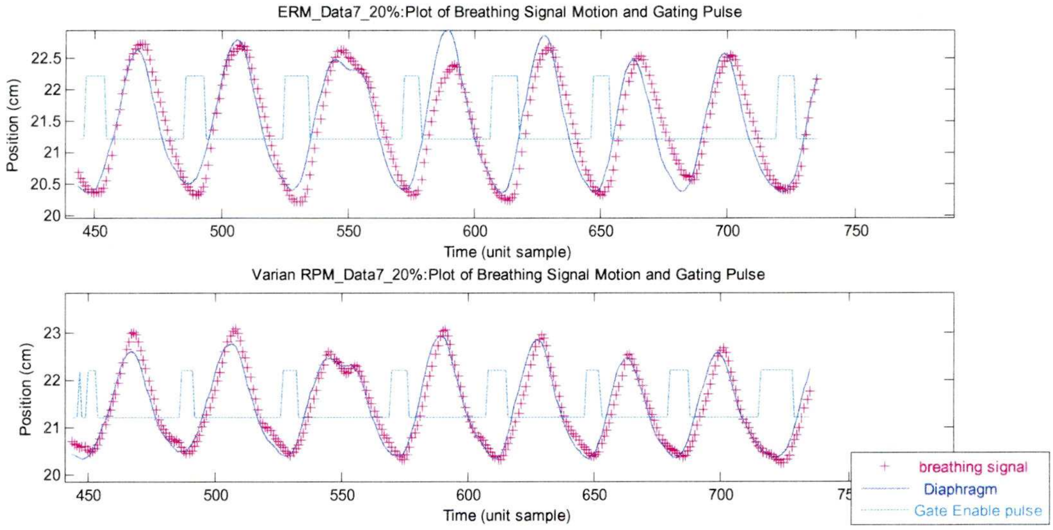

Figure 4-16: A comparison of the monitoring and gating signals for amplitude gating between the ERM and the Varian RPM system. The upper figure shows the ERM's signal in magenta and the gating signal in cyan. The lower figure shows the RPM's signal. A delay can be seen in the ERM figure, in which the gating signal is shifted slightly towards the right hand side.

To compensate for the systematic delay of breathing monitoring systems, prediction algorithms can be deployed to compensate for the delay. To estimate the effect of the systematic delay, the ERM signal was shifted with certain delay D_i for each dataset-i. D_i was obtained from the delay between the breathing signal and the internal motion in another dataset of the same patient. The rRMS of the residual motion using amplitude gating was evaluated for the shifted breathing signal. The results are shown in Figure 4-17. On average, we found that the time shifted signals could reduce the rRMS residual amplitude by an additional 4% to 12%. It was concluded that it would be possible to reduce the residual motion amplitude if prediction algorithms were used to compensate for the delay. A further investigation of prediction algorithms is in chapter 6 of this thesis.

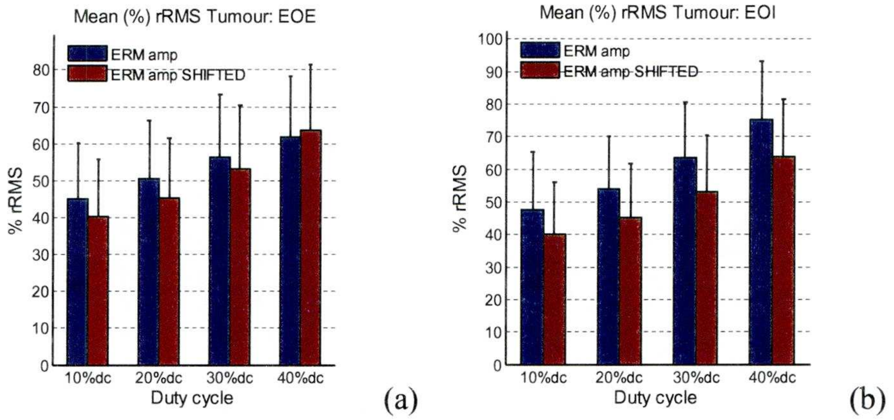

Figure 4-17: The blue bars are the mean rRMS organ residual motions over 12 datasets using amplitude gating without any delay compensation, while the red bars are delay compensated. The potential improvement associated with prediction algorithms is shown by the differences of each pair of bars. (a)Tumour EOE, (b)Tumour EOI.

4.3. Conclusion of the ERM in fluoroscopy study:

The results of gated radiotherapy simulations and the correlation between the breathing signal and the internal motion support the argument that the ERM was capable of reducing the amplitude of the motion of the target when the radiation beam was enabled. The degree of residual motion reduction associated with the ERM was than with the Varian RPM system in amplitude gating. This was because on the average, 1) the ERM has relatively lower correlation with the internal motion with the tumour and diaphragm, 2) the systematic delay.

For most of the patients, the EOE position has greater reproducibility, and therefore, gating at the EOE position yields lower residual motion. In Patient-1, audio and visual coaching significantly reduced the variation of the EOI and EOE, while the amplitude of total motion of the tumour was mildly reduced. As a result, the residual motion in amplitude gating was reduced by applying both audio and visual coaching.

5. Phase algorithm for ERM

5.1. Introduction

The ERM is sensitive to the rate of change in temperature. Therefore, if the respiratory frequency increases (and the amplitude of breathing remains unchanged), the amplitude would also increase. As a result, the amplitude of the breathing signal of the ERM may not be a good estimate of the tumour position of the internal organ. In such conditions, using phase gating may be more efficient than amplitude gating.

In respiratory gating, a reliable phase representation of the breathing motion is essential for the efficiency of gating. This is because the radiation beam is controlled by the gating signal and the gating signal relies on the phase signal which is derived from the amplitude of the breathing surrogate. The algorithm which is used to derive the phase from the amplitude signal of the surrogate affects the amount of residual motion reduction. For an absolutely noise-free and regular signal, the definition of phase is straight forward; one can measure the repetition duration between cycles and divide the lap time into equal portions. The portions, representing the state of the signal in a cycle, become the phase of the signal. However, in medical applications, especially for respiratory signals, the definition of phase is ambiguous, because the signal contains noise. When the noise distorts certain features of a signal, the phase is not easy to define. The variations of the EOE and EOI positions in a breathing signal are good examples of noise distortion in a breathing signal.

In this chapter, different approaches to Phase algorithms are investigated. An approach using the Fourier Transform and an approach using an Extended Kalman Filter (EKF) were investigated for deriving the gating signal for respiratory gating. The 12 datasets of the 5 patients of Chapter-4 were used to evaluate the performance of the phase algorithms.

5.2. Different Phase algorithms:

Most of the experiments rely on the built-in phase algorithm of the respiratory monitoring device to obtain the phase (George *et al* 2006, Chi *et al* 2006). Seppenwoolde *et al (*2002)analysed the hysteresis of tumour motion in different directions. The tumour motion was modelled by a power of 2n sinusoidal signal $\cos^{2n}(.)$, where n is a positive integer. The algorithm starts with identifying individual breathing cycles automatically by setting thresholds. For each individual breathing cycle, the amplitude, the position ofthe tumour in the inhale and exhale phases, the average tumour position, and the length of the breathing cycle were measured. The position s of the tumour as a function of time *t* can be defined as follows :

$$s(t) = s_0 - S\,cos^{2n}(\frac{\pi t}{\tau} - \phi)$$

where s_0 is the position of the tumour at exhalation, S is the amplitude, and hence s_0-S is the position at inhalation; τ is the period of the breathing cycle in seconds, and ϕ is thestarting phase. This parameterized breathing curve was fitted (using a least-squares method) through each average breathing cycle. However, it is difficult to perform curve fitting in real time, because the period and the amplitude of the current cycle is not known until the completion of the cycle.

5.2.1. Natural phase

Bogoliubov & Mitropolski(1961) developed a systematic approach to relate the amplitude and phase dynamics to the dynamics formulated in original phase space. The definition of an (instantaneous) phase proceeds by expressing the position x and the velocity v in polar coordinates A_N and ϕ_N:

$$x(t) = A_N(t)\cos(\phi_N(t)) \tag{5.1.1}$$

And

$$\dot{x}(t) = v(t) = -\omega A_N(t)\sin(\phi_N(t)) \tag{5.1.2}$$

, where ω is $\frac{d\phi_N}{dt}$.

It should be noted that a meaningful clockwise rotation in the x-v plane determines angles to be measured in a specific way depending on the sign of ω

The polar coordinate representation of the system is:

$$A_N(t) = \sqrt{x^2(t) + \frac{v^2(t)}{\omega^2}} \tag{5. 1.3}$$

$$\phi_N(t) = tan^{-1}\left(-\frac{\frac{v(t)}{\omega}}{x(t)}\right) \tag{5. 1.4}$$

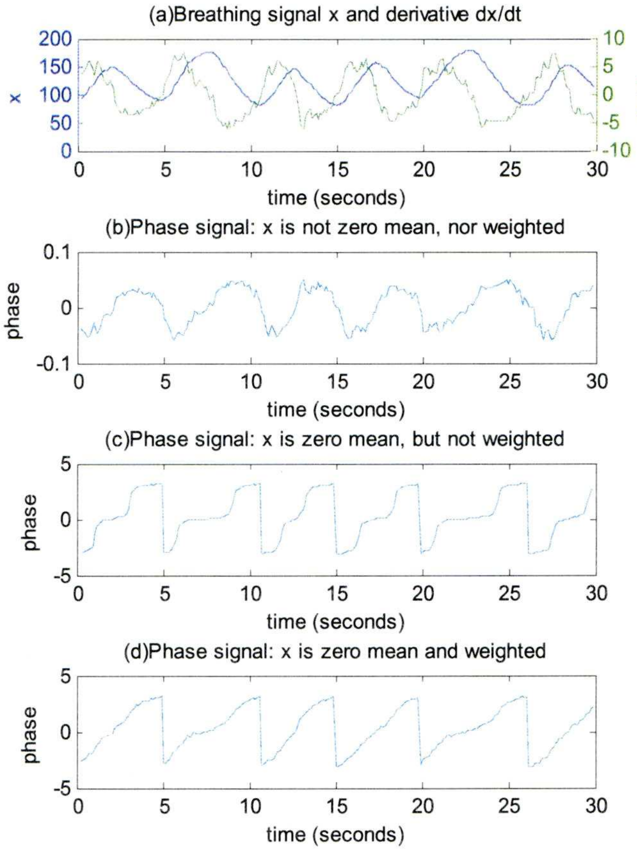

Key:[breathing signal x, derivative of x , phase]

Figure 5-1: The Breathing signal and the Natural Phase. (a)The upper chart is the respiratory signal x of a volunteer and its derivative dx/dt. (b)The second chart is the natural phase without a zero-mean x and proper weight between the two components x and dx/dt. (c)The third chart is the Natural Phase signal with a zero-mean x, but not properly weighted. (d)The fourth chart is the Natural Phase signal with a zero-mean x, and properly weighted x and dx/dt.

In order for the phase to be usable for radiotherapy, phase angles should be distributed linearly from $-\pi$ to $+\pi$ for a regular breathing signal Hence, the *x(t)* and *v(t)* components need to have zero mean and be weighted. A weight factor *w* is needed to balance the range of the numerator and denominator (in equation 5.1.4), such that their ranges are identical. If they are not, there will not be proper phase representation. An example is shown on figure 5-1. Suppose we have a breathing signal *x* and its derivative *v=dx/dt* (figure 5-1a). If the breathing signal does not have zero mean, the range of the phase angle would be too small and sometimes it progresses backwards (an example is shown in figure 5-1b, where $d\theta/dt < 0$ in the exhale phases). The physical meaning of a progresses backward phase is undefined. If the weight does not properly balance the ratio between x and v, the phase progression would not be linear (figure 5-1c). A proper phase representation of Natural Phase is shown in figure 5-1d.

The instantaneous phase of Natural Phase is given by:

$$\theta^{N}(t) = \arctan[\frac{\dot{x}(t)}{x(t) - \bar{x}} \cdot w] \qquad (5.\ 1.5)$$

where $\dot{x}(t) and\ x(t)$ are the breathing signal and its derivative respectively, $\bar{x}$ is the mean position of *x(t)* and *w* is a constant for balancing the weight of $\dot{x}\ and\ x$.

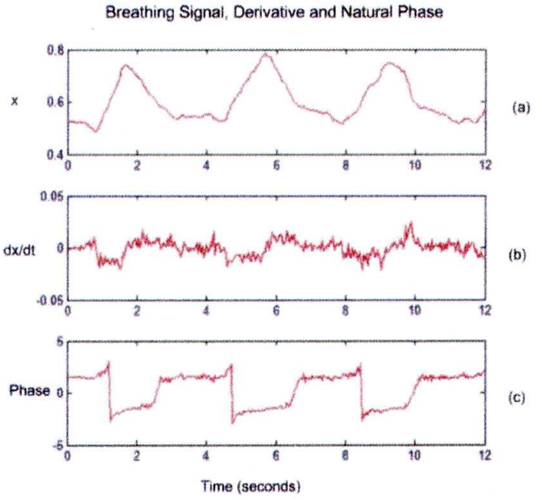

Figure 5-2: The Natural Phase. (a)The upper chart is the respiratory signal x of a volunteer which exhibited a relatively non-smooth breathing pattern. (b)The middle chart is the derivative dx/dt of the breathing signal. (c)The bottom chart is the Natural Phase signal. The signal was obtained by the Varian RPM system over a 1 minute sampling session. The first 12 seconds of the signal are shown here.

Since w is a constant, the phase is totally dependent on$\dot{x}(t) and\ x(t)$. In discrete signals, $\dot{x}(t)$ is often calculated by $x(t)-x(t-1)$. The phase will totally depend on the ratio of $x(t-1)$ and $x(t)$. The Natural phase algorithm is simple to operate, because only the current and the previous value of the breathing signal are needed to calculate the current phase. However, such simplicity makes it more sensitive to small and short term(high frequency) fluctuations in $\dot{x}(t)$. In a breathing sample (figure 5-2a) obtained from a healthy volunteer, the derivative of the breathing signal was not smooth (Figure 5-2b). In this case, the high frequency fluctuations in the derivative were relatively high and the breathing signal x(t) is far from a smooth sinusoidal signal. As a result, the natural phase is not a smooth and linear progressing function (figure 5-2c).

The problem of Natural Phase is that the instantaneous phase is derived by the ratio of the current value and its derivative. Hence, even if the breathing pattern is perfectly regular, the progression (dθ/dt) of the phase over time may not be constant. This results in the phase value not reflecting the stage of breathing.

5.2.2. Hilbert Phase /Analytic signals

The Hilbert transform offers a way to relate the signal $x(t)$ to an instantaneous amplitude and a phase. It has been used in chaotic systems for phase synchronization analysis (De Shazer *et al* 2001, Rosenblum *et al* 1996, Freund *et al* 2003). Analytic signals are signals without negative-frequency components. Hilbert Transformations are used to convert a real signal into an analytic signal. It is a system which produces the imaginary component bya phase shift of $\pi/2$ related to the real component. More specifically, if the input (figure5-3a) is a sinusoidal signal $x(t)=sin(\omega t)$, the output of the Hilbert transform y would be $y(t)=sin(\omega t + \pi/2)$ and the analytic signal x^a of x is $x^a(t)= sin(\omega t)+ jcos(\omega t)$.

The phase can be extracted from the polar expression of the analytic signal $x^a(t)= |A(t)|\, e^{j\omega t}$, where A is the amplitude and ωt is the phase. The transformation was calculated by finding the Discrete Fourier Transform of the input sequence, replacing the output coefficients that correspond to negative frequencies with zeros, and following this by the inverse Discrete Fourier Transform.

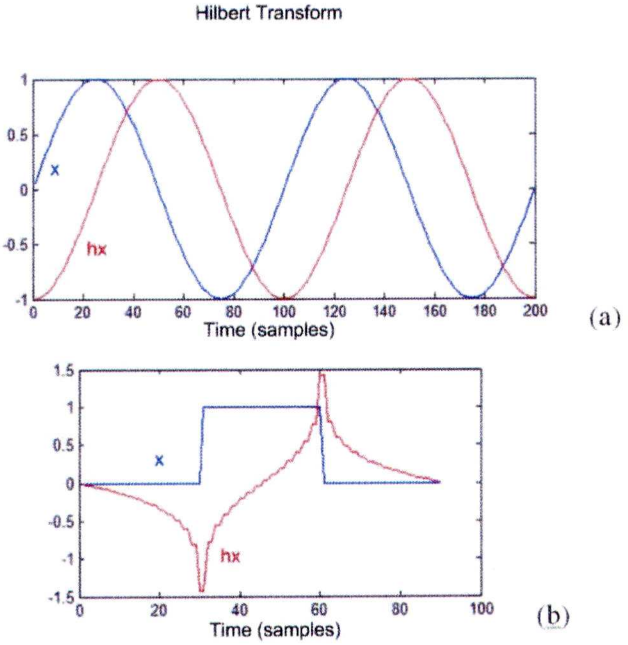

Figure 5-3: Hilbert Transform hx(red trace) of its original signal x. (a) sinusoidal signal (blue trace); (b)a square pulse (blue trace). The y-axis is the amplitude and the x-axis is the time axis.

5.2.2.1. Hilbert Transform

The aim is to find two orthogonal components to form a vector, which when time progresses, the vector goes around the origin. When the signal reaches the beginning of another cycle, the vector would have rotated a full circle about the origin.

To introduce the Hilbert transform, we start with two fundamental harmonic waves: the sine and cosine waves. The cosine spectral amplitudes are both positive and lie in the real plane (figure 5-4). The sine wave sequence has spectral components that lie in the Imaginary plane and are of opposite sign. If a sine wave sequence and cosine wave sequence combine and form a vector, the vector would go around the origin as described in the previous paragraph. Suppose the breathing signal is a cosine wave, the aim would be to derive a sine wave sequence.

In the Hilbert Transform, the negative frequency component of the cosine rotates by $+\pi/2$, while the positive frequency component rotates by $-\pi/2$. In other words, the positive component is multiplied by $-j$, while the negative component is multiplied by j.

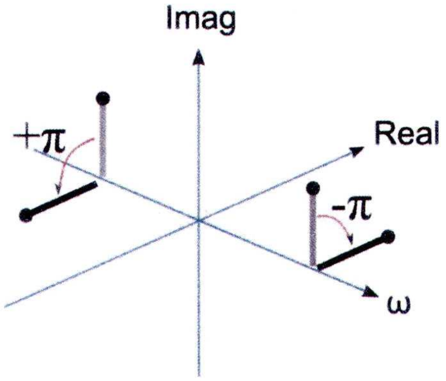

Figure 5-4: Hilbert Transform: Rotating the frequency components to create a sine wave out of a cosine

By the Hilbert transform, all negative frequencies of a signal get a +π/2 phase shift and all positive frequencies get a -π/2 phase shift. For any signal $x(t)$ in the Time Domain, its Hilbert Transform has the following property

$$\mathfrak{H}(X(\omega)) = -j\ sgn(\omega) = \begin{matrix} -j & for\ \omega > 0, \\ j & for\ \omega < 0 \end{matrix} \qquad (5.\ 1.7)$$

where $\mathfrak{H}$ *[ ]* is the Hilbert Transform operator, $X(\omega)$ is the Fourier transformation of $x(t)$, ω is in unit of frequency.The frequency components plot of the transform system is shown in Figure 5-5b.

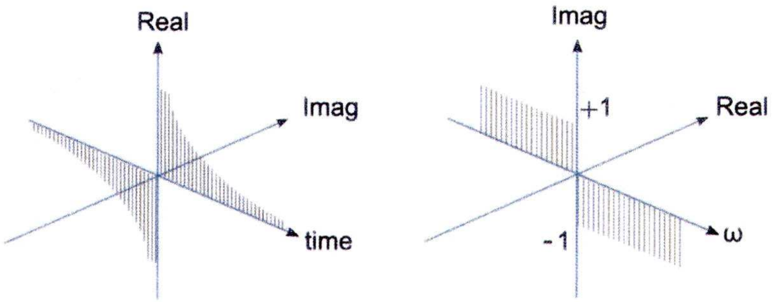

(a) (b)

Figure 5-5: The Hilbert transformation impulse response function in (a) time domain and (b) frequency domain. Hilbert Transform shifts the phase of positive frequencies components by -π/2 and negative frequencies components by +π/2.

5.2.2.2. Hilbert Phase:

The analytic signal approach extends the real signal $x(t)$ to a complex one

with the imaginary part $y(t)$ resulting from an appropriate transformation of the real part $x(t)$. Instead of taking $y(t) = c \cdot \dot{x}(t)$as for the natural phase algorithm, $y(t)$ is the result of a convolution of $x(t)$ with the Hilbert kernel $\mathfrak{H}$:

$$\mathfrak{H}(t) = \frac{1}{\pi t} \qquad (5.\ 1.8)$$

The Hilbert instantaneous phase becomes

$$\theta^H = tan^{-1}(\frac{\mathfrak{H}[x(t)]}{x(t)}) \qquad (5.\ 1.9)$$

where $\mathfrak{H}[\,]$ is the Hilbert transform operator.

An analytic signal $x^A(t)$can be computed by DFT. The DFT transform $X^A(\omega)$ of $x^A(t)$ is given by:

$$X^A(\omega) = \begin{cases} 2X(\omega) & for\ \omega > 0, \\ X(0) & for\ \omega = 0, \\ 0 & for\ \omega < 0 \end{cases} \qquad (5.1.10)$$

where $X(\omega)$ is the DFT of $x(t)$.

The Hilbert transform is suitable for deriving the phase for signals which exhibit a lot of irregularity where it is not clear how to define the phase (Freund *et al* 2003), and it is simple to operate from the signal processing point of view. This is because from Equation 5.1.0, the instantaneous phase can be calculated by computing its Discrete Fourier Transformation, zero substitutions, followed by inverse DFT and inverse tangent operation.

5.2.2.3. Edge Distortions

The transformation function of the Hilbert transform *h* with $h(t) = 1/(\pi t)$ is a non-causal filter (figure 5-5a). When causality is ignored and the input length of the transformation is infinite time, the variation of the instantaneous phase of the peaks and troughs appears small. Therefore, it has been widely used for retrospective analysis of time series.

One of the approaches to use Hilbert Transformation for real-time phase estimation is to select a wave segment for input. This is known as the windowing technique (or overlap technique as described in Rabiner 1975), which specifies a window as the input for Fourier Transformations. The Analytic signal approach utilizes the Discrete Fourier transformation (DFT), so it is also subject to the limitations (and related solutions) of the DFT.

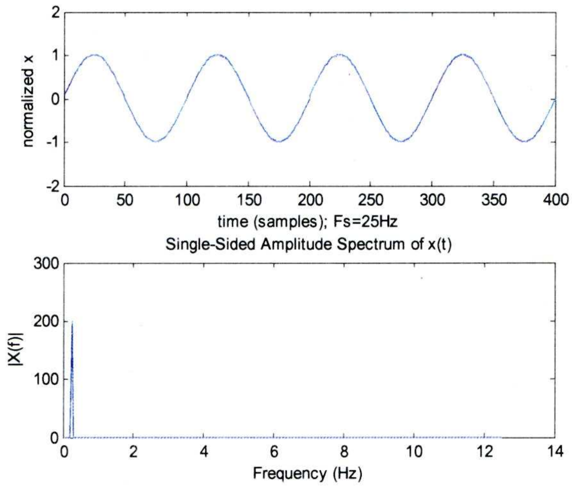

Figure 5-6a: The upper chart is a sine wave with a period of 4 seconds sampled at 25Hz sampling frequency. Four full harmonics of 400 samples were taken for the Fourier Transform. The spectrum is shown in the bottom chart, where a sharp component of 0.25Hz is found.

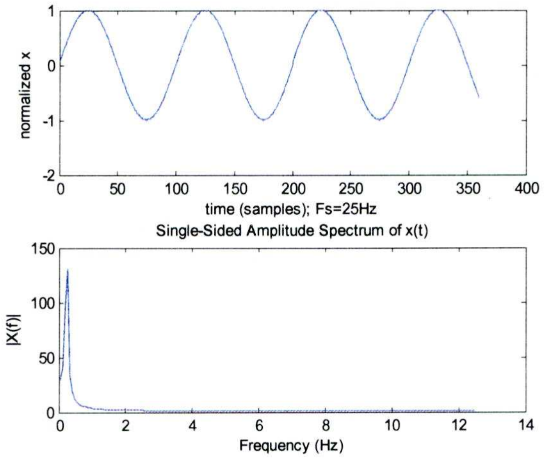

Figure 5-6 b: The upper chart is a sine wave with a period of 4 seconds sampled at 25Hz sampling frequency. 360 samples were taken for the Fourier Transform, accounting for 3.6 harmonics. The spectrum is shown in the bottom chart. The spectrum of the signal is spared around the 0.25Hz.

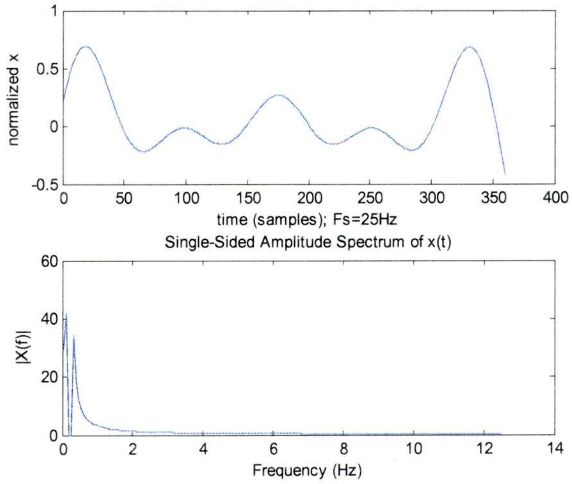

Figure 5-7: The upper chart is a sine wave with a period of 4 seconds sampled at 25Hz sampling frequency. With the frequency components corresponding to 0.25Hz removed. 360 samples were taken for the Fourier Transform, accounting for 3.6 harmonics. The spectrum is shown in the bottom chart.

The window size is an important factor in controlling the amount of distortion. For every segment of signal, the Fourier Transform works as if the data were periodic for all time (Rabiner 1975).Figure 5-8 shows the scenario measuring a signal for a period of time incorporating a few cycles (as for the windowing technique); the DFT works as if the data were periodic for all time. In Figure 5-8a, it happens that the signal is periodic and regular, but an integral number of cycles does not fit into the sampling window. (The sampling duration is shown in figure 5-8b). This means that, when the DFT assumes that the signal repeats (figure 5-8c), the end of one signal segment does not connect smoothly with the beginning of the next - the assumed signal is similar to the actual signal, but has 'glitches' at regular intervals.

If an integral number of cycles fit into the total duration of the input of a Fourier Transformation, then when the transform assumes the signal repeats, the end of one signal segment connects smoothly with the beginning of the next and the assumed signal happens to be exactly the same as the actual signal. An example of this is shown in Figure 5-6a, where the window size is a multiple of the period of the signal.

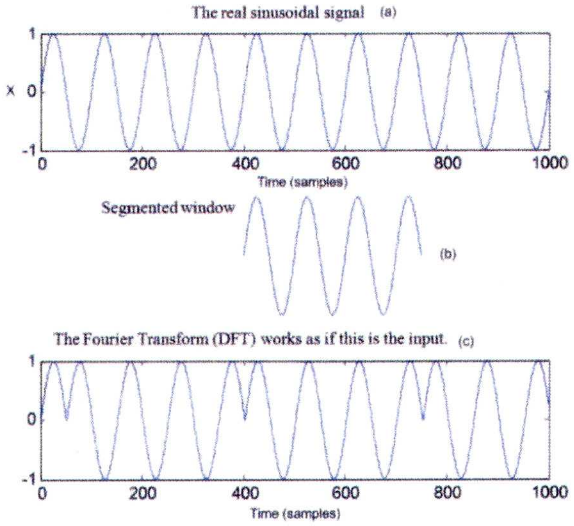

Figure 5-8: Assumption of Fourier Transformation. (a)The sinusoidal wave is a real signal, which has infinite duration. A window is defined for segmenting the real signal for real time processing. (b)The input signal (the middle sinusoidal wave) is periodic - but an integral number of cycles does not fit into the total duration of the measurement. (c)Hence, when the Fourier Transform assumes that the signal repeats, the end of one signal segment does not connect smoothly with the beginning of the next - the assumed signal is similar to the actual signal, but has little 'glitches' at regular intervals.

If not quite an integral number of cycles fit into the total duration of the measurement, then when the Fourier Transform assumes the signal repeats. However, the signal segments do not cascade smoothly. An example of this is shown in Figure 5-6b, where the window size is not an integer multiple of the signal period. In this case, the window size is 360 samples, while the period of the signal is 100 samples (0.25Hz frequency). A extended spectrum is observed in the bottom chart of Figure 5-6b. To show the effect of the window size mis-match, the frequency component of the 0.25Hz sinusoidal signal is removed from the spectrum, as shown in the bottom chart of Figure 5-7. The signal is reconstructed from its spectrum and shown in the upper chart of Figure 5-7. The reconstructed signal is the sum of all the harmonics excluding the 0.25Hz frequency. Due to the relatively high power (Figure 5-8) over the two tails, it distorts the representation of the phase at the two tails of the signal because the phase representations are affected by the dynamics of the extended frequency components which are far different from the original frequency (0.25Hz) of the real signal.

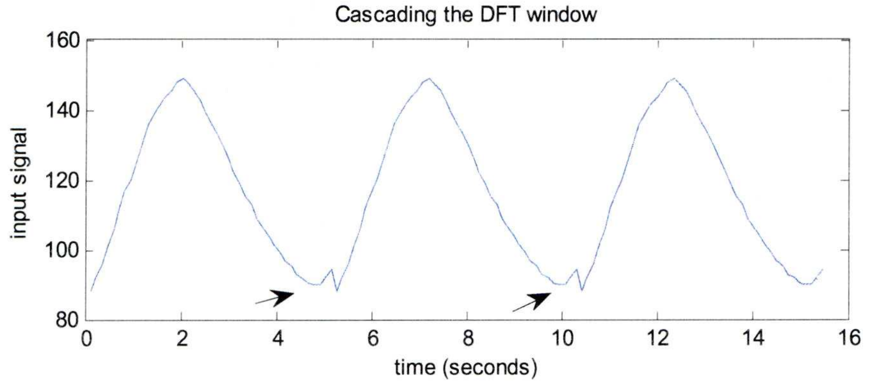

Figure 5-9: The input signal of the DFT. The DFT assumes the signal repeats. The transformation windows are cascaded (connected together) one by one. The end of one signal segment does not connect smoothly with the beginning of the next. The little 'glitches', are connection positions, marked with black arrows.

In gated radiotherapy, the phase of the breathing signal is derived in real time (or close to real time, but with a certain delay). The transformation window always starts at a certain time in the past and ends at the current moment. Only the instantaneous phase is of interest for triggering the treatment beam. Hence, the edge distortions described above affect the accuracy of the current phase, because the current phase is always at the edge of the window.

However, even if the window size perfectly matches the breathing period; the edge at the beginning of the window might not match the edge at the end (figure 5-9). Therefore, a low pass filter is needed to smooth the edges and the approach of using the Hilbert transform to estimate instantaneous phase (in real time) would become complicated to implement. Despite this, the Hilbert transform remains one of the best algorithms for offline (retrospective) phase estimation.

5.2.3. Multi-frequency tracker using Extended Kalman Filter

Based on the Kalman filter which was developed in 1960 by R.E. Kalman, the ExtendedKalmanfilter (EKF) was specifically developed for non-linear systems. It has been used in navigation (Cooper and Durrant-Whyte 1994), computer vision (Baumgartner1994), and in the estimation and tracking of signal problems (Brown 1983) for many years. It has the desirable quality of maintaining the physical meaning of the system dynamics by utilizing a state space representation.

In using the EKF to estimate the instantaneous phase of the breathing signal, we assume that the breathing signal is generated by a non-linear dynamic system model without a control input. At each point in time, the true state of the system being monitored will be denoted by x_k, where k is the time index.

$$x_k = f\ (x_{k-1}) + q_{k-1} \tag{5.2.1}$$

Here $f(.)$ is a nonlinear function and is a state transition matrix which describes how the state one time step earlier is transformed into the state at time k, and q_{k-1} is the normally distributed process noise with zero mean and covariance R.

The measurement z_k is the breathing signal and is formed through a non-linear function of the form:

$$z_k = h(x_k) + r_k \tag{5.2.2}$$

Here z_k is a measurement, $h(.)$ is a nonlinear function of the state x_k, and r_k is the measurement noise. The measurement noise is Gaussian with zero mean and covariance Q.

The EKF then provides us with an estimate m_k of the state at time k, along with an expected error of this estimate, expressed through a covariance P_k. Given a Gaussian estimate of the state specified by mean and covariance $<m_{k-1}, P_{k-1}>$ at time $k-1$, the EKF update rule provides us with an estimate of both quantities at time k.

The Jacobians of $f(.)$ and $h(.)$ are $F_x(m_{k-1})$ and $H_x(m_k)$, with elements:

$$\begin{aligned}[F_x(m_{k-1})]_{j,j'} &= \left.\frac{\partial f_j(x_{k-1})}{\partial x_{j'}}\right|_{x=m} \\ [H_x(m_k)]_{j,j'} &= \left.\frac{\partial h_j(x_k)}{\partial x_{j'}}\right|_{x=m}\end{aligned} \tag{5.2.3}$$

Here F_x and H_x are Jacobian matrices of $f(.)$ and $h(.)$, respectively, taken at the filter estimate m.

The resulting state transition and measurement functions are now linear in x. Hence, the EKF produces an exact update, by manipulating the various Gaussians involved. The update is then usually factored into two separate steps, a prediction step, and a measurement update step. The prediction step starts with the estimate m_{k-1} and its covarianceP_{k-1} at time $k - 1$, and produces an estimate for time t:

$$\begin{aligned} \overline{m}_k &= f\,(m_{k-1}, u_k) \\ \overline{P}_k &= F_x(m_{k-1}, u_k) P_k F_x^T (m_{k-1}, u_k) + Q_{k-1} \end{aligned} \tag{5.2.4}$$

The bar in $\overline{m}_k$ and $\overline{P}_k$ indicates that these estimates are pure predictions, before taking the measurement z_k into account. This happens in the measurement update step, in which the EKF integrates the measurement z_k by first calculating the Kalman gain:

$$\begin{aligned} K_k &= \overline{P}_k H_x^T (\overline{m}_k) S_k^{-1} \\ S_k &= H_x(\overline{m}_k) \overline{P}_k H_x^T (\overline{m}_k) + R_k \end{aligned} \tag{5.2.5}$$

This expression specifies the amount by which the estimate will be adjusted in accordance with the measurement prediction error $z_k - h\,(\overline{m}_k)$. This leads to the update of the mean and variance

$$\begin{aligned} m_k &= \overline{m}_k + K_k\,[z_k - h\,(\overline{m}_k)] \\ P_k &= \overline{P}_k - K_k S_k K_k^T \end{aligned} \tag{5.2.6}$$

The frequency tracker

Parker and Anderson (1990) used it as the framework for frequency, amplitude and phase estimation of the first mth components of a noise signal.

Consideranapproximatelyperiodic,non-sinusoidalsignal,inadditivewhite Gaussian noise. A non-sinusoidal signal may be considered to consist of an infinite number of sinusoidal components. Three sets of parameters can characterize the signal: the fundamental frequency, the amplitude of each harmonic component, and the phase of each harmonic component. The signal is not exactly periodic since frequencies, amplitudes and phases change slowly over time. Given a signal *y(t)* with zero d.c. component, has a slowly time varying frequency w_k, amplitudes r_k, and phases φ_k, a representation of this signal can be written as:

$$y(t) = \sum_{k=1}^{\infty} (r_k(t)\, sin(kw(t)t + \varphi_k(t))) \qquad (5.2.7)$$

where the quantities *w(t)*, $r_k(t)$ and $\varphi_k(t)$are the instantaneous frequency, amplitudes, and phases of the signal.

We assume for both models that the signal *y(t)* i s corrupted by noise. The measurement *z(t)* is given by:

$$z(t) = y(t) + r(t) \qquad (5.2.8)$$

where *r(t)* is the zero mean Gaussian noise with variance *R*.

The transition of state *x(t)* to state x(t+1)is given by:

$$x(t+1) = f(x(t)) + q(t) \tag{5.2.9}$$

where *f(.)* is the state transition function and *q(t)* is the zero mean Gaussian noise with variance *Q*.

And the state vector x is defined as:

$$x(t) = [r_1(t)\ldots, r_m(t), w\ \ (t), \varphi_1(t), \ldots \varphi_m(t)]^T \tag{5.2.10}$$

The Jacobian of *h(t)* is given by:

$$H(t) = \begin{bmatrix} sin(1 \cdot w(t) \cdot t + \varphi_1(t)) \\ sin(2 \cdot w(t) \cdot t + \varphi_2(t)) \\ \ldots \\ sin(m \cdot w(t) \cdot t + \varphi_m(t)) \\ \sum_{k=1}^{m} (r_k(t)\, cos(kw(t)t + \varphi_k(t))) \\ r_1(t) cos(1 \cdot w(t) \cdot t + \varphi_1(t)) \\ r_2(t) cos(2 \cdot w(t) \cdot t + \varphi_2(t)) \\ \ldots \\ r_m(t) cos(m \cdot w(t) \cdot t + \varphi_m(t)) \end{bmatrix} \tag{5.2.11}$$

The task is to estimate the values $r_1(t)$, ... $r_m(t)$,$w(t)$, $\varphi_1(t)$,... $\varphi_m(t)$ from the measurements, where m denotes the number of the significant harmonics. Parameters are only estimated up to the m^{th} harmonic. The higher harmonics are assumed to be negligible. A total of 2m+lparameters must be estimated.

Downsides of the EKF multi-frequency estimator

In both models there are some potential pitfalls of implementation. The first of these is that w can lock onto a fraction or multiple of the true frequency. For simplicity, we define $\hat{w}$ to be the actual value of instantaneous frequency w; $\acute{r}_k$ to be the true value of instantaneous amplitude r_k and $\acute{\theta}_k(t)$ to be the actual value of instantaneous phase $\theta_k(t)$(where $1 \leq k \leq m$). For suppose w locks onto $\frac{1}{2}\,\hat{w}$. Then, r_1 is around zero; r_2 tracks $\acute{r}_1$, $r_3$isnear zero, r_4 tracks $\acute{r}_2$ and soon. A similar case applies if $\hat{w}$ locks onto $w/3$. To solve this problem, we can check if $\acute{r}_k \cong 0$, and, if so, re-initialize with $\hat{w}$ twice (or three times) its previous value. Similarly, if $\hat{w}$ locks onto $2w$ then nothing tracks r_1, r_1 tracks $\acute{r}_2$, nothing tracks r_3, r_2 tracks $\acute{r}_4$ and soon. A remedy has been suggested by Parker and Anderson. Since the first, third and other odd harmonics are not being modeled, the state prediction error "$z_k - h\,(\overline{m}_k)$", will have greater energy than would be the case if $w \cong \hat{w}$. One can initialize a second filter with half the frequency estimate of the first: monitoring the prediction error of the two filters as well as the amplitude will tell one to reset the estimate $\hat{w}$ to half its previous value.

Another potential difficulty is cycle slipping, that is, for the estimated value of phase $\theta_k(t)$ and the actual value of phase $\acute{\theta}_k(t)$, for some k and t differing (approximately) by a multiple of 2π. In simulations of Parker and Anderson 1990, such cycle slipping was only observed at low Signal-To-Noise levels. Parker and Anderson suggested that slipping a cycle is probably of little consequence and can probably be ignored. However, in the case of radiotherapy, the phase is used to control the LINAC. An additional mechanism is vital to ensure the estimated phase is as close to the actual value as possible and reset the system if it goes wrong. The system can be initialized at the previous known state or the next known state. The maximum (EOI) and minimum (EOE) are easily detectable landmark states. The middle position is not as easily identified as the maximum and minimum, because the breathing baseline drifts. If the system were re-initialized from the next landmark position, there will be a time slot during which the system is offline and gives no response. This decreases the robustness of the system. On the other hand, if the system were re-initialized from the previous landmark states (which is the method we implemented), it requires that the states between the landmark and current position are re-estimated. To avoid interruption, this needs to be completed within one time step (of the order of tens to hundreds of milliseconds). If the sampling frequency of the signal is high, the system requires a considerable amount of computational power to handle the $(2m)^2$ computation complexity of the Kalman estimator.

5.3. The proposed Algorithms:

5.3.1. EKF phase estimation using Average Trajectory Function

We propose an Average Trajectory Function as a way to reduce the computational complexity of the Multi-frequency EKF estimator. The idea is that, instead of using multi-frequency sinusoid model, a mono-frequency average trajectory function is used. The average trajectory function maps the phase to an average amplitude. The average amplitude is obtained from the average trajectory of a training dataset of the same subject.

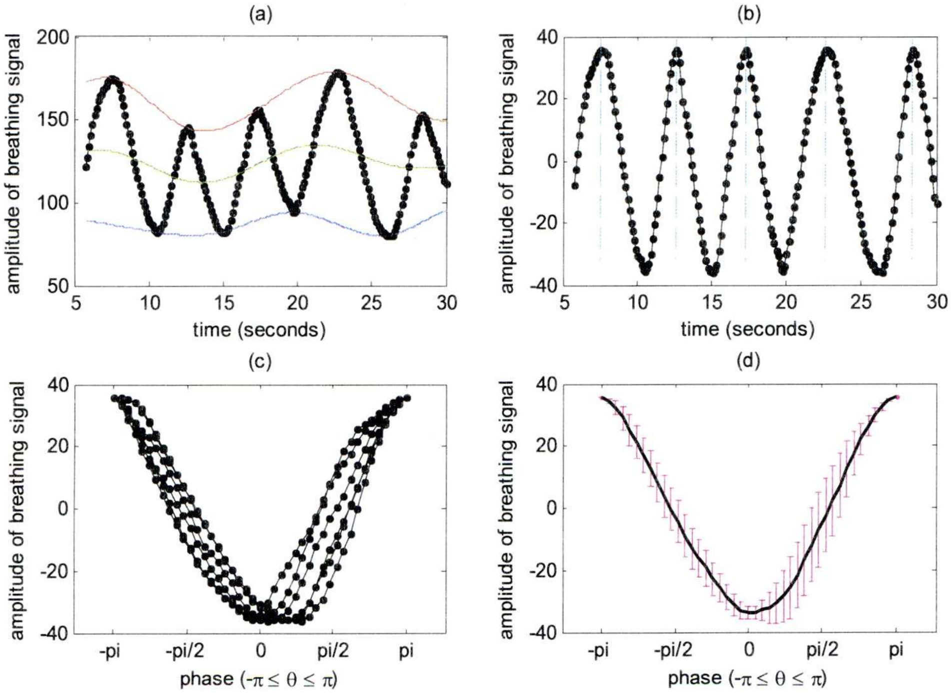

Figure 5-10: Stages of producing the breathing model (in the order from a to d). The ERM breathing of Patient-1 is used for demonstration. (a) A pair of cubic splines were used to connect the EOE (blue) and EOI (red) positions of the breathing signal (dotted black line). The green curve is the mean of the red and blue curves. (b)After the baseline drifting and amplitude variation is removed, the breathing signal is segmented into breathing cycles. (c) The breathing cycles were resampled, such that their lengths are equal, and represented by phase of –pi to pi (peak to peak). (d) The average trajectory (black curve) and standard deviation (magenta error bar) of all the breathing cycles.

5.3.1.1. A model to account for the inter-cycle breathing variations

The Average Trajectory model took into consideration the trajectory of breathing pattern from an EOI position to the next EOI position. Baseline drifting, amplitude and frequency variations were also taken into account. First, the baseline drifting and amplitude variations were modelled by cubic splines (Figure 5-10a). Second, the baseline drifting and amplitude variations were removed from the signal (Figure 5-10b). Third, in order to account for the variations in frequency, the average breathing cycle length Lb was calculated. Then, the breathing signal was segmented into breathing cycles. Fourth, the mean and standard variations of the duration of breathing cycles (wave-lengths) were calculated. Fifth, the breathing cycles were resampled into equal length segments by Cubic spline interpolation (Figure 5-10c). Sixth, the mean and standard deviation of every sampling point were computed (Figure 5-10d). The number of sampling points was chosen as the average breathing period (obtained in the third step) multiplied by the sampling frequency. Therefore, the resolution of the phase becomes 2 pi divided by the average cycle length and the sampling frequency. A phase (from $-\infty$ to $+\infty$) can be wrapped and then mapped to an average position by the Average Trajectory function. Since the Average Trajectory was represented by a discrete set of points, the Average Trajectory was interpolated for the mapping. Linear interpolation was used in this model because of the simplicity of the algorithm. However, a Discrete Cosine Transform can also be used to represent the Average Trajectory function. With a coefficient size of 20, the root mean square error (RMSE) of the Cosine Transform is less than 1% of the amplitude on all the training and testing signals.

The following parameters are included in the model:

- The Average Trajectory function
- The mean and rms values of:
  - The breathing cycle frequency
  - Every sampling point of the Average Trajectory.
  - Baseline spline
  - Amplitude variation

Reset mechanism

If the breathing pattern is too irregular and the EKF fails to track its phase, the phase estimator would reset and an alert is asserted if any of the following conditions is met:

- Instantaneous amplitude less than zero
- Instantaneous angular frequency less than zero
- The difference between the most recent peak (or trough) and the second most recent peak (or trough) is larger than RMS value of the signal.

Following the reset, the system would be re-initialized from the previous most recent peak (or trough) and recalculates the current state. The most recent peak (or trough) is detected by the peak detection algorithm described in Chapter-3.

5.3.1.2. The details of the modelling process:

The first step is to determine the baseline drift and the instantaneous amplitude of a breathing signal. Given a breathing signal x_a, the maximum (EOI) and minimum (EOE) points of x_a were located by the algorithm described in chapter 3. Three splines were computed: m_x connecting all the maxima, m_n connecting all the minima and m_i which is the mean of m_x and m_n. x_b is a signal with the variation of baseline and amplitude removed. x_b is given by:

$$x_b[k] = \frac{mean(m_x[k] - m_n[k])}{m_x[k] - m_n[k]} \cdot (x[k] - m_i[k]) \qquad (5.3.1)$$

where k is the index of the vectors.

The second step is to divide the breathing signal x_b into individual breathing cycles. x_b was then divided into segments(Figure 5-10b). Each segment is given by: $x_c[i,j]$, where $1 \leq i \leq N_i$ and $1 \leq j \leq N_j[i]$. N_i is the number of segments and $N_j[i]$ is the length of the i^{th} segment.

Each segment was then resampled to length N_L, where N_L is the average length of all the segments and $N_L = mean(N_j)$. The collection of equal length segments is represented by x_d. The mean trajectory x_e was calculated by

$$x_e[j] = \frac{1}{N_i} \sum_{i=1}^{N_i} x_d[i,j] \qquad (5.3.2)$$

for $1 \leq j \leq N_L$.

The third step is to determine the average trajectory of the breathing signal. The mean trajectory x_e becomes the parameters of the Average Trajectory function $x_f(\theta)$. x_f interpolates the x_e vector and maps a phase θ (wrapped by $\pm\pi$) onto the Average Trajectory. θ is given by:

$$\theta = 2\pi \cdot \frac{j-1}{N_L} - \pi \tag{5.3.3}$$

The mean trajectory is then normalized to the range of ±1.

The forth step is to determinate the parameters of the model. The breathing frequency variation g_L is measured by the standard deviation of the length of the breathing cycles normalized by its mean. It is given by:

$$g_L = std(\frac{1}{N_j \cdot \Delta t}) \tag{5.3.4}$$

where Δt is the sampling period.

The variation of the Baseline g_B is measured by the RMS of the rate of change of m_i which is the mean of the two splines connecting the EOI and EOE positions. It is given by:

$$g_B = rms\left(\frac{m_i[k] - m_i[k-1]}{\Delta t}\right) \tag{5.3.6}$$

$$for \;\; 2 < k < N_{mi}$$

where *rms(.)* is the function for calculating root mean square value and N_{mi} is the length of mi.

The variation g_A of the amplitude is measured by the RMS of the rate of change of the peak to peak amplitude *R* which is the difference between the two splines connecting the EOI and EOE positions. It is given by:

$$
\begin{gathered}
g_A = rms(\frac{R[k] - R[k-1]}{\Delta t}) \\
for\ \ 2 < k < N_R; \\
R = m_x[k] - m_n[k] \\
for\ \ 1 < k < N_R;
\end{gathered}
\tag{5.3.7}
$$

where *rms(.)* is the function for calculating root mean square value.

The parameters g_L, g_A and g_B were used for phase tracking using the Extended Kalman filter.

Kalman filter estimation requires complete knowledge of the dynamic system. The transition *f(.)*, the measurement function *h(.)* and the noise covariance matrices *Q* and *R* must be known. In this study, the breathing signal *y* is defined by following the model.

$$
h(x) = y \ \ = d + a \cdot x_f(\theta\ \ ) + r \tag{5.3.8}
$$

where *d* represents the drift of the baseline, *a* is the amplitude, $x_f(.)$ is the average trajectory function, θ is the phase and *r* is the Gaussian noise with zero mean and variance *R*.

The state vector *x* at time *k* is defined as:

$$
x_k = [\theta_k w_k a_k d_k]^T \tag{5.3.9}
$$

where d_k is the baseline drift, a_k is the amplitude, θ_k is the phase and w_k is the angular velocity. The phase θ_k is updated at each iteration. It is defined by:

$$\theta_{k+1} = \theta_k + w_k \cdot \Delta t \tag{5.3.10}$$

where Δt is the time step in seconds.

In continuous case the dynamics of the target's motion can be modelled as a linear, time-invariant system:

$$\frac{dx(t)}{dt} = \begin{bmatrix} 0 & \Delta t & 0 & 0 \\ 0 & 0 & 0 & 0 \\ 0 & 0 & 0 & 0 \\ 0 & 0 & 0 & 0 \end{bmatrix} x(t) + \begin{bmatrix} 1 & 0 & 0 & 0 \\ 0 & 1 & 0 & 0 \\ 0 & 0 & 1 & 0 \\ 0 & 0 & 0 & 1 \end{bmatrix} w(t) \tag{5.3.11}$$

where the white noise process *w(t)* has power spectral density Q_c:

The elements of Q_c and R are the product of the breathing model parameters (g_L, g_A and g_B) and weighting factors q_a q_b q_c q_d r_a. They are defined as:

$$Q_c = \begin{bmatrix} q_a & 0 & 0 & 0 \\ 0 & (q_b \cdot g_L)^2 & 0 & 0 \\ 0 & 0 & (q_c \cdot g_A)^2 & 0 \\ 0 & 0 & 0 & (q_d \cdot g_B)^2 \end{bmatrix} \tag{5.3.12}$$

$$R = r_a$$

The estimation of the weight factors will be described in the following section: chapter 5.3.1.3: Learning the Filter Parameters. The variables on the diagonal of Q_c describe the strengths of random perturbations of the phase, angular velocity, amplitude and baseline drifts respectively.

The state transition function *f(.)* defines as:

$$f(x_{k-1}) = F_x x_{k-1} \tag{5.3.13}$$

By referring to equation 5.2.1 the discretized form of the dynamic equation can written as:

$$x_k = \begin{bmatrix} 1 & \Delta t & 0 & 0 \\ 0 & 1 & 0 & 0 \\ 0 & 0 & 1 & 0 \\ 0 & 0 & 0 & 1 \end{bmatrix} x_{k-1} + q_{k-1} \tag{5.3.14}$$

Where q_{k-1} is the discrete Gaussian white noise process:

$$q_{k-1} \sim N(0, Q)$$

Following the manual of the Kalman Filter toolbox (Hartikainen and Särkkä 2008), the process noise covariance matrix Q is given by:

$$Q = C\, D^{-1}$$

where C and D is calculated by:

$$\begin{pmatrix} C \\ D \end{pmatrix} = \exp\{\begin{pmatrix} \mathbb{F} & LQ_cL^T \\ 0 & -\mathbb{F}^T \end{pmatrix} \Delta t\} \begin{pmatrix} 0 \\ I \end{pmatrix}$$

and

$$\mathbb{F} = \begin{bmatrix} 0 & 1 & 0 & 0 \\ 0 & 0 & 0 & 0 \\ 0 & 0 & 0 & 0 \\ 0 & 0 & 0 & 0 \end{bmatrix}; \quad L = I \tag{5.3.14}$$

The Jacobian of the state transition function F_x in equation 5.2.3 was defined by:

$$F_x = \begin{bmatrix} 1 & \Delta t & 0 & 0 \\ 0 & 1 & 0 & 0 \\ 0 & 0 & 1 & 0 \\ 0 & 0 & 0 & 1 \end{bmatrix} \qquad (5.3.14)$$

where Δt is the sampling period ($\Delta t = 1/Fs = 0.12s$).

The measurement function $h(.)$ and its Jacobian H_x were defined as:

$$h(x_k) = d_k + a_k \cdot x_f(\theta_k) \qquad (5.3.13)$$

$$F_x(x_k) = \begin{bmatrix} a_k \cdot x_f'(\theta_k) \\ 0 \\ x_f(\theta_k) \\ 0 \end{bmatrix}^T \qquad (5.3.14)$$

where d_k is the baseline drift, a_k is the amplitude and θ_k is the phase and $x_f(.)$ is the average trajectory function.

5.3.1.3. Learning the Filter Parameters

We now describe the learning techniques for obtaining the noise parameters of the EKF. The breathing patterns and variations are different for every individual. A training dataset is needed for every individual to determine its parameters.

The weighting factors were obtained by the "*patternsearch*" function of Matlab 2007b[7]. The "*patternsearch*" function finds the minimum of an object function with a given starting input vector and constraints. Pattern search operates by searching a set of points called a pattern, which expands or shrinks depending on whether any point within the pattern has a lower objective function value than the current point. The search stops after a minimum pattern size is reached. By the state transition function *f(.)*, the EKF is also capable of predicting the breathing signal. The best weighting vector was evaluated by minimizing the prediction error for 10 steps ahead. It has been assumed that the optimum parameters were judged by their ability to make the EKF algorithm accurately represent the current state. With an accurate current state, the future states prediction would yield less error and vice versa. The output of the object function (of *patternsearch*) was the RMSE of predicting 10 steps ahead. The ranges and initial-value vectors (of *patternsearch*) $s^0 = [q_a^0 \quad q_b^0 \quad q_c^0 \quad q_d^0 \quad r_a^0]$ were based on the manually tuned values of the signals of 9 healthy volunteers (of Chapter-3). The search ranges were within ±3 standard deviations of the weight vectors of the volunteers. All the elements of the weighting vectors are positive, so the range of the search space excluded negative values. By assuming that the elements of the weighting vectors are Gaussian distributed, the range covers 99.7% of the possible element values.

The initial vector s^0 was set as the average weight vector of the volunteers. It was calculated by:

$$s^0\,(j) = \frac{1}{N_v}\sum_{i=1}^{N_v} s^i\,(j) \tag{5.3.16}$$

where j is the index of the initial vector elements, i is the index of the datasets of the healthy volunteers, s^i is the weighting vector of the i$^{\text{th}}$ volunteer and Nv is the number of volunteers.

---

[7] The MathWorks, Inc. MA 01760-2098, UNITED STATES

In some pilot trial runs, the outcomes of the search function (final weighting vectors) despite being able to produce the minimum prediction error, failed to identify all the peaks. These "peak-miss" conditions happen when a sudden baseline drift takes place. In order to prevent peak-miss (or trough-miss) for a valid weighting vector, the phase difference θ_z between the first peak and the last peak of the unwrapped phase signal should be close to 2π multiplied by the number of wave cycles N_z. The difference should be smaller than π:

$$\theta_z - 2\pi \cdot N_z < \pi \tag{5.3.17}$$

If the criteria is not met, the output of the object function would be infinity. Hence, the parameter is rejected.

Let m_0 denote the initial state and P_0 denotes its covariance. The diagonal elements of P_0 were all set to 0.01 for simplification.

$$P_0 = \begin{bmatrix} 0.01 & 0 & 0 & 0 \\ 0 & 0.01 & 0 & 0 \\ 0 & 0 & 0.01 & 0 \\ 0 & 0 & 0 & 0.01 \end{bmatrix} \tag{5.3.18}$$

For every testing session, the EKF requires to have one breathing cycle (peak to peak) to warm up the system. During this time, the system determinates the initial state m_0. Hence, the first breathing cycle was not included in the evaluation. The initial phase θ_0 was $-\pi$ (as the prediction starts at the peak). The initial angular w_0 velocity was the angular velocity of the first cycle. The initial amplitude a_0 was that of the first cycle A_0 normalized by the amplitude A_m of the Average Trajectory function. The initial baseline drift d_0 was the baseline drift d_m (from zero) of the mid-position between the peak and the trough in the first cycle. The initial state vector m_0 was defined as:

$$\begin{aligned} m_o &= [\theta_o w_0 a_0 d_0]^T \\ \theta_o &= -\pi \\ w_0 &= \frac{2\pi}{L_0} \cdot F_s \\ a_0 &= (\mathbb{M}_x - \mathbb{M}_n)/2 \\ d_0 &= (\mathbb{M}_x + \mathbb{M}_n)/2 \end{aligned} \tag{5.3.19}$$

where L_0 is the duration of the first breathing cycle, Fs is the sampling frequency, A_m is the amplitude of the Average Trajectory function, A_0 is the amplitude of the first cycle, d_m is the baseline drift (from zero) of the first cycle, $\mathbb{M}_x$ is the position of the peak of the first cycle and $\mathbb{M}_n$ is the position of the trough of the first cycle.

5.3.2. Adaptive Windowing Autocorrelation Approach

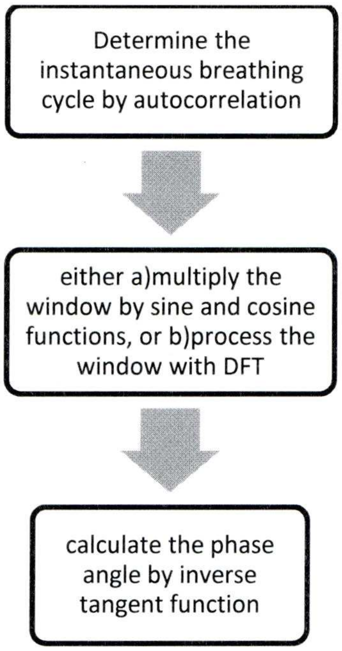

Figure 5-11: The flow chart of the Adaptive Windowing Autocorrelation Approach. The instantaneous phase is calculated by a 3 step process as: 1)determines the length of the transform window, then 2)multiply the window with sine and cosine function respectively and finally 3)calculate the phase by inverse tangent function.

The Adaptive Windowing[8] Autocorrelation (AWA) approach evolved from the Hilbert transform, but the Hilbert's complicated operations in real time phase estimation were simplified. Similar to the Hilbert Transform, the AWA approach also requires determining a transformation window such that the window includes one cycle of breathing. The autocorrelation technique is used to determine the size of the window. In the Hilbert approach, a low pass filter is required to smooth the signal in the window, because, in the presence of baseline drift and noise, the beginning of the window may not perfectly match the end of the window. This will lead to the edge distortion described in section 5.2.2.3. In the AWA approach, the windowed signal is transformed by Discrete Fourier Transform (DFT). We are only interested in the phase of the signal in which its wavelength matches the

---

[8] The term “window” in this section refers to the window for the input of Fourier Transformation. It is a segment of breathing signal including one or several breath cycles. It is different from the gating window which represents the time slots in which the radiation beam is enabled.

autocorrelation window. Therefore, the instantaneous phase is estimated by the phase of the first harmonic. The DC component and the higher harmonic components are neglected. A flow chart of the process is shown on figure 5-11.

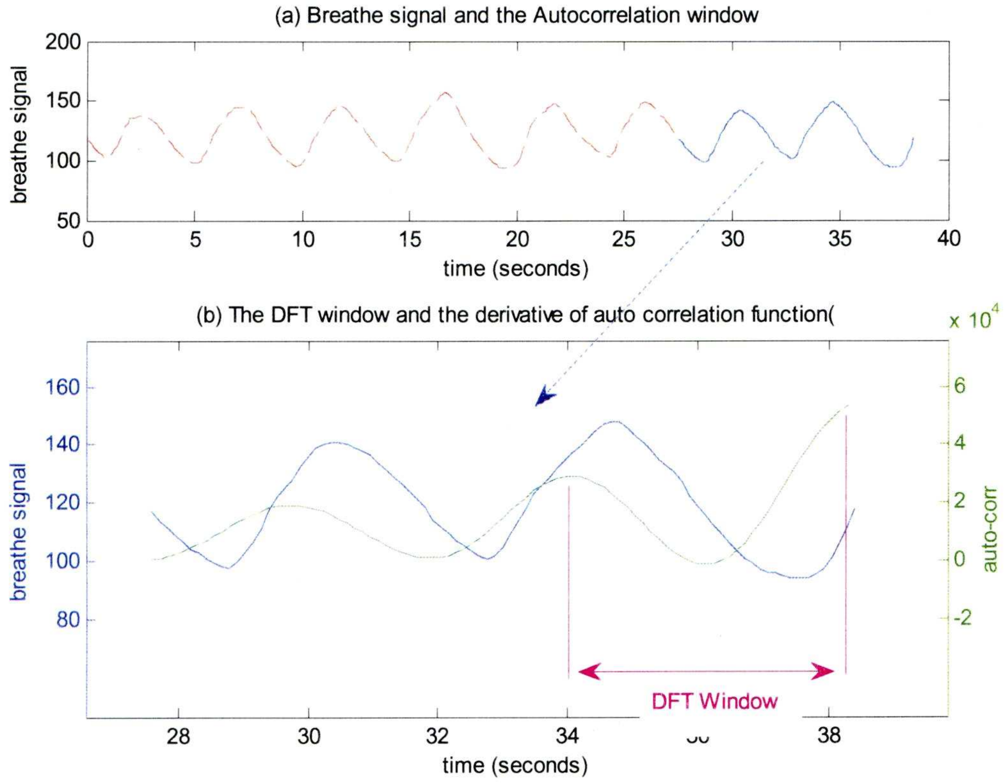

Figure 5-12: The AWA approach of phase estimation: (a)A breathing signal of 38 seconds is shown by the red dashed curve. The blue curve is the segment used for calculating the autocorrelation function. (b)The signal in the autocorrelation window is plotted by the blue curve. The autocorrelation function is plotted in green. The DFT window is defined by the 2^{nd} *peak (the magenta arrow) of the autocorrelation function. The phase of the first harmonic in the DFT window is the estimated phase.*

Autocorrelation

The window size could be adjusted in real time according to the instantaneous period of the signal. The aim of this was to adapt the window size to match the instantaneous period of breathing such that the edge distortion could be reduced. This was because the DFT assumed the input was from a random process where all of its statistical properties were time invariant. Signals whose statistical properties do change are referred to as nonstationary. Using the DFT implies that the finite segment that is analyzed is an infinitely extended periodic signal. Autocorrelation is the cross-correlation of a signal with itself. It has been used to find repeating patterns ineconometrics (Sentana and Wadhwani 1992) or in information processing such as the presence of a periodic pattern which has been buried under noise, or identifying the missing fundamental frequency in a signal implied by its harmonic frequencies (Gaydecki 2004). Suppose there is a breathing signal whose auto-correlation function (ACF) is derived from the ERM (figure 5-12a). When the current time is t=38.5s, we would like to search for a time which is about one cycle away from now. The ACF would reach its local maximum, when the time difference is about one cycle away from the current time. Since a breathing signal lasts for tens of seconds and all we need to determine is the period of the current cycle, it would be a waste of computation power to calculate the ACF of the whole signal. The length of the autocorrelation window was chosen to be 3 times the breathing period of the training dataset of the patient because there was no improvement in performance with longer windows. A longer autocorrelation window makes its size more close to the average breathing wavelength. On the other hand, a short window size might fail to detect the "peak" in slow breathing.

The DFT window size can also be analyzed by a Coherence Function in the frequency domain (in contrast to autocorrelation in the time domain). The Coherence Function gives a measure of the linear dependence between two signals as a function of frequency. The function has properties which are applicable to breathing signals: i.e. invariance to phase shift, change of amplitude and baseline drifting. To estimate the true instantaneous wave length, the previous breath cycle Cy_0 was identified (by peak detections) and compared it with the current cycle Cy_{now} (whose phase was different from the previous cycle Cy_0) using the Coherence Function. The goal was to find a window size for the current breath cycle Cy_{now} such that the signal had maximum coherence with the previous cycle Cy_0. The window size might not be the same length as the previous wave cycle; thus, interpolation might be needed to resize the signal Cy_{now} inside the window. Two parameters were required to estimate the true instantaneous wave length λ_{true}

of the current breath: (1) A successfully identified breath cycle Cy_0 and (2) and a range R_{true} for the searching space of wave length λ_{true}. R_{true} could be in the range from 0.5 to 2 times the length of the previous wave cycle Cy_0.

Fourier Transform

The length of the Fourier transform window was determined by detecting the adjacent local maximum of the current time (figure 5-12b). The signal inside the Fourier transform window was then processed by DFT. The phase of the current breath cycle is the phase of the first harmonic of the DFT. As a result, it becomes the final estimated phase.

In a mathematical form, the two orthogonal components of the phase were the dot product of the Fourier transform window with a sine wave and cosine wave (respectively). The instantaneous phase $\phi_A(t)$estimated by the AWA approach is given by:

$$\phi_A(t) = tan^{-1}\left(\frac{w_t[k]\cdot\psi_s[k]}{w_t[k]\cdot\psi_c[k]}\right),$$

$$\psi_s[\mathrm{k}] = \sin\left(\frac{2\pi}{N}\cdot(k-1)\right), \qquad (5.3.20)$$

$$\psi_c[\mathrm{k}] = \cos\left(\frac{2\pi}{N}\cdot(k-1)\right)$$

where $w_t[.]$ is the vector of the autocorrelation window, k is the index of the vectors ($1 \leq k \leq N$). $\psi_s[.]$ and $\psi_c[.]$ are the sine and cosine vectors and N is the length of the vectors w_t, ψ_s and ψ_c.

5.3.3. Different approaches of adapting to irregular breathing signals

Breathing signals vary in frequency, amplitude, baseline and trajectory pattern. The AWA adapts to the change of frequency by changing the size of the DFT window. When the DFT filtered out the frequency of the higher harmonic signals and the DC component, the variations in baseline and trajectory pattern were eliminated. In the inverse tangent transform, the amplitude variation is also cancelled. While the AWA approach removes (filters) information from the signal, the EKF keeps the information and trys to reduce the covariance among the system parameters (of frequency, baseline, amplitude and trajectory pattern). Moreover, the AWA estimates the phase of a complete breathing cycle. In contrast, the EKF estimates the phase of the current time step.

5.4. Experiment setup:

The subjects and datasets from Chapter4 were used for this experiment. The two proposed approaches were used to estimate the phase of the ERM breathing signal. The residual motions in phase gating were evaluated and compared with the amplitude gating result as in Chapter-4. There were 12 datasets from 5 patients.

The Hartikainen and Särkkä Matlab toolbox EKF/UKF (Extended Kalman filter/ Unscented Kalman filter) version 1.2 was used for EKF implementation. We used a dataset from the patient as training data to initialize and evaluate the filter parameters, and then tested the filter performance against the other datasets of the same patient.

Gating windows (phase gating)

In phase gating simulation, the beam was enabled when the phase θ of the breathing trace goes within the range of $\Theta-\check{R}$ and $\Theta+\check{R}$. A suitable mid-point Θ and range $\check{R}$ were used for each position(EOE or EOI) of gating and for each different duty cycle. We simulated10%, 20%, 30% and 40% duty cycles, which are the usual duty cycles used in clinical practice. By using pattern search algorithms ("patternsearch" function of Matlab 2007b), the mid-point of the gating window Θ and the range of the gating window $\check{R}$ were optimized such that the portion of beam on time (measured in %) was closest to the intended duty cycle (either 10%, 20%, 30% or 40%). Choosing the mid-point of the gating window Θ is of great importance for phase gating. Shifting the gating window from a relatively stable phase to a less stable phase would introduce more residual motion.

In this experiment, the mid-point of the gating window Θ was chosen from the corresponding training dataset. In a specific duty cycle, Θ was the value which could reduce the RMS of the residual motion of the diaphragm in the largest amount. The optimum value of the mid-point of the gating window Θ was evaluated within the range$\Theta_0\pm\frac{\pi}{2}$, where Θ_0 is the average phase of the extreme points. The mid-point $\Theta_0$would be close to $-\pi$ radians for EOI and close to 0 radians for EOE.

5.5. Result and Discussions

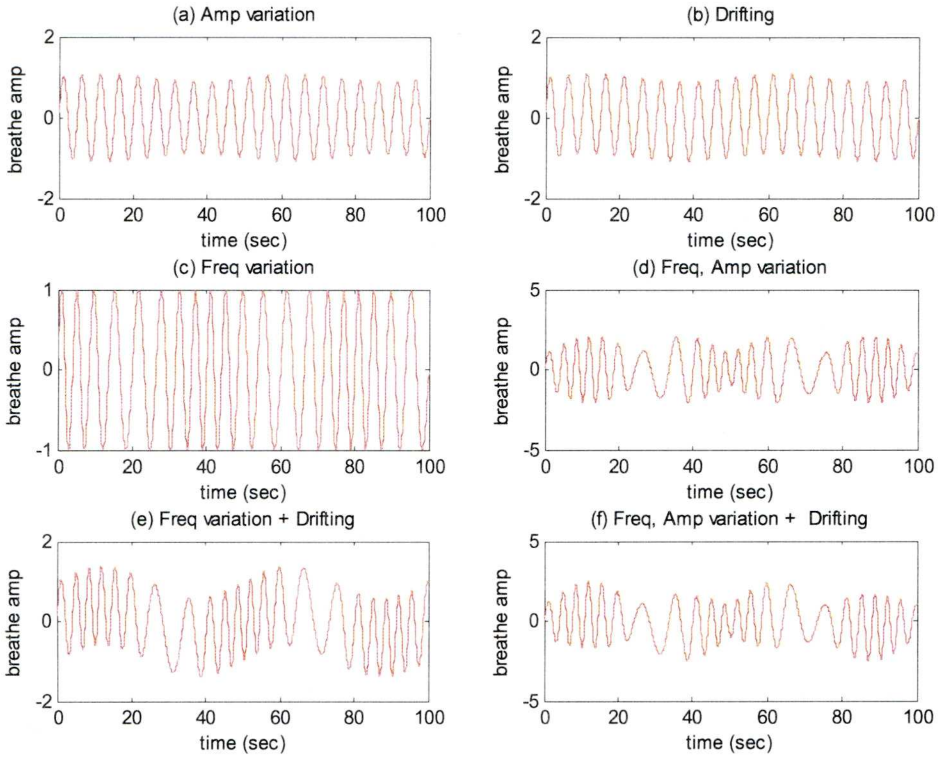

Figure 5-13: The sinusoidal waves used to simulate the breathing signal. (a) Amplitude variations only; (b) Base-line Drift only; (c) Frequency variations only; (d) Frequency and amplitude variations; (e) Frequency variations and baseline drifting; (f) Frequency-amplitude variations and baseline drifting.

Reliability of synchronization with the breathing signal

To present a first impression of the characteristics of the two phase estimators, the phase of a collection of different sinusoidal signals were estimated. The signals are shown in Figure 5-13. The set of signals are different combinations of amplitude variations, frequency variations, and drift. A signal with amplitude variations was used as the training dataset for the phase estimator. The approach taken to measuring the variation of the pattern was the same as in Chapter 3. The variation of breathing pattern of a signal was measured by the "sum of the standard deviation of the breathing patterns". The bin size was 20, which is two times the bin size of a 4D CT dataset (10 bins). The results are shown in table 5-1. For large variations (figure 5-13d, e & f), the phase derived by the EKF approach was less variable than that derived by the AWA approach (especially in the presence of frequency variations).

During the process of determining the system parameters, it has been found that the parameters have to be highly customized for the volunteers where the breathing was irregular. Hence, the AWA approach is more stable over the EKF approach owning to the recursive characteristics of EKF. Further investigation is needed to determinate the impact of a optimum set of parameters which would fit all different breathing conditions.

The sum of the standard deviation of the breathing patterns (Rs)		
	EKF	**AWA**
Amplitude variations	2.2	2.2
Baseline drifting	2.6	2.6
Frequency variations	1.9	5.4
Frequency and amplitude variations	4.7	10.2
Frequency variations and baseline drifting	7.6	10.8
Frequency-amplitude variations and baseline drifting	6.4	10.4

Table 5-1: The sum of the standard deviation of the breathing patterns (Rs) of the two phase estimators on sinusoidal waves. (Lower value is better)

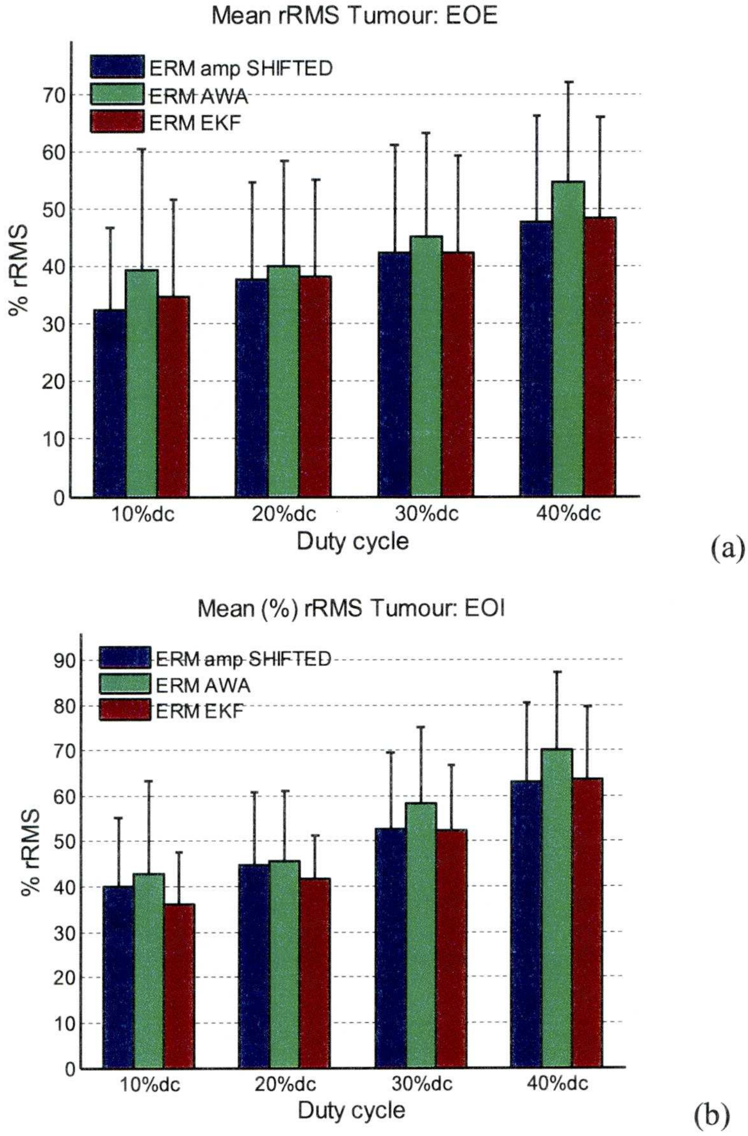

Figure 5-14: The relative root mean square values of residual motions averaged over the 12 datasets are shown on the figures. Each set of bars represents different duty cycles. The colours of the bar represent different phase estimation algorithms. The error bar shows the standard deviation. The upper figure a) is for gating at the EOE position and the lower figure b) is for the EOI position.

Residual Motions of gating simulations

The rRMS values of the residual motion of the tumour using the EKF and AWA approaches are plotted in figure 5-14. The upper figure (a) is for gating at the EOE position, while the lower figure (b) is for gating at the EOE position. The results are grouped into four sets of colour bars: each set of bars represents a different duty cycle (from 10% to 40%), while different colours represent different gating techniques:

- ERM amplitude gating with systematic delay compensation (for reference),
- ERM signal derived by the AWA approach
- ERM signal derived by the EKF Average Trajectory approach

The mean rRMS values of the diaphragm in phase gating are shown in figure 5-15, with the same format of representation as those of the tumour.

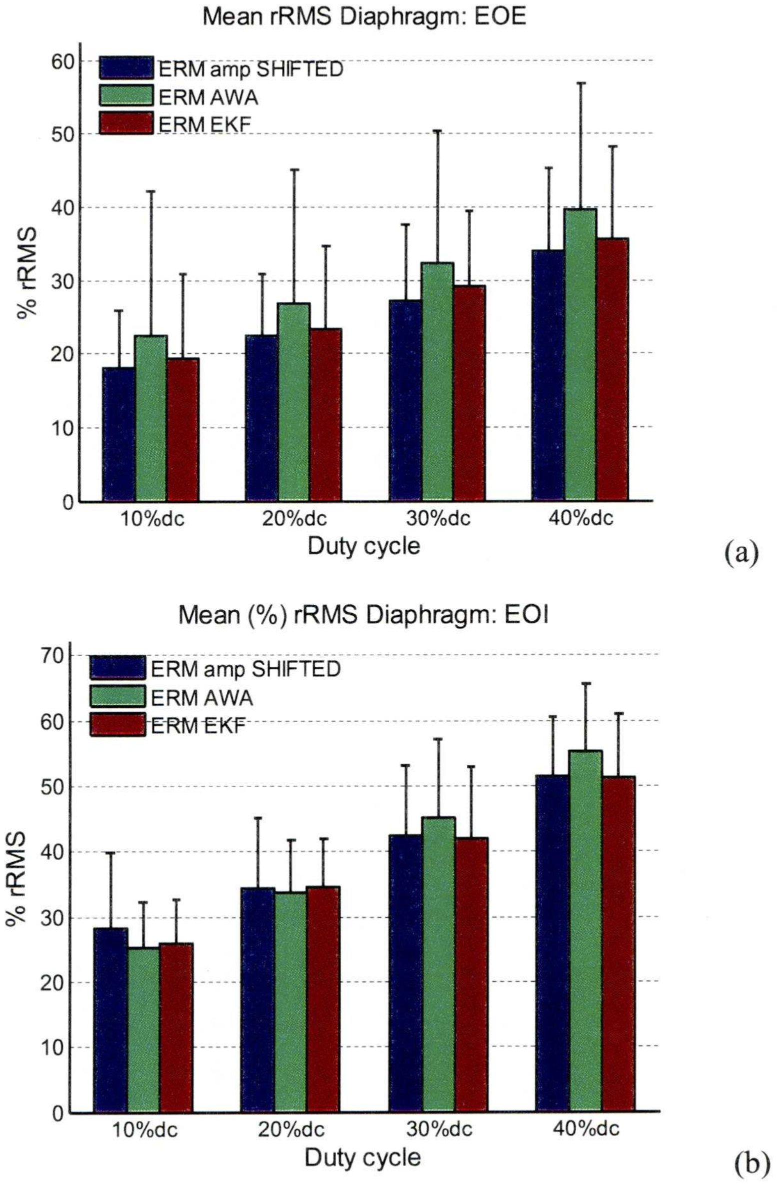

Figure 5-15: The rRMS over the 12 datasets are shown in this figure. Each set of bars represents different duty cycles. The colours of the bar represent different phase estimation algorithms. The error bar shows the standard deviation. The upper figure a) is for gating at the EOE position and the lower figure b) is for the EOI position.

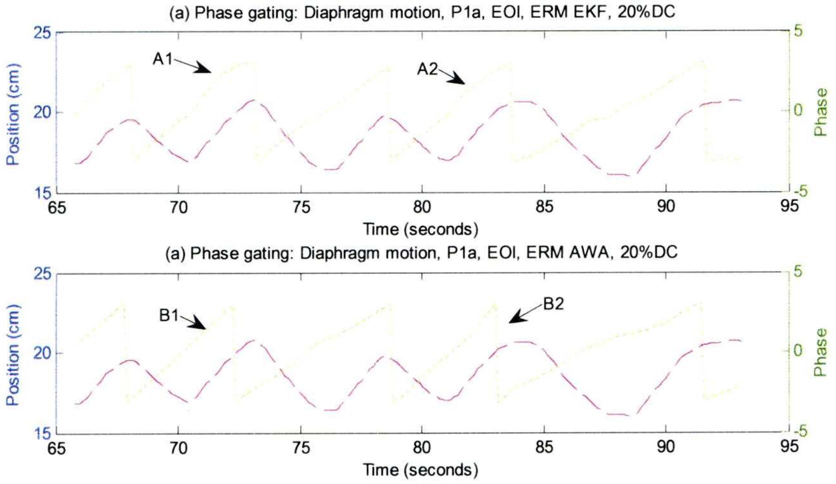

Figure 5-16: The instantaneous phase of dataset-P1a derived by two phase estimation approaches: The yellow dotted curve is the phase and the magenta dashed curve is the breathing signal of ERM. a)EKF approach b) AWA approach. The differences in characteristics of the two approaches are marked with A1, A2 and B1 B2.

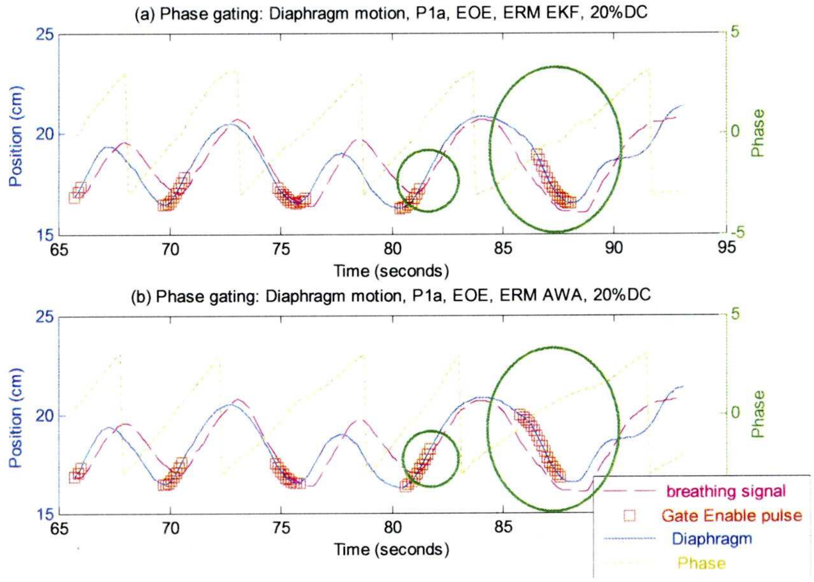

Figure 5-17: The gating pulse dataset-P1a comparing the EKF and AWA approaches: The yellow dotted curve is the phase; the magenta dashed curve is the breathing signal from the ERM. The blue curve is the motion of the diaphragm and the gate enable window is marked with red squares. a) The EKF approach using the ERM signal b) The AWA approach using the ERM signal. The major differences are highlighted by green circles.

Comparing the two phase estimation approaches

Phase gating using the EKF approach achieved 2% to 8% (rRMS) more reduction in residual motion than the AWA approach in different duty cycles and gating positions. When looking into individual datasets, the differences between the two approaches in EOE position were small and not significant. However, one can observe that the EKF gave a better phase representation when the breathing motion was irregular. In the simulation of P1a of Patient-1(arrow A1 of figure5-16), when the signal reached the peak of the previous cycle, the EKF slowed down its phase progression (dθ/dt), but that of the AWA kept increasing (arrow A2). One of the cases for which the AWA performed less well is shown in figure 5-17. Figure 5-17a is from the EKF approach, while Figure 5-17b is from the AWA approach. The red squares are the gating window and the blue curve is the motion of the diaphragm. The magenta curve is the breathing signal from the ERM and the yellow curve is the phase. The major differences are highlighted by green circles. Owing to the accurate phase representation, the EKF approach was capable of determining the gating window with smaller residual motion, for this particular dataset.

Table 5-2: The difference of the residual motions of EKF and AWA approaches. A negative value means the EKF is smaller than the AWA.

rRMS difference of the residual motion of EKF and AWA approaches		
	EOE	**EOI**
20% DC	-2% ± 9%	-3% ± 10%
30%DC	-6% ± 12%	-5% ± 14%
40%DC	-6% ± 10%	-7% ± 5%

The differences between the two approaches in 20%, 30% and 40% duty cycle of the EOI and EOE position are shown in table 5-2. Despite the AWA is worse than the EKF on the average, the differences between the two approaches were not significant.

Phase gating and amplitude gating using the ERM

The rRMS values of amplitude gating (shown in Figure 5-14 and 5-15) were evaluated based on the assumption that the breathing signal was perfectly predicted. Perfect prediction would be achieved by shifting the breathing signal with an amount equal to the systematic delay found in the training dataset. Under such an assumption, on average, there were no obvious differences between the EKF approach and amplitude gating, owing to the large differences among the datasets.

Table 5-3: The difference of the residual motions of Amplitude and phase gating using AWA. A negative value means the rRMS of Amplitude gating is smaller than that of the phase gating.

rRMS difference of the residual motion of :		
(a)amplitude gating and phase gating AWA approaches		
	EOE	**EOI**
20% DC	-2% ± 7%	1% ± 13%
30%DC	-3% ± 7%	-5% ± 12%
40%DC	-6% ± 10%	-7% ± 10%
(a)amplitude gating and phase gating EKF approaches		
20% DC	0% ± 8%	4% ± 12%
30%DC	0% ± 10%	-1% ± 5%
40%DC	-1% ± 6%	0% ± 7%

The differences between the two approaches in 20%, 30% and 40% duty cycle of the EOI and EOE position are shown in table 5-3. Hence, the differences between the two approaches were not significant.

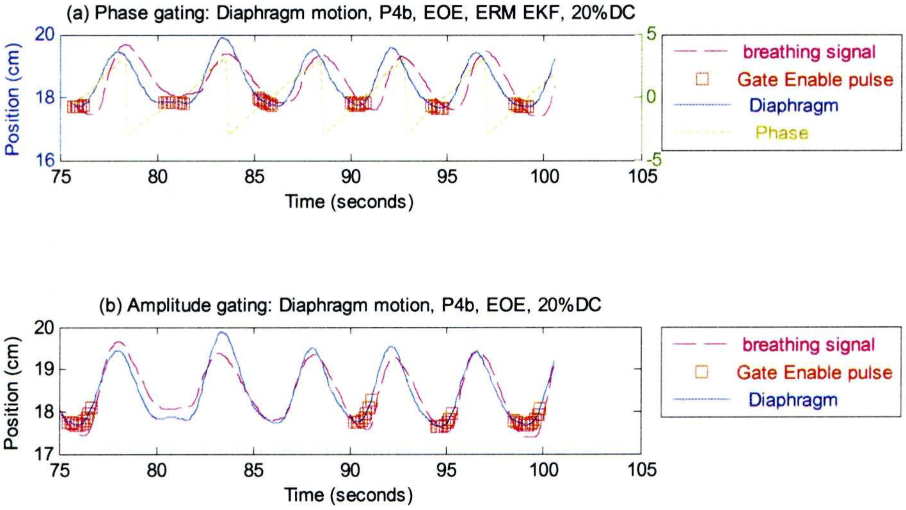

Figure 5-18: The gating pulse of dataset-P4b comparing the EKF phase gating and amplitude gating: The yellow dotted curve is the phase; the magenta dashed curve is the breathing signal from the ERM. The blue curve is the motion of the diaphragm and the gating enabled window is marked with red squares. a) The EKF approach using ERM signal b) amplitude gating using ERM signal. The major differences are highlighted by green circles.

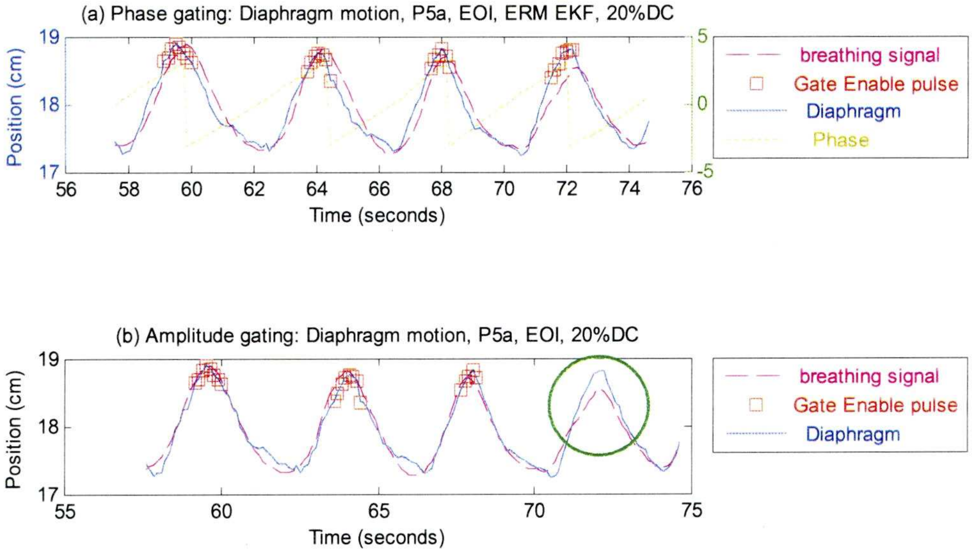

Figure 5-19: The gating pulse of dataset-P5a comparing EKF phase gating and amplitude gating: The yellow dotted curve is the phase, the magenta dashed curve is the breathing signal from the ERM. The blue curve is the motion of the diaphragm and the gating enabled window is marked with red squares. a) The EKF approach using ERM signal b) amplitude gating using ERM signal. The major differences are highlighted by green circles.

In Patient-4 and Patient-5, phase gating achieved smaller residual motion than amplitude gating. In the conditions of regular target motion but irregular breathing signal, phase gating would outperform amplitude gating. A couple of examples from Dataset-P4b (EOE, 20%DC) and Dataset-P5a (EOE, 20%DC) were shown on figure 5-18 and figure 5-19 respectively. In both cases of amplitude gating (figure 5-18b and figure 5-19b), the ERM couldn't represent the amplitude of the target motion accurately. Hence, the gating windows missed a few cycles and increased the residual motion for a duty cycle of 20%. Hence, the phase gating technique is preferable for stable target motions. Despite the variations of EOI and EOE positions, for phase gating to achieve the best performance, good temporal synchronization between the target and the motion is vital.

The selection of gating window in phase gating

The training dataset played an important role in our simulations, because it helped to define the point at which to enable the beam. In the session of EOI gating at 20%DC using the EKF approach on Patient-1 (figure 5-20), the optimum mid-point of the gating window in the training set was 0.85π. Hence, in the evaluation dataset, the gating windows were shifted to the left of the peaks. Because of this, the gating windows were not aligned with every peak of the breathing signal. If the gating windows had been aligned with the peaks, the large variation of the peaks would have significantly increased the residual motion.

If the systematic delay between the training dataset and treatment dataset was largely different, the residual motion of the target would be affected by a large amount. Therefore, in phase gating, the systematic delay between the motion signal and the breathing signal should be accurately estimated.

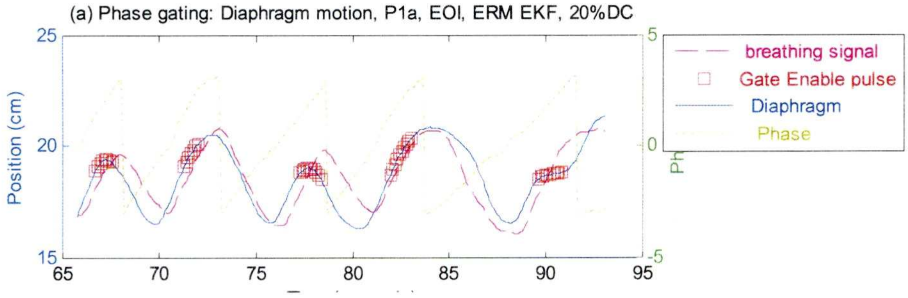

Figure 5-20: The gating pulse of dataset-P1a EKF approach phase gating using ERM signal. The yellow dotted curve is the phase; the magenta dashed curve is the breathing signal from the ERM. The blue curve is the motion of the diaphragm and the gate enable window is marked with red squares..

5.6. Conclusion:

Two approaches to estimating the instantaneous phase of a breathing signal have been assessed: The EKF approach and the AWA approach. The EKF approach utilizes an Average Trajectory Function to model the parameters of breathing and follows by using EKF to estimate the parameters. On the other hand, the AWA approach utilizes autocorrelation windowing and DFT. The EKF approach was found to be more reliable in reducing residual motion of the target in the phase gating simulation of 12 datasets from 5 patients. Despite the relatively slightly worse performance, the AWA approach is simpler to implement.

The relative performance of phase gating over amplitude gating was evaluated. If the systematic system delay between the breathing signal and the target motion is perfectly compensated in amplitude gating, phase gating would contribute to a significant performance gain in some of the datasets. This was because the ERM does not accurately indicate the amplitude of breathing. However, the performance gain is highly dependent on the synchronization between the target motion and the ERM signal. Irregular amplitude of target motion occurred together with lack of synchronization on the same patient. Further investigation is needed to assess whether the association between the two conditions is common among a wider group of patients.

In the simulation, the systematic delay (mentioned above) could affect the performance of phase gating by a large amount, because it determines the timing to enable the radiation beam. Prior to starting a treatment by phase gating, it is important to ensure that the delay is not significantly different from that in the training dataset.

6. Prediction Algorithms

6.1. Introduction

In order to reduce the residual motion of the target using gated radiotherapy, it is necessary to enable the radiation beam at the correct time to ensure that the target is in the radiation field. This is achieved by monitoring the patient's breathing pattern and relating this to the tumour position. The existence of a time delay between the breathing signal and the positioning of the tumour in the radiation beam implies that some kind of predictive ability should be included in a gating treatment system. The delay, if neglected, results in loss of accuracy in hitting the target. Consequently, it results in under-dosing to some parts of the target volume (Vedam *et al* 2005). Hence, the internal margin has to increase for acceptable dose coverage. A typical human breathing cycle, being largely periodic, has significant cycle-to-cycle fluctuations in displacement, as well as longer-term fluctuations in both displacement and frequency. However, these fluctuations are not purely random, suggesting there are possibilities to predict a particular breathing cycle from the observed characteristics of previous breathing cycles. In Chapter 4, we showed that delay compensation could have significant benefit on residual motion reduction. In this chapter, the impact of prediction algorithms is investigated.

Detection and imaging delay:

In the evaluation of residual motion of the patients of Chapter-4, the systematic delay of the ERM and the target motion can be as large as 0.4 seconds. There was significant performance improvement if the breathing signal was perfectly compensated for the detection delay. Hoisak *et al* (2004) assessed the correlation of respiratory volume and abdominal displacement with tumour motion using X-ray fluoroscopy. A maximum phase lag of 0.35s was found in the respiratory volume signal and a maximum phase lag of 0.65s was found in the abdominal displacement signal. Tsunashima *et al.* (2004) found that although the delays between the respiratory waveform and the 3D tumour motion were principally in the range 0.0 to 0.3 s, there existed cases of nearly 1.0s and above.

Sharp *et al* (2004) described the existence of system latency and its effect on tumour location accuracy. In real-time image-guided delivery systems, consisting of a LINAC, imaging device and information system, there is always a system latency due to the time needed for image processing, response times of hardware, and communication delays. This means that the real-time tracking or gating directly from the location of the sampling image is based on estimations of some past time. Keall *et al* (2004) have investigated whether a position signal obtained by an Electronic Portal Imaging Device (EPID) measurement of an internal marker could be used to control a dynamic MLC delivery of IMRT. The EPID was set to acquire an image in 0.1 s, as opposed to the normal setting of 1 s; however, the interval between acquisitions was still 1 s. The long interval between image acquisitions and processing prohibited the clinical application of EPID in real-time tracking. However, they considered that it would be feasible if predictive tracking could be implemented.

Control-System Delays:

The response of a beam control system to a breathing signal cannot occur instantaneously. Seppenwoolde *et al* (2002) report a delay of 90 ms between the recognition of a fiducial marker in a fluoroscopic image and the triggering of irradiation in their gated beam-delivery system. Mechanical systems which need the beam to be repositioned have longer delays. The CyberKnife[9] has a 200 ms delay between acquisition of tumour coordinates and repositioning of the linear accelerator. Repositioning an MLC aperture will likewise involve a time delay of 100–200 ms or more (Keall *et al* 2006). Shirato *et al* (2000) reported a time delay of 0.09 s between the time of the marker recognition and the start of irradiation in a gating system. Measurement results of Jin and Yin (2005) for a similar gating system show that the time lag including the response time of the LINAC and the delivery time is 0.17±0.03 s. In the robotic radiation delivery system studied by Schweikard *et al* (2000), the time lag including the response time of the robot was of the order of 0.3 s.

---

[9] Accuray, Sunnyvale, CA

6.2. Review of breathing signal prediction algorithms:

Shirato *et al* (2000) implemented a linear extrapolation method which was able to predict the tumour position about 0.09 s in advance. With implanted golden markers and with the assumption of constant linear marker speed, they claimed to achieve prediction errors less than 1.5 mm. Murphy *et al* (2002) analyzed breathing prediction using a variety of adaptive filters and found that the tumour position can be predicted with up to 80% accuracy in the presence of a 200 ms system delay, but accuracy degrades rapidly with longer delay intervals (1 second prediction horizon). Sharp *et al* (2004) investigated the performance of a linear filter, neural networks (NN) and a Kalman filter, to characterize the predictability of lung tumour motion for different imaging rates and system latencies. The best predictor, Linear filter, achieved and RMS error(RMSE) less than 2mm for prediction time 0.2 s with a 10Hz sampling rate (compared to 3mm RMSE when prediction is not used).

Vedam *et al* (2004b) compared the prediction performance of an adaptive sinusoidal filter and an adaptive linear filter. In the sinusoidal filter, the current data point was compensated by a value with reference to a sinusoidal model. In the adaptive linear filter, an LMS algorithm was used to update the weight vector. The adaptive linear filter performed better and achieved prediction errors of 2 mm (RMSE) for prediction time of 0.6 s with a 10 Hz sampling rate. The average root mean square of the motion extent was about 3.6mm.

Ernst *et al* (2008) modified the least mean squares (LMS) based adaptive linear prediction algorithms so as to allow for dynamic adaptation of both learning rate and signal history length to cope with possible changes in the breathing motion signal's characteristics. This was done by parallel evaluation of several LMS predictors initialised with different values of learning rate and signal history length.

In addition to Sharp *et al* (2004), Isaksson *et al* (2005) proposed an Adaptive Neural Network (ANN) and showed that its prediction performance was better than that of a linear filter using LMS prediction in terms of the normalized RMSE (nRMSE). They studied the breathing traces from three patients. In the case of regular breathing and a 500ms prediction horizon, the nRMSE of ANN was about 50%. In the case of irregular breathing and the same prediction horizon, the nRMSE of ANN was 62%. In both conditions, the nRMSE of an adaptive linear filter was 2% better than ANN. The differences between the two algorithms were small, given that the total range of motion of the patients was not large. Kakar *et al* (2005) used an Adaptive Fuzzy Neural Inference System

(ANFIS), which is an augmented Gaussian radial basis function NN. ANFIS combines both the learning capabilities of a neural network and reasoning capabilities of fuzzy logic in order to give enhanced prediction capabilities. Previous studies have shown that ANFIS is a better predictor for a chaotic time series as compared to using a single technique like an artificial neural network alone (Jang *et al*1995).

Putra *et al (*2008) proposed a multiple model approach to respiratory-induced tumour motion prediction using the interacting multiple model (IMM) filter algorithm and to compare its performance to a single model Kalman filter. The IMM, based on a stochastic discrete time linear system, modelled the constant velocity (CV) and constant acceleration (CA) properties of the breathing signal. During steady inhale and exhale phases, respiratory motion is almost at a constant velocity. At the transition between inhale and exhale, respiratory motion is decelerated at the end of inhale/exhale and is accelerated at the beginning of exhale/inhale. A single CV model or single CA model may not be adequate to capture the dynamics of respiratory motion. The breathing signals of 110 traces from 24 lung-cancer patients in George *et al*2005 were used to evaluate the prediction performance of the IMM and Kalman filters. The respiratory motion traces were acquired using the RPM system of Varian Medical Systems. With 30Hz sampling frequency, the IMM, CV and CA filter showed 19% to 49% reduction in root mean square error (RMSE). However, the difference between the CV model and the IMM was small: with a maximum of 0.04 mm RMSE difference. We can expect that, if the IMM algorithm were used for predicting the ERM signal (instead of the CV only model), the performance gain would be very small. Since the ERM signal is a surrogate which has lower correlation with the tumour (comparing with the Varian RPM used in the study of George *et al*), the extra complexity of the IMM algorithm would not bring significant benefit to the RMSE reduction.

6.3. Methodology

Since most of the above studies either (a) measured the prediction error in a absolute value or (b)used abdominal motion for breathing monitoring, the effect of them on the ERM signal is not known. Therefore, in this study, we evaluated the performance of a collection of prediction algorithms:

> (1)Adaptive linear prediction using Normalized Least Mean Square NLMS for weight update and (2)Neural Network, because they were both widely implemented in the literature;
>
> (3)ANFIS, because it is a newly proposed algorithm for respiratory signal prediction;
>
> (4)Extended Kalman Filter-Average Trajectory Function (EKF-ATF), because the built in phase estimator proposed in Chapter-5 can be used for prediction. Moreover, the performance of average trajectory model based prediction of the breathing signal has not been evaluated in the literature.

We used the breathing signals from the ERM from 9 free breathing datasets of volunteers from Chapter 3. The first 40% of samples of each signal were used as the training dataset. The maximum breathing signal latency from the ERM was 480ms (Chapter 4) and the beam delivery latency was assumed to be about 100ms. The first aim was to find the algorithm with the smallest nRMSE for 500ms to 600ms prediction horizons. The second aim was to investigate the impact of prediction algorithms on residual motion reduction. As a follow up to chapter-4, the amplitude gating simulation was used to assess the residual motion of the target using the output of the prediction algorithms. The prediction algorithm must compensate for the delay of the ERM signal (with respect to the target motion) together with any control system delays.

Adaptive linear prediction using NLMS

A linear predictor is a system which predicts the future output signal as a linear function of a set of inputs (Sharp *et al* 2004). We consider linear predictors of the form:

$$y_t = w_t \cdot u_t \tag{6.1}$$

where y_t is the predicted signal at step t, w_t is the corresponding weight vector (with length M)and u_t is the signal history ("tap input vector" with length M) used in step tto compute y_t

In each step t, the weigh vector is updated,

$$w_t = w_{t-1} + \frac{\mu\,(z_t - y_t) \cdot u_t}{u_t \cdot u_t} \tag{6.2}$$

where μ is the learning rate parameter and z_t is the measured signal at step t.

The optimum value of μ and M are determined from the training dataset. The range of μ and M were [0.1, 2.0] and [5, 50] respectively. The initial weight vector w_0 was computed from the final value of the weight vector when the optimum values of μ and M were applied to the training set.

Artificial Neural Network

The Feed-forward artificial neural network was used for prediction. It has one-way connections from input to output layers. They are most commonly used for prediction, pattern recognition, and nonlinear function fitting. The future velocity of the breathing signal was predicted, instead of the future position. This was because from both our early trial and the experimental result of Sharp *et al* 2004, velocity prediction yielded more accurate prediction results. In the first trial using the 9 healthy volunteer dataset, the optimum prediction accuracy was obtained with a hidden layerof12 neurons and "tap input vector" with length 16. The weights of the ANN were estimated from the training dataset. The Neural Network training Tools of Matlab 2007b was used as the Neural Network library.

The training parameters are listed as follow:

- Training algorithm: Levenberg Marquardt
- Data Division: Random
- Checking data: 30% (of the training dataset)
- Max. Epochs: 500
- Time: Inf
- goal: 0
- mem_reduc: 1
- min_grad: $1e^{-10}$
- mu: $1e^{-3}$
- mu_dec: 0.1
- mu_inc: 10
- mu_max: $1\ e^{10}$

Adaptive Neuro Fuzzy Inference System:

The combination of the ability of a neural network (NN) to learn with fuzzy logic to reason in order to form a hybrid intelligent system is called ANFIS (adaptive neuro fuzzy inference system). The goal of ANFIS is to find a model or mapping that will correctly associate the inputs (initial values) with the target (predicted values). The fuzzy inference system (FIS) is a knowledge representation where each fuzzy rule describes a local behaviour of the system. An ANFIS network structure is similar to that of a neural network. It maps inputs through input membership functions and associated parameters, and then through output membership functions and associated parameters to outputs. Kakar *et al* 2005 and Jang *et al* 1995 gave detailed introductions to the ANFIS. With reference to the input data points dimension in Kakar *et al* 2005, the data points in each row were set to 1 steps apart and each epoch contained 8 data points. The FIS and the initial weight of the NN were estimated from the training dataset. ANFIS was trained with the help of Matlab 2007b with the following parameters.

ANFIS Parameter Values

- MF type: Bell function
- Number of MFs:8
- Output MF: Linear
- Number of Nodes:155
- Number of linear parameters:128
- Number of nonlinear parameters: 24
- Total number of parameters:200
- Number of fuzzy rules:8

EKF-ATF

The implementation of EKF-ATF is the same as the phase estimator in Chapter 5.3. Let us assume that y is the predicted value, that t is the current position in time and that δ is the prediction horizon. Furthermore, let x be the state vector. The future state becomes:

$$x_{t+\delta} = (F_x)^{\delta} x_t \tag{6.3}$$

where F_x is the Jacobian of the state transition function (equation 5.3.11)

Hence, from equation 5.3.8, the prediction y becomes:

$$y = h(x_{t+\delta}) \tag{6.4}$$

where *h(.)* is the measurement function.

6.4. Results and discussion:

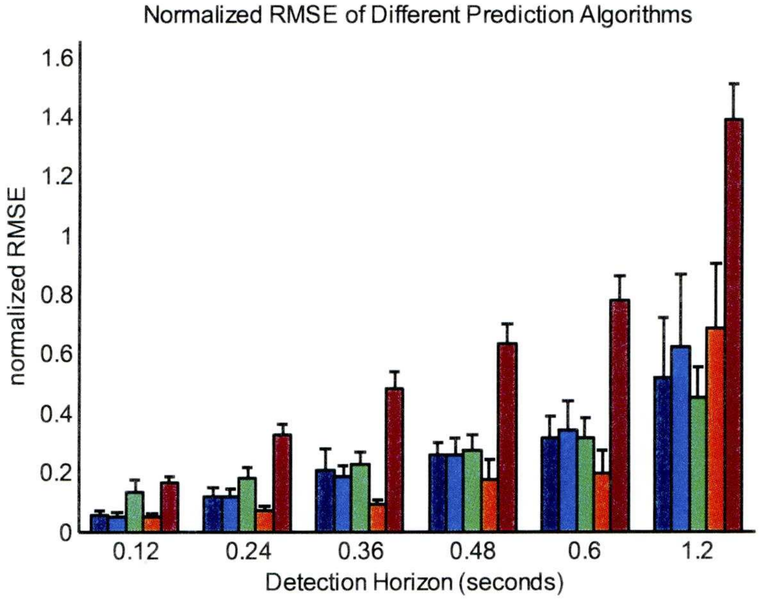

[Legend: **ANN** **ANFIS** **EKF** **NLMS** **No Prediction**]

Figure 6-1: The nRMSE of different prediction algorithms averaged over all the datasets using ERM signals. The length of the error bar indicates one standard deviation. The results are grouped by different detection horizons.

The nRMSE values of different prediction algorithms averaged over all the datasets were plotted on figure 6-1. The LMS algorithm was the best performing predictor for a wide range of prediction horizons (which is consistent with the findings of Sharp *et al.*2004 and Vedam *et al.*2004). The nRMS of the ANFIS were not significantly different from the ANN algorithm. Hence, the extra computational power spent on the FIS did not show significant impact. One of the possible reasons was that the datasets were not irregular enough, such that the "adaptive" property of the ANFIS was not obvious. The EKF algorithm has the lowest average nRMS when the prediction horizon is at 1.2 seconds; however, the advantage was not significant. Except the EKF based algorithm in the 0.12s prediction horizon, the normalized RMSE of all the algorithms were lower than having no prediction.

As a control experiment, the prediction algorithms tried to predict a sinusoidal wave with prediction horizon ranges from 0.12s to 1.2s. Nearly all algorithms have extremely small prediction error.

nRMSE of a sinusoidal signal				
Prediction horizon (s)	**ANN**	**ANFIS**	**EKF**	**LMS**
0.12	0.00	0.00	0.00	0.00
0.24	0.00	0.00	0.00	0.00
0.36	0.00	0.00	0.00	0.00
0.48	0.04	0.06	0.08	0.10
0.60	0.04	0.09	0.15	0.34
1.2	0.20	0.39	0.58	0.77

Table 6-1: The nRMSE of a sinusoidal wave using different prediction algorithms.

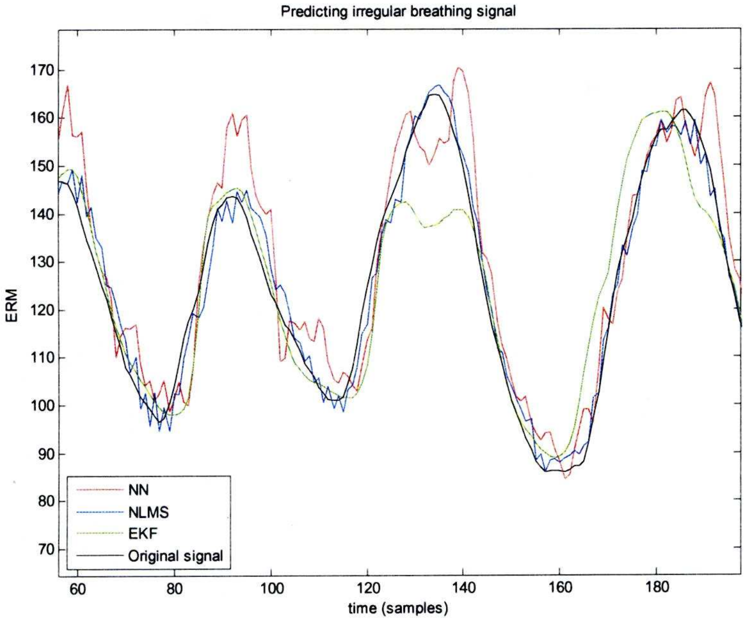

Figure 6-2: Prediction of irregular signals at 480ms prediction horizon.

The NLMS performed well in predicting irregular signals. An example is shown in Figure 6-2. Over-shoot occurred at the first two peaks (at the 60th and 90th samples) of the Neural Network prediction. The EKF could adapt to the gradual decrease of instantaneous amplitude from the 60th to 120th sample. However, after the 120th sample, the breathing amplitude increased by a large amount, the EKF could track the change of amplitude starting at the 140th sample.

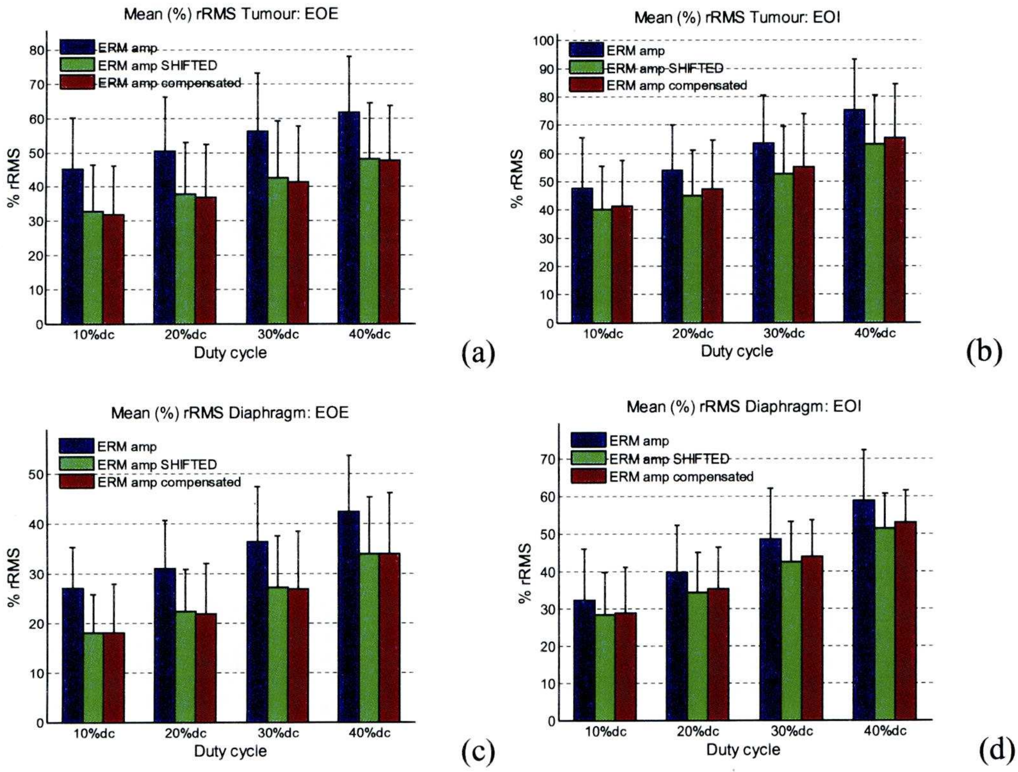

Figure 6-3: The blue bars are the mean rRMS (in percentage) organ residual motions over 12 datasets using amplitude gating without any delay compensation, while the red bars are delay compensated by LMS prediction. The green bars were produced by shifting the breathing signal to compensate for the delay. (a)Tumour EOE, (b)Tumour EOI, (c)Diaphragm EOE and (d)diaphragm EOI.

The systematic delay between the signal of the ERM and the tumour motion ranged from 1 to 4 time steps (0.12s-0.48s). Based on the above results, the best predictor was the NLMS because, on average, it produced the best result from 2 to 5 time steps. Although, the nRMSE of EKF was the lowest at 1.2s prediction horizon, the different (of nRMSE) between EKF and the NLMS algorithms was not significant (mean difference 0.23±0.29). Hence, the NLMS was used as predictor for compensating the delays. The results, measured by % rRMS of the patients in Chapter 4, with 120ms systematic control delay, are shown on figure 6-3. When predictive gating was applied with amplitude gating, there could be a further reduction in the residual motion of about 10% (EOE) and 5-10% (EOI). If we look at the error of the no prediction bars on figure 6-1, the error was approaching unity when the prediction horizon was beyond 600ms. Under such condition, the residual motion reduced by gating would be neutralized by the decrease in accuracy of target position estimations. The comparisons of the rRMS of the 12 datasets in 30% duty cycle are shown in figure 6-4. The difference of rRMS between no-prediction and the NLMS compensation was 18%±16% in the EOE and 12%±9%. Most of the datasets benefit from the prediction algorithm to compensate for the systematic delays. In Dataset P1a and P3a, the residual motion of the tumour was increased by 2% and 1% in the IS direction. With prediction, 9 out of 12 datasets have more than 10% (rRMS) reduction in the EOE; while 7 out of 12 have more than 10% (rRMS) reduction in the EOI.

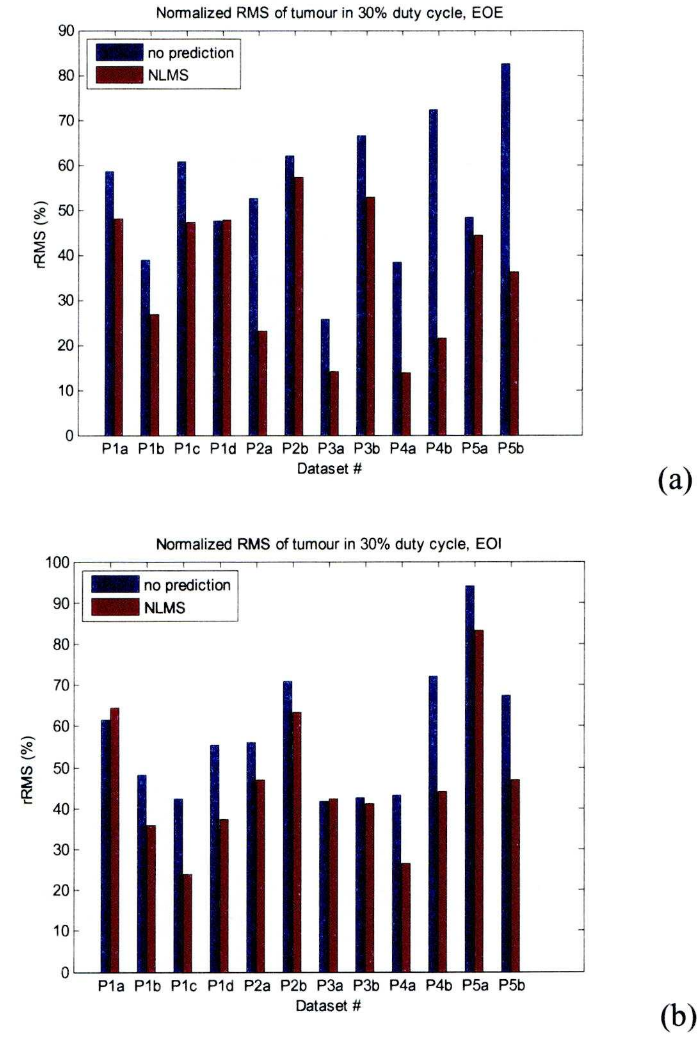

Figure 6-4: Comparison of the rRMS of NLMS prediction and no prediction in 30% duty cycle of the tumour IS motion. The blue bars are the mean rRMS organ residual motions over 12 datasets using amplitude gating without any delay compensation, while the red bars are delay compensated by NLMS prediction. (a)EOE, (b)EOI.

6.5. Conclusion:

It is concluded that prediction algorithms are essential for amplitude gating. The adaptive linear algorithm (NLMS) can effective predicts the ERM signal for a wide range of prediction horizons. If systematic delay is ignored in gating, the error introduced could easily neutralize the effect of gating.

7. Applications Developed for the ERM

7.1. A Software tool to evaluate the regularity of breathing

7.1.1. Introduction

When audio coaching techniques are used in radiotherapy, one needs to choose the repeat rate of the audio prompt. Normally the rate of audio prompt is set to the same as the natural breathing rate. From the healthy volunteer experiment of Chapter-3, most of the volunteers felt uncomfortable with the audio prompt at the rate of natural breathing. Hence, the patient is required to perform a number of trials with different coaching parameters. The Varian RPM system installed at the Clatterbridge Centre for Oncology displays the amplitude of breathing. Ideally the repetition rate would be chosen to minimise the amplitude of breathing. However, amplitude is not the only relevant factor in the evaluation of the breathing signal. One of the aims of coaching is to improve the regularity of the breathing. We can reasonably expect that if a patient is breathing rhythmically, the tumour and external motions will be more in phase as compared to breathing irregularly. We developed a methodology to evaluate the regularity of the breathing signal. This methodology was incorporated into a program which facilitated the comparison of different breathing samples so that a clinical decision could be more easily made as to which method of coaching should be used. Since the Experimental Respiratory Monitor (ERM) is highly portable, the patient can complete the respiration regularity test in a normal room, so that the couch would be free for other clinical usage. An instant feedback of the regularity of the breathing signal is provided when a new set of gating parameters is applied. This software supports displaying the parameters for maximum of four sets of breathing signals, so that the clinician can choose the parameters (or settings) which best suit the patient.

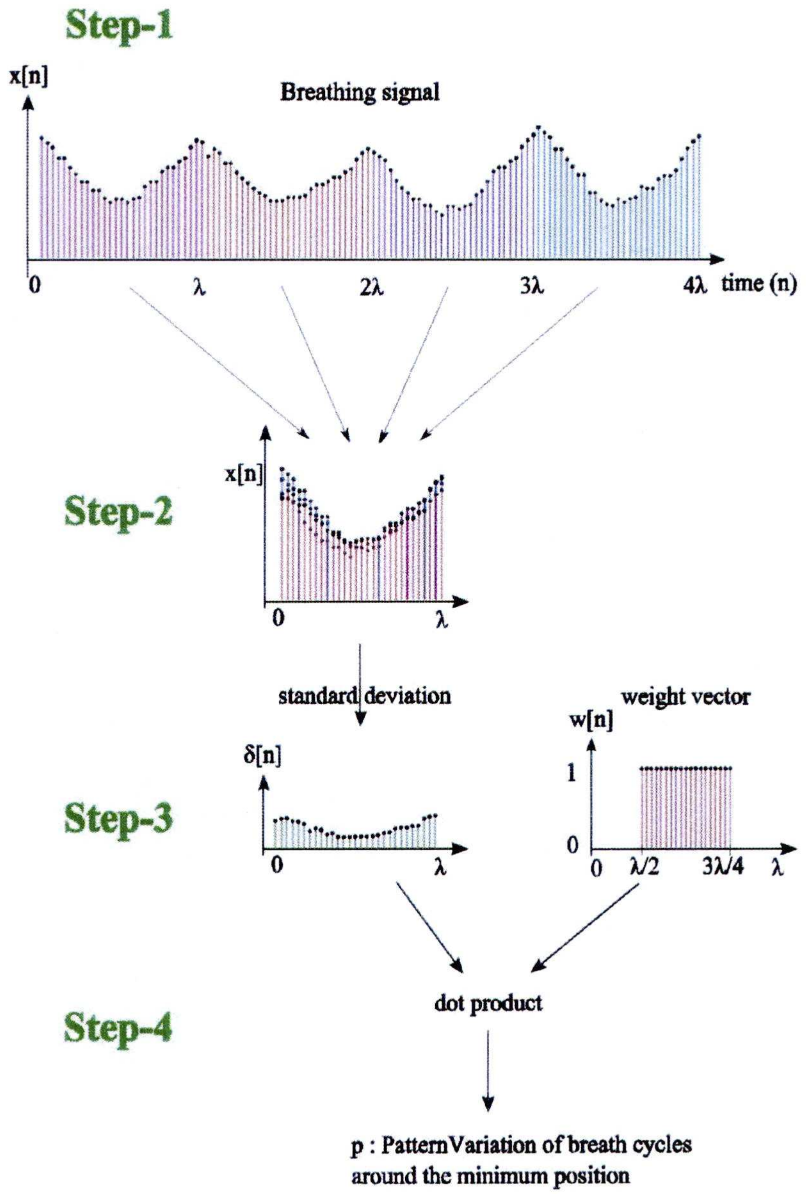

Figure 7-1: Schematic diagram of evaluating the variation of breathing cycles: A breathing signal containing several breathing cycles is divided into segments of equal length. The length is equal to the mean duration of the wave cycles. The standard deviation vector δ[n] of the aligned wave form is computed. The variation of the wave pattern weighted at the local minimum position is defined as the dot product of a weight vector w[n] and the standard deviation vector δ[n]. w[n] is a vector with a square pulse distribution of values.

7.1.2. Methodology

7.1.2.1. The model for finding the pattern variation of breathing cycles

For measuring regularity, we produce a wave model from the breathing signal.

The breathing signal of a person is cyclic over a long period of time. It is smooth if the person breathes naturally. It slightly varies up and down if the person does nothing abnormal (coughing, talking etc). If a feature point can be found in each cycle, we can separate the signal by the feature point. A long breathing signal is divided into individual wave segments by dividing them at their peak, such that the segments can be evaluated. The wave segments would then align according to their minimum point (Figure 7-1).

The alignment begins with identifying the local maxima and minima of a breathing signal. A point is considered a maximum if it has the maximal value, and was preceded (to the left) by a value lower by T_a. The default value of T_a is the RMS amplitude of the whole signal x_F. The parameter T_a adjusts the sensitivity of the peak detection. A high T_a value would decrease the sensitivity of the peak detection algorithm, making it suitable for noisy signals. After a maximum has been found, the algorithm would search for a trough and iterates until the end of the signal.

Hence, the local maxima M_a and minima M_b would be located from the breathing signal x_F. $M_a[k]$ is a vector, with length A, containing the index of the local maxima; $M_b[k]$ is a vector, with length B, containing the index of the local minima.

For finding the variations of breathing pattern about its minimum positions, the mean of the breathing period λ_b is calculated by finding the mean of the difference $\Delta M_a[n]$ of vector $M_a[n]$.

A set of equal length vectors x_k, each represent a segment of the k^{th} breath cycle (Step-2 of Figure 7-1). The length of x_k is 2·round(λ_b/2) +1. x_k is defined by:

$$x_k[n] = x_F\left[M_a[k] - \frac{g}{2} + n\right], \quad for\ 1 \leq n \leq 2g + 1$$

$$g = \text{round}\left(\frac{\lambda_b}{2}\right) \tag{7.2}$$

For each value of n in the set of x_k, the standard deviation vector $\delta[n]$ is computed (Step 3 of Figure 7-1). It is defined by:

$$\delta[n] = \sqrt{\sum_{k=1}^{A} \frac{(x_k[n] - \overline{x_k}[n])^2}{A}}$$

$$\overline{x_k}[n] = \sum_{k=1}^{A} \frac{x_k[n]}{A} \tag{7.3}$$

The variation p of the breathing pattern about its minimum positions (Step-4 of Figure 7-1) is defined by the dot product between the standard deviation vector $\delta[n]$ and a weight vector $w[n]$. $w[n]$ is a vector with unit values spaced equally around half the wavelength (period).

The aim of weighting is to focus on estimating the variations on the EOI or the EOE position. $w[n]$ is defined by:

$$w[n] = \begin{cases} 0, & for\ 1 \le n \le B_1 - 1 \\ 1, & for\ B_1 \le n \le B_2 \\ 0, & for\ B_2 + 1 \le n \le 2g + 1 \end{cases}$$

$$B_1 = round\left(\frac{g}{2}\right), \tag{7.4}$$

$$B_2 = round\left(\frac{3g}{2}\right),$$

where *round(.)* is the decimal round off function and $g = round(\lambda_b/2)$

Hence, the variation p is normalized by the sum of the weight vector $w[n]$ and the RMS of the amplitude of the breathing signal. It is given by:

$$p = \frac{\delta[n] \cdot w[n]}{(B_2 - B_1 + 1) \cdot std(x_F)}$$

where x_F is the breathing signal and *std(.)* is the standard deviation function

The variation p increases as the baseline drift increases, but p has no effect in changing frequency.

For finding the variations of the breathing pattern about its maximum positions, we replace $M_b[n]$ with $M_a[n]$ and $g = round(\lambda_b/2)$ with $g = round(\lambda_a/2)$ in Equation 7.2; and replace A with B in Equation 7.3. The mean of the breathing period λ_a is calculated by finding the mean of the difference $\Delta M_a[n]$ of vector $M_a[n]$.

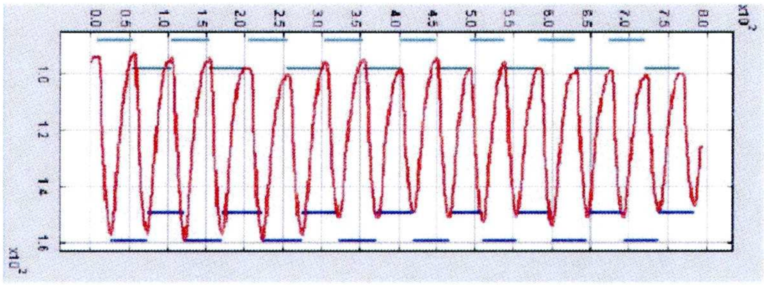

Figure 7-2: Result of breathing cycle segmentation of the program. The breathing signal (red trace) is plotted above. The y-axis is the amplitude and the x-axis is the time in unit samples. The result of the segmentation is displayed as horizontal line segments. The line segments (cyan colour) on top of the breathing signal represent the breathing cycles segmented with reference to the minimum positions; while the line segments (blue colour) below the breathing signal represent the breathing cycles segmented with reference to the maximum positions.

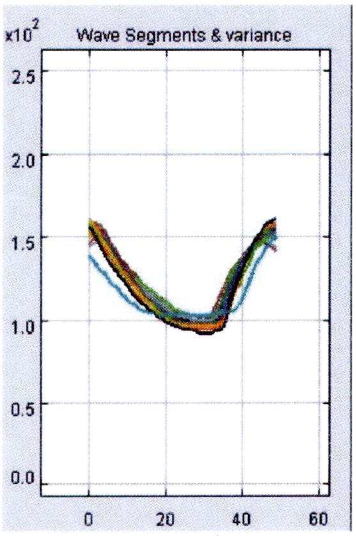

Figure 7-3: Wave segments aligned to the local minima. The screen capture of the wave segment window shows the variation of the breathing cycles and provides an alternative to the numerical presentation. The y-axis is the amplitude of the breathing signal. The x-axis represents the time measured in unit samples.

7.1.2.2. The Variation of extreme positions

The variations of amplitude of the maximum or minimum positions are defined as the standard deviation of their amplitude. The standard deviation of maximum positions δ_A is defined by:

$$\delta_{\mathrm{A}} = \mathrm{std}(x[M_a[k]]) \quad ,\forall k$$

where *std(.)* is the standard deviation function, *x[.]* is the original breathing signal and $M_a[k]$ is the vector of maximum position pointers.

The standard deviation of maximum positions δ_B is defined by:

$$\delta_{\mathrm{B}} = \mathrm{std}(x[M_b[k]]) \quad ,\forall k$$

where *std(.)* is the standard deviation function, *x*[.] is the original breathing signal and $M_a[k]$ is the vector of minimum position pointers.

7.1.2.3. The Variations of Breathing Period

For finding the variations of the breathing pattern about its minimum positions, the standard deviation of the segment duration vector $\Delta M_b[n]$ is calculated. It is defined as the difference of the maximum position vector $M_b[n]$; ie: $\Delta M_b[n]=M_b[n]-M_b[n-1]$.$M_b[n]$ is a B-dimensions vector containing the index pointing to the maximum positions in the breathing signal $x[n]$.

The elements of the segment duration vector $\Delta M_b[n]$ are plotted on a chart in the software, so that the change of breathing period over time can be visualized.

7.1.3. Specifications:

A program written in Java was developed to evaluate the variations of the breathing signal of the ERM based on the above methodology. The specifications of the program are listed as follow:

- To evaluate a maximum of 4 sets of breathing signals simultaneously. In most of the situations, a clinician only needs to compare 3 sets of breathing signals; two for the best-parameter sets and one for testing new parameters. The ability to compare four signals was to allow flexibility.
- Customizable peak detection parameter T_a to account for the noise of the breathing signal for accurate breathing cycle segmentation.
- Aligning the wave cycles with their maximum points at the centre; display the aligned breath cycles in different colours.
- Aligning the wave cycles with their minimum points at the centre; display the aligned breath cycles in different colours.
- Provide measurements for the following quantities:
    - Standard deviation of the (local) maximum positions
    - Standard deviation of the (local) minimum positions
    - The variations of the breathing period over time
    - Standard deviation of the breathing periods
    - The sum of weighted standard deviation of the breath cycles aligned by the minimum points at the centre
    - The sum of weighted standard deviation of the breath cycles aligned by the maximum points at the centre

7.1.4. The user Interface:

The user interface elements are divided into 4 columns (figure7-4). The number of columns is limited by the size of the User Interface elements and the resolution of the display. The program was designed for displaying on a 1280-x1024 screen. Each of the columns corresponds to one set of breathing signals. The fourth column also contains two more elements. One of them is the signal monitor tab, which can monitor the result of segmentation of the breathing cycles (Figure 7-5). The other element is a plot of segmented breath cycles centred at the maximum position (Figure 7-6).

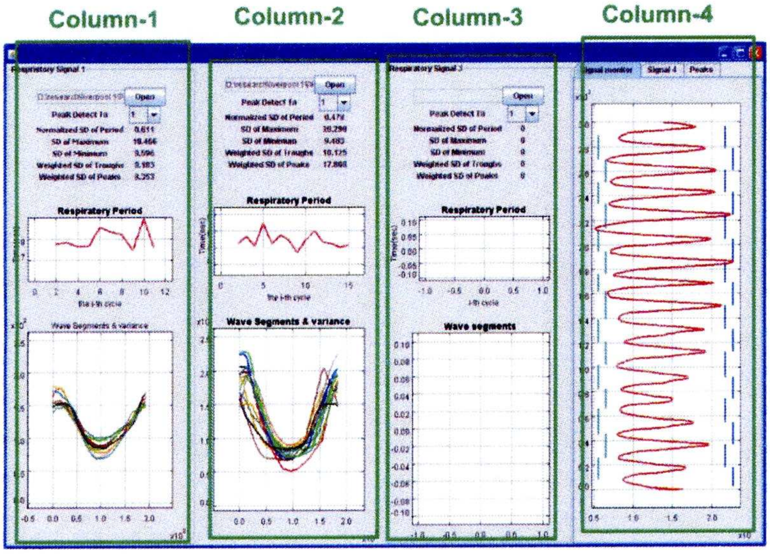

Figure 7-4: A snapshot of the 4 column layout of the software

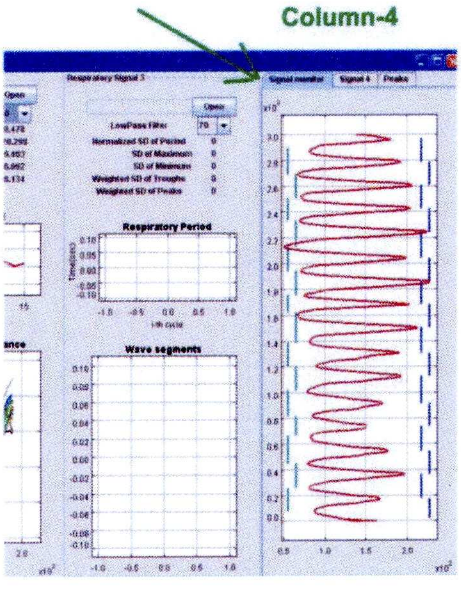

Figure 7-5: The signal Monitor displaying the segmentation result

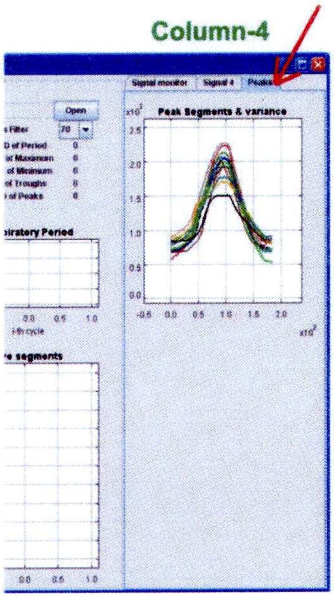

Figure 7-6: A tab in the 4th column showing the aligned breath cycles about their maximum position.

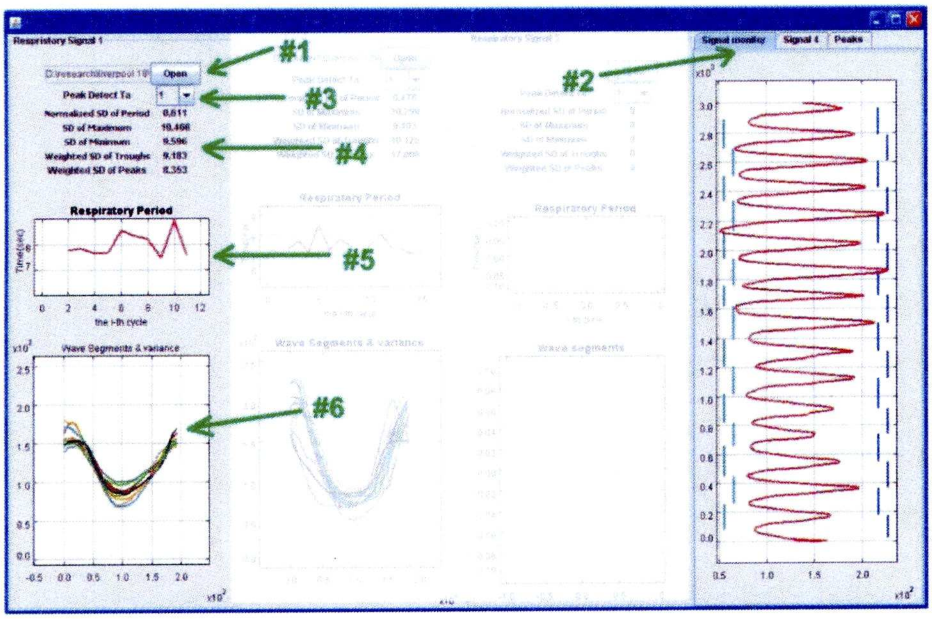

Peak Detect Ta 1

Normalized SD of Period 0.611

SD of Maximum 10.468

SD of Minimum 9.596

Weighted SD of Troughs 9.183

Weighted SD of Peaks 8.353

Figure 7-7: User Interface of the Breathing Signal comparison tools: The tools allow clinicians to evaluate the regularity of the 4 different breathing signals at once. By providing the variation of the motion and regularity measurements, it helps clinicians to find the best set of parameters for gating. Please refer to section 7.1.5 for descriptions of the interface.

7.1.5. User-Program Interaction Procedure:

After the program started up, the user loads (#1of Figure 7-7) the breathing signal into one of the 4 panels.

Once the signal is loaded into the program, the program automatically divides the signal into segments. The result of the segmentation is shown in the Signal Monitor Tab in the fourth column (#2 of Figure 7-7).

The default value of the peak detection parameter T_a is 1.0 multiplied by the RMS of the breathing signal. If the user is not satisfied with the segmentation result (eg: the program might have classified a short-time fluctuation as a complete breath cycle), the user can select different values of T_a (#3 of Figure 7-7). The range is from 0.1 to 2.0 times the RMS value of the breathing signal with a step size of 0.2. The program would perform the segmentation again whenever a new peak detection parameter is selected.

The following measurements of the variations are displayed (#4 of Figure 7-7):

- the standard deviation of breathing period (in the unit of seconds),
- the standard deviation of the maximum,
- the standard deviation of the minimum,
- the variations of the breathing pattern about the troughs (minimum position) as describe in chapter 7.1.2.1, and
- the variations of the breathing pattern about the peaks (maximum position) as described in chapter 7.1.2.1.

The variation of the breathing period over time is plotted on the chart at #5 of Figure 7-7.

The aligned breath cycles about their troughs are plotted in the bottom chart of the column (#7 of Figure 7-7).

The aligned breath cycles about their peaks are plotted in the Peak Tabs of the 4th column (Figure 7-4).

The second and subsequent breathing signals can be evaluated in the 2nd, 3rd and 4th column (Figure 7-4).

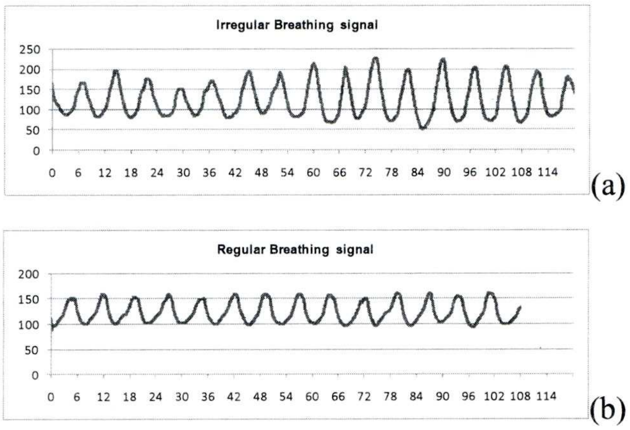

Figure 7-8: Breathing signal of the volunteer of (a)Irregular and (b)Regular breathing patterns were used as input to show the function of the software.

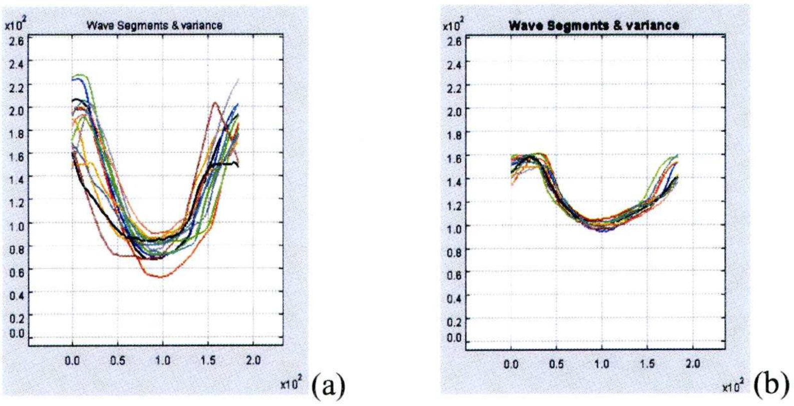

Figure 7-9: Wave segments aligned to the trough of (a) an irregular breathing signal and (b) a regular breathing signal

7.1.6. Evaluation of the Software

An irregular and a regular breathing signal of a healthy volunteer was used as an example to evaluate the program. The regular signal was obtained after the patient had been coached. The irregular signal prior to coaching is plotted in Figure 7-8a. The regular signal after coaching is plotted in Figure 7-8b. The segments of the breathing cycles were aligned about their troughs and are plotted in Figure 7-9. The list of measurements is shown in Table 7-1.

From the data, we can determine that the SD of the breathing period of the subject was reduced in regular breathing as well as the variations in the extreme positions. The clinician can then decide to use the coaching technique based on the improved regularity. If the clinician wants to compare a third set of signals in which another technique or parameters are applied, he/she can use the third panel to evaluate the new signal.

Table 7-1: Measurements of the breathing data of the volunteer in two breathing modes.

Measurements	**Irregular Breathing**	**Regular Breathing**
SD of Period / mean of period	0.48	0.26
SD of local maxima	20.3	4.1
SD of local minima	9.4	2.9
Sum of weighted SD of Troughs	10.1	2.5
Sum of weighted SD of Peaks	17.8	3.9

7.1.7. Section Summary:

The presented program is new; similar functionality is currently not available in any other free or commercial system. It has been successfully used to evaluate the variations of breathing signals. By means of comparing several breathing signals at a time; the program provides quantitative indices to clinicians for decision making. For potential patients who breathe irregularly, the program could be used to practice breathing with this software with the aim of improving regularity.

Further work will be to combine the program with the ERM sampling wizard (chapter 7.3) and include visual feedback of the respiratory phase for patient training purposes.

7.2. Monitoring the Stability of Breathing: Online Detection of abnormal breathing behaviour

7.2.1. Introduction

The aim of this section is to develop and evaluate a real-time (online) abnormal activity detection algorithm. The algorithm was designed to work with the signals sampled from the ERM system, but it could also be adapted to other respiratory monitoring systems with some modifications.

7.2.2. Definition of Abnormal breathing activities

Coughing, talking, hiccups or sudden very deep breaths were classified as abnormal activities because these activities might compromise the normal synchronization between the tumour and the surrogate. Even if the abnormal activities do not compromise the synchronization, irregular breathing was found to increase the residual motion within the gating window (see chapter 4). We define abnormal breathing activities as a breathing pattern which is significantly different from the normal breathing pattern. "Normal breathing pattern" is defined as the repetitive pattern which appears most in the breathing signal of the patient. Clinicians can also define a segment of the breathing signal, based on experience, as the normal pattern. In such cases, any breathing pattern that is significantly different from the normal pattern is classified as abnormal.

7.2.3. Model for abnormal detection

The breathing signal has a cyclic property. Its pattern repeats, but with certain variations. The phase derived from the breathing signal indicates the state within a breathing cycle. If the AWA approach (see chapter 5) is used to derive the phase, the phase progresses linearly in regular breath patterns. Our model of abnormal breath activity detection is based on detecting abnormal changes of phase.

The detection algorithm operates as follow:

A breathing signal x_T, which is identified as the regular signal, is required to train the system. It aims to fine tune the detection threshold.

The average and mean of the rate of change of phase Q is calculated from the training signal. The rate of change of phase $Q[n]$, in general, is defined as:

$$Q[n] = \mathfrak{U}(\theta_H[n]) - \mathfrak{U}(\theta_H[n-1]) \qquad (7.51)$$

where $\mathfrak{U}(.)$ is a phase unwrap function, $\theta_H[.]$ is the Hilbert (AWA) phase. The length of $\theta_H[\ ]$ is N_x, which is the length of the training signal. The length of $Q[n]$ is N_x -1.

The rate of change of phase $Q_T[n]$ of the training signal can be derived by substituting the phase signal θ_T of the training signal into θ_H.

The mean $\overline{Q_T}$ and standard deviation δ_{QT} of the rate of change of phase $Q_T[n]$ help to define the upper bound and lower bound of the rate of change of phase Q of the test signal. A test signal is used to evaluate the performance of the abnormal activity detection algorithm. δ_{QT} is defined as the square root of the sample variance of $Q_T[n]$.

A test signal x[n] has a phase $\theta[n]$. The rate of change of phase $Q[n]$ is computed in real-time by Equation 7.51. Any instant t_i in the breathing signal can be classified as “regular” if and only if $Q[t_i]$ stays inside the upper and lower bound. The threshold is defined as:

$$\text{upper bound: } \overline{Q_T} - z \cdot \delta_{QT}$$

$$\text{lower bound: } \overline{Q_T} + z \cdot \delta_{QT}$$

The value of *z* determines the sensitivity of the abnormal activity detection. By assuming the elements of vector *Q* follow the normal distribution, we use a default value of 2.58 throughout our experiment. The chosen *z* value should be able to include 99.9% of the elements in the vector *Q*. The *z* value is a parameter to control the sensitivity of the detection. The system returns to the normal state after 4 seconds if no more abnormal breathing patterns are detected.

7.2.4. Evaluations

Six breathing signals were collected from 3 healthy volunteers (Volunteer 7, 8 & A).

Each of them first had 20 seconds of normal breathing signal to train the detection system. The testing signal of Volunteer A was 40 seconds of normal breathing and then followed by an abnormal session. In the Abnormal session, the volunteer was asked to talk or cough. After 90 seconds from the start of the sampling, the volunteer was asked to breathe normally for another 20 seconds. In addition to volunteer-A, 2 pairs of abnormal and normal signal breathing signals were selected from the coaching experiments (volunteers-7 & 8).

7.2.5. Results & Analysis

The talking and coughing activities were successfully detected from all the signals.

Figure 7-10 shows the detection result of Volunteer-7. The subject was fell asleep during the experiment. When the subject became less awake, the amplitude of the breathing decreased (the 700th-1500th samples of figure 7-10a). The algorithm detects the change of breathing pattern at the 1200th sample (the red trace of figure 7-10c), where the rate of change of the phase (the blue trace of figure 7-10b) exceeded the threshold. The subject awoke at the 1750th sample and took a deep breath. Since the deep breath was a significant change of breathing pattern, it was detected. For this dataset, the negative pulses in the 300th to 400th sample and the pulses at the end of the trace were also triggered by the abnormal change of amplitude.

The result of Volunteer-8 is shown in the figure 7-11. The subject fell asleep during the experiment (the 600th -800th sample on figure 7-11).

(a) breath signal of volunteer-7

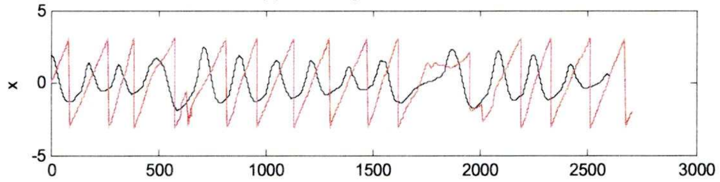

(b) Vector Q and upper/lower bounds

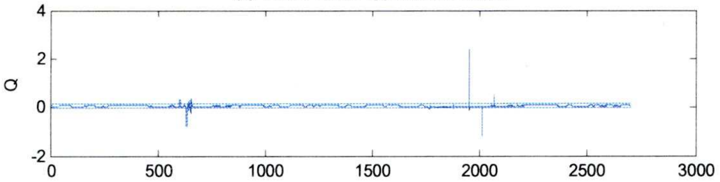

(c) Detection result

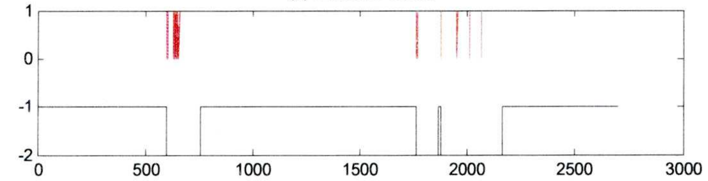

Figure 7-10: Abnormal detection in Volunteer-7. As the subjects fell asleep, the amplitude of breathing was reduced. The subject waked at 600th and 1700th samples. Hence, there was a sudden increase in amplitude in both positions. (a) The black trace on the upper graph is the breathing signal and the red trace is the phase signal. (b)The rate of change of phase Q[n] is shown. The two cyan horizontal lines are the upper and lower bounds of the normal breathing patterns

(c) the red trace is the abnormal trigger, where a high level (1) indicates that breathing is normal and a low level indicates that abnormal activity has been detected. The black trace is the result of the detection which included the 4-seconds abnormal-to-normal recovery time. The x-axis represents the time in sample units. The signal was sampled at 25Hz frequency.

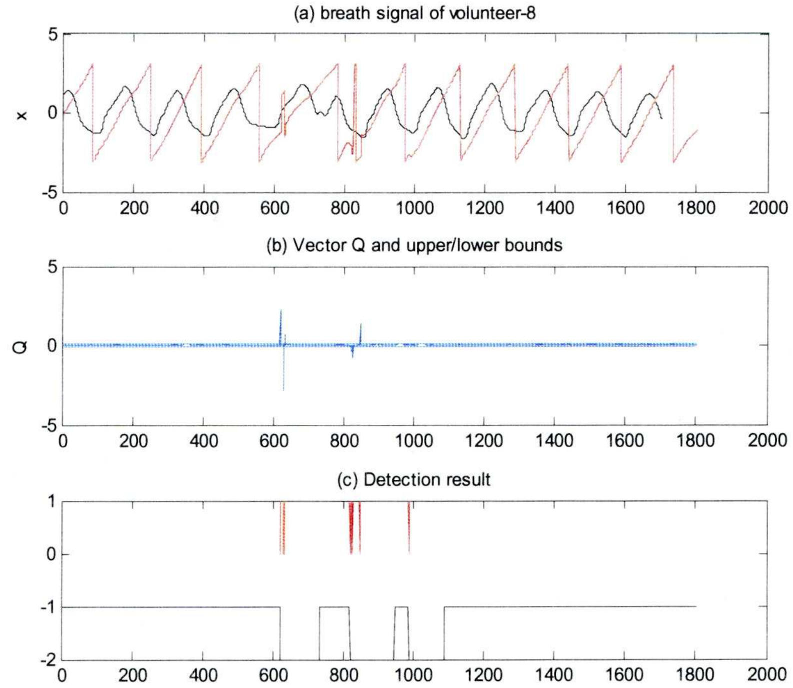

Figure 7-11: Abnormal detection in Volunteer-8. (a)The black trace is the breathing signal and the red trace is the phase signal.(b)The rate of change of phase Q[n]: The two cyan horizontal lines are the upper and lower bound of the normal breathing patterns. (c)the red trace is the abnormal trigger, where a high level (1) indicates that breathing is normal and a low level indicates that abnormal activity has been detected. The black trace is the result of the detection which included the 4-seconds abnormal-to-normal recovery time. The x-axis represents the time in sample units. The signal was sampled at 25Hz frequency.

The detection result of Volunteer-A is shown in the following figure 7-12. The subject was coughing between the 500th and 850thsample. The irregular patterns (the black trace of Figure 7-12) were detected in the red trace of the bottom chart.

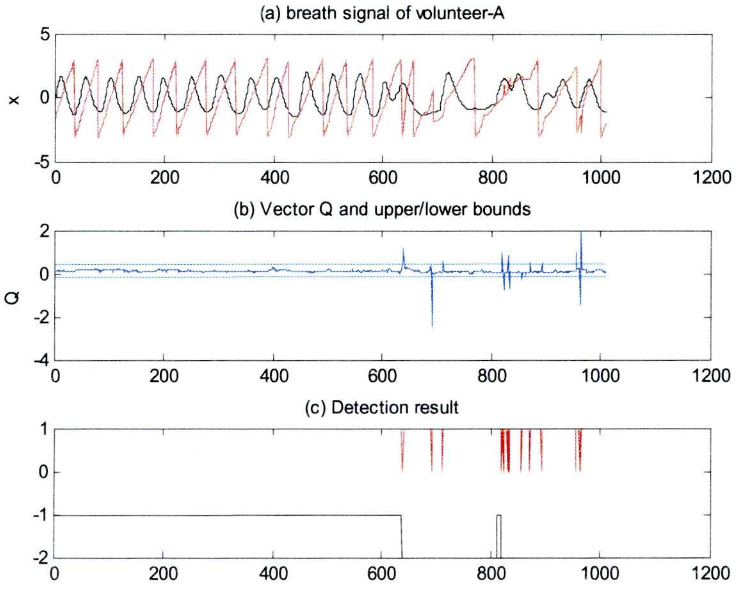

Figure 7-12: Abnormality detection in Volunteer-A.(a) The black trace is the breathing signal and the red trace is the phase signal. (b)The rate of change of phase Q[n] is shown. The two cyan horizontal lines are the upper and lower bounds of the normal breathing patterns. (c) The red trace is the abnormal trigger, where a high level (1) indicates that breathing is normal and a low level indicates that abnormal activity has been detected. The black trace is the result of the detection which included the 4-seconds abnormal-to-normal recovery time. The x-axis represents the time in sample units. The signal was sampled at 10Hz frequency.

7.2.6. Section Summary:

The irregular breathing detection algorithm proposed in this section was able to detect irregular breathing as results from coughing, talking and changes in breathing pattern. Due to the sudden change of airflow of these abnormal activities, the rate of change of phase $d\theta/dt$ goes beyond its normal value. Since the phase estimation algorithm is already a built-in feature of the gating system, it would take very little computational power to detect the phase derivative abnormalities.

Further work will be to compare the proposed algorithm with detecting the covariance matrix P in the EKF phase estimator. When using the EKF approach (Chapter 5.2.3) to estimate the phase, there is a covariance matrix which represents the error in the state estimation at every time step. An abnormality detection mechanism is needed for every gating system. When the ERM is used routinely for clinical purposes in the future, this algorithm will be integrated into the workstation program of the ERM.

7.3. Wizard based breathing signal sampling program

7.3.1. Problems:

A program is needed to communicate with the ERM from the ERM workstation.

When the ERM is started, the program would search for ports which the ERM is connected to, as an aim to simplify the start-up process. In order for the ERM to be able to communicate with other systems for experiment use or for controlling the LINAC, the program should have an interface to handle the external connections through an ADC.

The program should also provide real-time visual feedback for the operator and allow the signal to be saved for analysis.

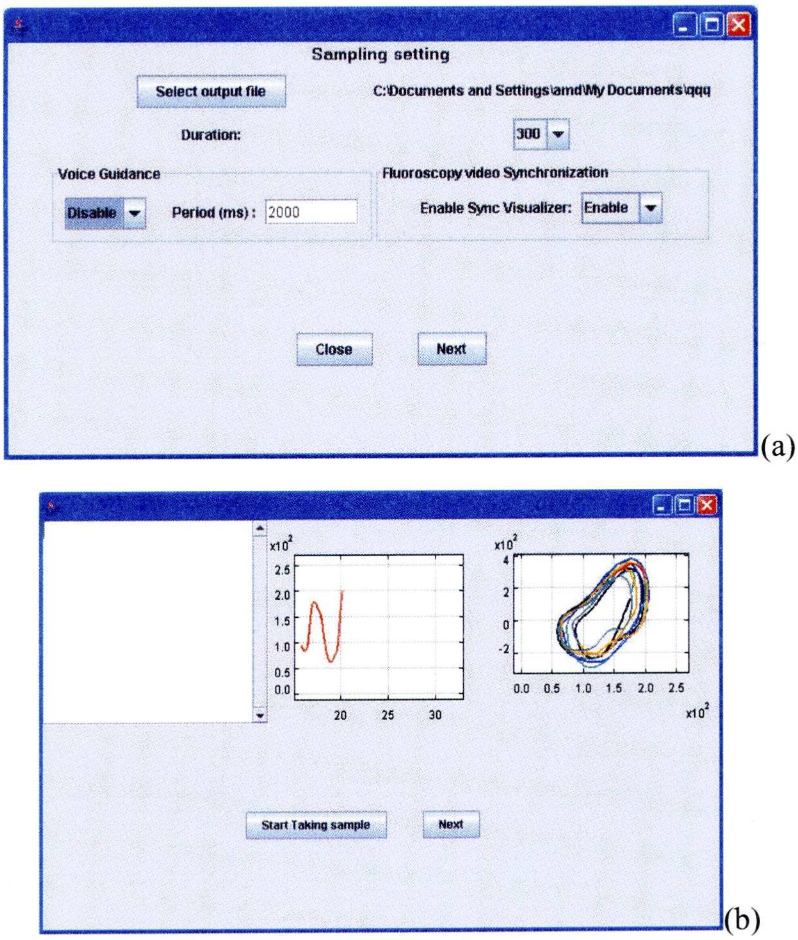

Sampling setting

C:\Documents and Settings\amd\My Documents\qqq

Duration: 300

Voice Guidance

Disable

Period (ms) : 2000

Fluoroscopy video Synchronization

Enable Sync Visualizer: Enable

Figure 7-13: User Interface of a Wizard based ERM sampling program. The signal of the ERM is plotted in the top middle chart. The natural phase of the signal is plotted in the top right hand side chart.

7.3.2. Method and Summary

A Wizard based sampling tool has been developed to take breathing samples using the ERM. The program addressed the functional requirements described in the problem section. The program was developed in JAVA (Sun Microsystems, Inc) to run on computers with VGA resolution or above. It provides visual feedback regarding the regularity of the breathing by natural phase trajectory (at the top right hand-side chart in figure 7-14 b). The software can read and write signals from/to an ADC for synchronization with other systems.

8. Discussion, Summary and Future Work

8.1. Discussion:

The aim of this study was primarily to investigate the performance of a piezo-electric based device (ERM) in respiratory monitoring. A number of respiratory monitoring systems have been developed: strain gauge, spirometer, thermocouple, abdominal surrogacy tracking, and implanted marker tracking. The behaviour of the ERM is similar to a thermocouple system in which the temperature of respiratory air flow is being monitored. Implanted marker target tracking has the problems of patient tolerance, extra dose to the patient and expensive equipment. A spirometer has the problems of portability and patient discomfort. Abdominal tracking and the strain gauge are less complex solutions.

Compared to the ERM, abdominal tracking (using the Varian RPM system) showed better temporal and spatial relationship with the tumour. However, it is difficult to monitor the displacement or movement of the abdomen in the application of stereotactic radiotherapy using abdominal compression or when the patient has been asked to minimise their breathing. Onishi *et al* (2004b) have shown that stereotactic radiotherapy combined with respiratory gating produced good local control of small lung tumours achieving a biologically effective dose at the isocenter of approximately 120 Gy. In order to carry out stereotactic lung treatments accurately it is important to have 4D-CT data, which improves the accuracy of target definition for treatment planning and also helps to assess the target motion. However, a respiratory signal is required to enable 4D scanning. Under such conditions, as long as the subject keeps breathing, the ERM can still detect the respiratory cycle for imaging and treatment.

A secondary aim was to investigate the impact of gating using the ERM device with different techniques. The subjects tend to breathe more deeply in audio coaching, causing the respiratory motion to increase. Thus, they feel more comfortable breathing at a slower coaching rate (in relation to their natural breathing rate) to maintain the same rate of gas exchange. In the fluoroscopy study of chapter 4, audio and visual coaching were applied for Patient-1, who had one of his lungs removed by surgery and consequently had impaired lung function. The audio-visual coaching technique reduces the RMS amplitude of residual-motion as well as the EOE and EOI variations, thereby allowing greater margin reduction when using respiratory gating for radiotherapy imaging, planning and treatment.

The Varian RPM measurements of abdominal motion were better correlated with tumour motion throughout each session as compared with the ERM breathing signal as shown in Chapter 4. This is because abdominal motion is more directly involved in a change in the diaphragm position than is the change of gas temperature in the face mask (to which the transducer of the ERM is attached). The average correlation between the ERM and the tumour SI motion was 0.81 ± 0.07. Although this is lower ($p=0.05$ by paired t-test) than that of the Varian RPM (mean 0.90 ± 0.09), it is still comparable to the surrogate-tumour correlations in other studies. Hoisak *et al* (2004) demonstrated a correlation with coefficients ranging between 0.51 and 0.98 between abdominal motion and lung-tumour motion. Ahn *et al (*2004) found an average correlation of 0.77 between skin and tumour movements with a range between 0.41 and 0.97. Mageras *et al.*(2001)investigated lung-tumour motion with respiration-correlated CT and found a correlation range of 0.73 to 0.96.The results of gated radiotherapy simulations and the correlation between the breathing signal and the internal motion support the argument that the ERM is capable of reducing the standard deviations of the motion of the target when the radiation beam was enabled.

When comparing the Experimental Respiratory Monitor (ERM) with the commercial device (Varian RPM), the degree of residual motion reduction with the ERM was not as good as the commercial system in amplitude gating. The reasons for this are (1)the systematic delay between the ERM signal and the tumour motion, as well as (2)the lack of correlation between the amplitude of the ERM signal and amplitude of the tumour motion. Prediction algorithms and phase gating have been investigated to improve its performance.

The Varian RPM system has two gating modes built into the system: Amplitude gating and Phase gating. Phase gating employs an instantaneous phase estimator; the beam is controlled by the phase signal produced by the estimator. Unlike the Varian system, the ERM needs an algorithm to estimate the instantaneous phase. The AWA approach and the EKF approach have both been investigated. On average the EKF was slightly superior to the AWA. However, the EKF was relatively more complicated to implement. Moreover, EKF is less stable, because of the recursive state estimations. The results of Chapter 5 showed that if amplitude gating was properly compensated in time, there is no significant difference between phase gating and amplitude gating. However, in some cases, the difference in the residual motion between phase and amplitude gating can be as large as 15% rRMS. This suggests that the use of phase gating has to be judged on an individual patient basis.

The accuracy of a number of prediction algorithms has been evaluated in chapter 6. It has been shown that, for prediction horizon of 0.5s, the Adaptive Linear (NLMS) algorithm was preferred. With an average of about 10% further reduction in the rRMS of residual motion, the prediction algorithm improved the accuracy of the ERM on nearly most of the datasets (with the assumption of 120ms control delay). We found that using a prediction algorithm was effective in compensating the systematic delay of the ERM.

Regarding other respiratory monitoring systems, we expect that the sampling rate of the systems as well as their accuracy will improve and the response time of the beam delivery system will be reduced in the future. However, the systematic delay between the gating surrogate and the tumour, being another source of major delays, is highly dependent on individual subjects. Moreover, from the results of chapter 4, the effect of it on the residual motion was significant. Systematic phase differences of surrogates have also been found by Cerviño *et al* (2009) and Hoisak *et al* (2004). Therefore, gating system prediction algorithms with a large prediction horizon will be still required. Hoisak *et al* (2004) studied the reproducibility of 5 patients over multiple days. They found that only 1 patient exhibited a reproducible interfractional phase relationship. The existence of an interfractional variation in phase difference contradicts the assumptions of constant systematic delay of the surrogate. Therefore, the systematic delay should be validated before each session of treatment. Failure to do so may result in a geographic miss of the tumour if radiotherapy is guided with surrogates.

The Clatterbridge Centre of Oncology (CCO) has been using conventional 3D-CT scans consisting of images without time information from the moving tumour and anatomy for radiotherapy planning. The image-set obtained from the 3D-CT scan is an arbitrary snapshot. The uncertainty results in an undefined displacement of the tumour with respect to the mean tumour position. Tumour shape deformation in the image can occur because the reconstruction algorithm assumes a static volume.

In conventional treatment, the breathing of the patient is not restricted by any respiratory control or monitoring devices, this introduces tumour position uncertainty. Four-dimensional computed tomography (4D-CT) provides a more reliable basis than conventional 3D-CT scanning. In 4D-CT, data acquired over several breathing cycles are sorted to produce a sequence of 3D image sets, each at a different phase of the breathing cycle. In addition to tumour motion measurements, the data permit calculation of the dose to moving anatomy, which is especially important for the accurate determination of target coverage. The images themselves exhibit fewer motion artefacts and therefore reduce the uncertainty associated with target delineation. However, even with the precise delivery of radiation permitted by PTV margin reduction; there remains significant uncertainty in defining the biological target to which that margin is applied. Target definition combining CT and other imaging modalities (known as modal fusion), such as PET and MRI, is likely to reduce this uncertainty.

At CCO, the CTV to PTV margin for non-gated 3D planning ranges from 5 to 10mm. The value depends on the size and the location of the tumour. If the tumour is close to critical organs and would result in an unacceptable dose to these, the clinician will use a smaller margin. Therefore, to estimate a uniform setup margin for lung patients based on our population, in this work we have been applying the general margin recipe from van Herk *et al* 2002.

Margins in the conditions of online correction

Respiration motion contributes to both systematic (during imaging) and random errors (during treatment); therefore, a reduction in the effective respiration motion will affect both these contributors. Imaged guided online corrections, which align the GTV to the beam before each treatment, could reduce the systematic error by a significant amount. Despite accurate online correction strategies, residual uncertainties will always remain in target definition, treatment delivery, and because of respiratory motion, safety margins are still required. For each patient individually, the margin M_{PTV} necessary to deliver a dose of at least 95% of the prescribed dose to the CTV (for 90% of the population) can be computed by the following margin recipe of van Herk *et al* (2002):

$$M_{PTV} = 2.5\Sigma + 1.64\sqrt{\sigma^2 + {\sigma_p}^2} - 1.64\sigma_p \qquad (8.1)$$

where Σ and σ denote the standard deviations of the systematic errors (localization errors in planning imaging) and random errors (localization errors during treatment), respectively. σ_p denotes the standard deviation of the dose gradient and describes the width of the penumbra modelled by a cumulative Gaussian. In lung, where the penumbra is broader, the width of the penumbra was estimated at σ_p = 6.4mm. The various components of the systematic and random uncertainties are summed in quadrature to generate the margin .The value of the SD of the random error distribution σ was obtained by the square root of the sum of squares of SD of the random components of the localization accuracy, intrafractional stability, and respiratory motion. The value of Σ was obtained by the square root of the sum of squares of the SD of the systematic component of localization accuracy, intrafractional stability, and delineation uncertainty.

Although delineation uncertainty is more a shape change than a translation, Deurloo *et al* 2002 showed that delineation uncertainties can be modelled by a simple shift. Steenbakkers *et al* (2005) showed that the delineation uncertainty is generally large (up to 6 mm SD) for lung tumours. For simplicity, the systematic error of delineation Σ_{del}=6 (mm) is used for all the patients. The interfraction baseline variation (day-to-day variation) and treatment setup uncertainty were referenced from 4D respiration-correlated cone-beam CT data from the patient group in Snoke *et al* 2008 and Erridge 2003.An overview of the error contributions for the different approaches is given in Table 8-1, while the margins due to respiratory motion of each individual patient are shown in Table 8-2. In Table 8-2, the standard deviation of the random error of respiratory motion of non-gated and gated radiotherapy were listed for comparison. The technique used was exhale gating with a 30% duty cycle using AWA phase gating (for Patient 4 and 5) and the ERM was used as the breathing monitor. Amplitude gating was used for Patient 1, 2 and 3. Since Patient-1 exhibited smaller residual motion in the inhale position, the residual motion of inhale was used for this patient. The tumour motion of the IS direction was the average of the IS motion in the AP and Lateral view.

Table 8-1The systematic and random uncertainties for the margin calculations with image guided online verification. The σ_x ,σ_y and σ_z values for each patient can be found in Table 8-2. The units of the above table are millimetre (mm).

	Systematic (Σ)			**Random (σ)**		
	LR	**SI**	**AP**	**LR**	**SI**	**AP**
Delineation	6.0	6.0	6.0	-	-	-
Baseline	-	-	-	1.2	2.4	2.2
Setup	1.4	1.5	1.3	2.9	3.1	2.0
Respiratory	-	-	-	σ_x	σ_y	σ_z

Table 8-2 The Standard deviation of periodic motion σ_x , σ_y and σ_z of the LR, SI and AP directions. Gating was enabled in the Exhale position (except for Patient-1, who exhibited smaller residual motion in inhale who was gated in the inhale position).

Standard deviation of Residual Motion (mm)					
			No-gating		
	Patient-1	**Patient-2**	**Patient-3**	**Patient-4**	**Patient-5**
σ_x	0.5	0.4	2.0	0.9	0.3
σ_y	4.3	1.4	4.3	6.2	2.7
σ_z	0.5	0.8	1.3	1.2	0.7
			30% phase gating		
σ_x	0.2	0.2	0.2	0.2	0.2
σ_y	1.8	0.8	1.3	1.0	1.0
σ_z	0.2	0.1	0.3	0.2	0.7

The PTV margin ranged from 17 to 21mm in non-gated radiotherapy (Table 8-3). In the PTV margin of gated treatment: Patient-1, Patient-3 and Patient-4 achieved a margin reduction of 1.5mm, 1.7mm and 3.5mm in the SI direction respectively. The margin reductions of other directions and of other patients were below 1 mm. Hence, the average reductions were small. The percentage reduction from non-gated to gated treatment ranged from 1% to 17%. However, by using the gating technique, Patient-4, being the patient having the largest tumour motion, could still benefit from a significant reduction of PTV margin. The result supports the argument that gated radiotherapy does not reduce the margin significantly in all the patients. However, there still exists a proportion of patients who can benefit from the technique and it must be remembered that the small number of patients in this sample did not show tumour movements as large as some of those reported in the literature

	PTV margin (mm)				
No-gating	**Patient-1**	**Patient-2**	**Patient-3**	**Patient-4**	**Patient-5**
σ_x	16.6	16.6	17.1	16.7	16.6
σ_y	19.2	17.5	19.1	20.9	18
σ_z	16.5	16.5	16.6	16.6	16.5
30% phase gating					
σ_x	16.6	16.6	16.6	16.6	16.6
σ_y	17.6	17.3	17.5	17.4	17.4
σ_z	16.4	16.4	16.4	16.4	16.5

Table 8-3 The PTV margin of in the LR, SI and AP directions of the 5 patients in gated and non-gated radiotherapy using the ERM as the respiratory monitor.

For both amplitude and phase gating, the rRMS residual-motion standard deviations were lower for exhale compared with the respective inhale values in most of the datasets. Moreover, the EOI position variations were larger than those of the EOE. This supports the general notion that the exhale position is more reproducible and that the patient spends more time at exhale than at inhale. The advantage of treating at inhale as opposed to exhale is that the lung volume is larger than at exhale and, therefore, the mass of lung receiving radiation is less at inhale as compared with exhale. According to the study conducted for Patient-4, the patient has the largest reduction (5.2mm) in the SI direction of tumour motion in 30% duty cycle gated treatment at EOI position. If the patient was treated at the EOI position, the residual motion became 4.2mm. Then, the PTV margin would be increased by 0.3mm. However, this is unlikely to have any significant impact on dose escalation. Moreover, by using audio-visual coaching, we may be able to reduce the variation of EOI positions. If the Varian RPM is used for respiratory monitoring, the margin could be reduced by 0.1mm for Patient 2 to 5, while the margin of Patient-1 could be reduced by 0.4mm. Hence, the different between the two monitoring devices in margin reduction is small for most of the patients.

PTV margin of Gating VS non-gating

A paired t-test was used to evaluate the statistical significance of 30% duty cycle gating versus no-gating in the IS direction using the ERM as the breath monitor.

H_0: $\sigma_{y0}= \sigma_{y30}$

H_1: $\sigma_{y0}> \sigma_{y30}$

where $\sigma y0$ is the PTV margin in the SI direction without gating and $\sigma y30$ is the margin using gating with 30% duty cycle. The difference between the PTV margins was significant ($p=0.029$) with $\beta=0.78$.

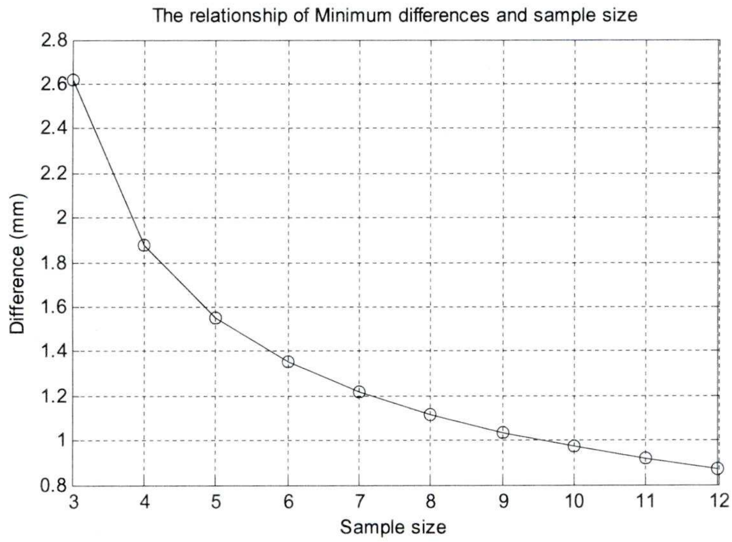

Figure 8-1: Sample size in Paired T-test using $\alpha=0.05$, $\beta=0.8$ using the data of the PTV margin in IS direction (σ_y) in Table 8-3.

The relationship of Minimum differences and sample size was shown on Figure 8-1 (computed by the Statistic Toolbox of Matlab, Mathworks). Six samples are needed to test for the significance of the difference of the two margins at $\alpha=0.05$, $\beta=0.8$. To detect a 1-mm differences of the means, the sample size should be at least 10 at $\alpha=0.05$, $\beta=0.8$. In this thesis, the patient sample size is 5, hence, the minimum difference E it can test is 1.55mm.

If there were 1 more sample and gating produced a smaller margin, the result of the hypothesis test could become significant at $\alpha=0.05$, $\beta=0.8$ with $p=0.03$.

Owing to the small number of samples, the nonparametric Friedman's test was also used to evaluate the statistical significance of the PTV margin. The PTV margins were grouped into columns of no-gating and 30% duty cycle gating. The test showed there was a significant different between the two approaches ($p=0.03$).

However, when using the Wilcoxon signed rank test, the null hypothesis could not be rejected (p=0.06) because the sample size was only 5. With one additional sample which gating produced beneficial effect, the null hypothesis can be rejected (p=0.03).

8.2. Conclusions

The (Experimental Respiratory Monitor ERM) device has been further developed and adapted for respiratory gating:

- The electronic design of the ERM has been verified and some changes have been made to improve its usability in the field of respiration monitoring for respiratory gating.
- A wizard based program has been developed to monitor the phase (Natural phase) of the ERM in real time while the breathing of the patient is being monitored.
- A synchronization system between the ERM and other systems (fluoroscopy, CT scanner) has been developed.
- A program has been developed to analyse the regularity of four recorded breathing signals simultaneously. By using the program, clinicians have instant feedback on the regularity of respiration to guide clinical decisions. The software could be used as a training aid for patients.
- An algorithm has been developed to monitor abnormal breathing by detecting sudden phase changes in the breathing signal.

The impact of audio coaching was investigated by analysing the breathing samples of 9 healthy volunteers using audio coaching.

- It was found that audio coaching increased the amplitude of breathing in most of the subjects. As the amplitude of breathing increased it was found that the variability of the amplitude also increased. Consequently audio coaching increased the variability of breathing amplitude.
- A program using the Hilbert transform was developed to derive the phase signal and to measure the variation of the breathing cycle. This provided a methodology for breathing cycle analysis for gating.

Based on the 12 datasets of fluoroscopy results from 5 lung cancer patients,

- It has been shown that the experimental system (ERM) is able to reduce PTV margin in gated radiotherapy.
- When comparing the experimental system (ERM) with the commercial system(Varian RPM) in terms of the synchronisation of the gating signal with tumour movement, it was found that the raw signal from the experimental system was less well correlated with tumour motion than that of the commercial system. The stability and the systematic delays of the experimental system for amplitude gating were less satisfactory than that of the commercial system.
- The systematic delays could be compensated by prediction algorithms and resulted in a significant reduction in residual motion.

The use of the Extended Kalman Filter and the Autocorrelation function to estimate the breathing phase in real time has been investigated in order to improve the reproducibility.

- The two approaches produced similar results, but the EKF approach was slightly better than the autocorrelation approach.
- The residual motion difference of phase and amplitude gating has to be determined on a case by case basis.

8.3. Future Work:

The results of the fluoroscopy study showed that the signal from the ERM and the tumour motion were not well synchronized in the Exhale phase in one patient. Further investigation is needed to find out why and how frequently this happens in patients.

In order to facilitate the clinical use of the ERM for gated radiotherapy, more patients need to be recruited to confirm that the signal of the ERM is well synchronized with the tumour motion.

The breathing regularity assessment program has yet to be applied clinically. The usefulness of this system as an aid to patient training should be investigated. Furthermore, more experience with using the ERM on patients is needed in order to assess its usefulness in assessing patient suitability for gated treatment.

Further work needs to be done with patients with large tumour movements. The patients included in this study did not have particularly large movements and the margin reduction recorded in Table 8-3 may have limited clinical benefits. However, the approach of Van Herk *et al* assumes that the motion of the tumour can be satisfactorily represented by a Gaussian which may not be the case for all patients, particularly with large tumour excursions. A more detailed investigation of the gain of TCP for fixed NTCP/decrease in NTCP at fixed TCP with a wider group of patients should be carried out.

9. Reference

Ahn, S., Yi, B., Suh, Y., Kim, J., Lee, S., Shin, S., Shin, S. & Choi, E., (2004). A feasibility study on the prediction of tumour location in the lung from skin motion, *British Journal of Radiology*, **77(919),**588-596.

Antolak J.A. and Rosen I.I., (*1999*) Planning target volumes for radiotherapy: How much margin is needed? *International Journal of Radiation Oncology Biology Physics***44**, 1165–1170

Askanazi, J.,Silverberg, P.A., Foster, R.J., Hyman, A., Milic-Emili, J.&Kinney, J.M.,(1980). Effects of respiratory apparatus on breathing pattern, *Journal of Applied Physiology,***48(4),**577-580.

Bar-Shalom, Y., Li, X.R. & Kirubarajan, T. (2001). *Estimation with Applications to Tracking and Navigation.*Wiley-Interscience

BarnesE.A., Murray B.R. and Robinson D.M. *et al.* (2001)Dosimetric evaluation of lung tumor immobilization using breath hold at deep inspiration, .*International Journal of Radiation Oncology Biology Physics***50**, 1091–1098

Balter J. M., Ten Haken R. K., Lawrence T. S., Lam K. L., Obertson J. M.(1996). Uncertainties in CT-based radiation therapy treatment planning associated with patient breathing. *International Journal of Radiation Oncology Biology Physics,***36,** 167-174.

Balter, J. M., Lam, K. L., McGinn, C. J., Laerence T. S., Ten Hakan, R. K., (1998). Improvement of CT-based treatment-planning models of abdominal targets using static exhale imaging. *International Journal of Radiation Oncology Biology Physics,***41,** 939–943.

Balter, J.M., Wright, J., Newell, L., Friemel, B., Dimmer, S., Cheng, Y., Wong, J.,Vertatschitsch, E. & Mate, T., (2005). Accuracy of a wireless localization system for radiotherapy, *International Journal of Radiation OncologyBiologyPhysics,* **61(3)**, 933-937

Baumgartner, E.T. & Skaar, S.B., (1994), An autonomous vision-based mobile robot, IEEE Transactions on Automatic Control, *IEEE Transactions on Automatic Control,* **39(3),** 493-502.

Bechbache RR, Chow HHK, Duffin J & Orsini EC (*1979*). The effects of hypercapnia, hypoxia, exercise and anxiety on the pattern of breathing in man. *J Physiol****293****, 285*–300

Berbeco, R.I., Nishioka, S., Shirato, H., Chen, G.T.&Jiang S.B., (2005), Residual motion of lung tumours in gated radiotherapy with external respiratory surrogates, *Physics in Medicine and Biology,* **50(16),**3655-3667.

Berbeco, R.I., Mostafavi, H., Sharp, G.C. & Jiang, S.B.(2005b), Towards fluoroscopic respiratory gating for lung tumours without radiopaque markers *Physics in Medicine and Biology,* **50,** 4481-4490.

Bogoliubov, N.N. & Mitropolski, Y.A. (1961). *Asymptotic Methods in the Theory of Nonlinear Oscillations*, Gordonand Breach, NewYork, 1961.

Borst, G.R., Sonke, J,J, Betgen, A., Remeijer, P., van Herk, M. & Lebesque, J.V. (2007). Kilo-Voltage Cone-Beam Computed Tomography Setup Measurements for Lung Cancer Patients; First Clinical Results and Comparison With Electronic Portal-Imaging Device. *International Journal of Radiation Oncology Biology Physics,* **68(2),** 555-561.

Bortfeld, T., Jokivarsi, K., Goitein, M., Kung, J. & Jiang, S.B., (2002). Effects of intra-fraction motion on IMRT dose delivery: statistical analysis and simulation, *Physics in Medicine and Biology,* **47(13),** 2203-2220.

Bortfeld, T, Jiang, S.B.& Rietzel, E., (2004) Effects of Motion on the Total Dose

Distribution, *Seminars in Radiation Oncology,* **14(1),**41-51.

Brown, R.G. & Hwang, P.Y., (1983). *Introduction To Random Signal Analysis And Kalman Filtering,* John Wiley & Sons, New York, pp181.

Bruce E. N., (1996). Temporal variations in the pattern of breathing. *Journal of applied physiology,* **80(4),**1079-1087.

Cerviño, L.I., Chao, A.K.Y., Sandhu, A. & Steve B. Jiang, (2009). The diaphragm as an anatomic surrogate for lung tumor motion, *Physics in Medicine and Biology,* **54(11),**3529-3541.

Chi, P. C., Balter, P., Luo, D., Mohan, R.& Pan, T., (2006). Relation of external surface to internal tumour motion studied with cine CT, *Medical Physics,* **33(9),** 3116-3123.

Cheung, P. C. , Sixel, K. E., Tirona, R.&Ung, Y. C., (2003). Reproducibility of lung tumour position and reduction of lung mass within the planning target volume using active breathing control (ABC). *International Journal of Radiation OncologyBiologyPhysics,* **57(5),** 1437–1442.

Chow, S. C., Wang H., Shao J., (2003). *Sample Size Calculations in Clinical Research*, CRC Press, New York, pp15.

Chui, C. S., Yorke E. & Hong, L., (2003). The effects of intra-fraction motion on the delivery of intensity-modulated field with a multileaf collimator, *Medical Physics,* **30,** 1736–1746.

Coopers, S. & Durrant-Whyte, H. (1994). A Kalman filter model for GPS navigation of land vehicles, Proceedings of the IEEE/RSJ/GI International Conference on Intelligent Robots and Systems '94. 'Advanced Robotic Systems and the Real World', IROS '94, **1(1),**157-163.

Cox, J.E., Chiles, C., McManus, C.M., Aquino, S.L., & Choplin, R.H. (1999) Transthoracic needle aspiration biopsy: Variables that affect risk of pneumothorax, *Radiology,* **212,** 165–168.

DeShazer D.J., Breban R., Ott E., and Roy R. (2001) Phys. Rev. Lett.**87.4**

Diniz P.S.R., Da Silva E.A.B.& Netto S.L.,(2002).*Digital Signal Processing,* Cambridge University Press, Cambridge.

Dawson, L.A., Brock, K.K., Kazanjian, S., Fitch D., McGinn, C.J., Lawrence, T.S.,Ten Haken R. K.& Balter J., (2001). The reproducibility of organ position using active breathing control (ABC) during liver radiotherapy1. *International Journal of Radiation OncologyBiologyPhysics,* **51(5),**1410–1421.

Dougherty,C. (2002). *Introduction to econometrics.* Oxford University Press, USA.

Engelsman, M., Sharp, G.C., Bortfeld, T., Onimaru, R. & Shirato, H., (2005). How much margin reduction is possible through gating or breath hold?, *Physics in Medicine and Biology,* **50,** 477-490.

Ernst, F. & Schweikard, A., (2008). Predicting respiratory motion signals for image-guided radiotherapy using multi-step linear methods (MULIN), *International Journal of Computer Assisted Radiology and Surgery,* **3(1-2),** 85-90.

Ernst, F., Schlaefer, A., Dieterich, S & Schweikard, A. (2008). *A Fast Lane Approach to LMS prediction of respiratory motion signals,* **3(4),** 291-299.

Erridge, S., Seppenwoolde, Y., Goedbloed, C., Heemsbergen, W., Muller, S., van Herk, M., De Jaeger, K., Belderbos, J.S., Boersma, L. & Lebesque, J.V. (2001). Portal imaging to assess setup errors, tumor motion and tumor shrinkage during conformal radiotherapy for non-small cell lung cancer. *International Journal of Radiation Oncology Biology Physics,* **5(1),** 207-208.

Fish,G.D., Stanley J.H., Miller, K.S., Schabel, S.I. & Sutherland, S.E.(1988). Postbiopsy pneumothorax: Estimating the risk by chest radiography and pulmonary function tests, *American Journal of Roentgenology,* **150(1),**71–74.

Ford, E.C., Mageras, G.S., Yorke, E., Rosenzweig, K.E., Wagman, R. & Ling, C.C., (2002). Evaluation of Respiratory Movement During Gated Radiotherapy Using Film and Electronic Portal Imaging, *International Journal of Radiation OncologyBiologyPhysics,* **52(2),**522–531.

Ford, E.C., Mageras, G.S., Yorke, E. & Ling, C.C., (2003). Respiration-correlated spiral CT: A method of measuring respiratory-induced anatomic motion for radiation treatment planning, *Medical Physics,* **30(1),** 88-97.

Fox, J.L., Rengan, R., O'Meara, W., Yorke, E., Erdi, Y., Nehmeh, S., Leibel, S.A. &Rosenzweig, K.E. (2005). Does registration of PET and planning CT images decrease interobserver and intraobserver variation in delineating tumor volumes for non-small-cell lung cancer?, *International Journal of Radiation Oncology Biology Physics,* **62(1),**70-75.

Frazier, R.C., Vicini, F.A., Sharpe, M.B., Yan, D., Fayad, J., Baglan, K., Kestin, L., Remouchamps, V., Martinez, A.& Wong, J.W., (2004). Impact of breathing motion on whole breast radiotherapy: A dosimetric analysis using active breathing control. *International Journal of Radiation OncologyBiologyPhysics,* **58(4),**1041-1047.

Freund J.A., Schimansky-Geier, L. & Hänggi, P., Frequency and phase synchronization in stochastic systems, *Chaos,* **13(1),**225-238.

Giraud, P., Elles, S., Helfre, S., De Rycke, Y., Servois, V., Carette, M.F., Alzieu, C., Bondiau, P.Y., Dubray, B., Touboul, E., Housset, M., Rosenwald, J.C. &Cosset, J.M. (2002). Conformal radiotherapy for lung cancer: different delineation of the gross tumor volume (GTV) by radiologists and radiation oncologists, *Radiotherapy and Oncology*, **62(1),** 27-36.

Goodband, J.H., Haas, O.C. & Mills, J.A., (2008). A comparison of neural network approaches for on-line prediction in IGRT.*Medical Physics,***35(3),** 1113-22.

Hanley J, Debois MM, Mah D, Mageras GS, Raben A, Rosenzweig K, Mychalczak B, Schwartz LH, Gloeggler PJ, Lutz W, Ling CC, Leibel SA, Fuks Z, Kutcher GJ. (1999) Deep inspiration breath-hold technique for lung tumors: the potential value of target immobilization and reduced lung density in dose escalation. *Int J Radiat Oncol Biol Phys.* 45(3):603-11.

Harada, T., Shirato, H., Ogura, S., Oizumi, S., Yamazaki, K., Shimizu, S., Onimaru., R., Miyasaka, K., Nishimura, M. & Dosaka-Akita, H., (2002). Real-time tumor-tracking radiation therapy for lung carcinoma by the aid of insertion of a gold marker using bronchofiberscopy, *Cancer*, **95(8)**, 1720–1727.

Imura, M., Yamazaki, K., Shirato, H.,Onimaru, R., Fujino, M., Shimizu, S., Harada, T., Ogura, S., Dosaka-Akita, H., Miyasaka, K. & Nishimura, M., (2005). Insertion and fixation of fiducial markers for setup and tracking of lung tumors in radiotherapy, *International Journal of Radiation OncologyBiologyPhysics,***63(5),** 1442–1447.

Isaksson M. and Jalden J. (2005) On using an adaptive neural network to predict lung tumor motionduring respiration for radiotherapy applications Med. Phys. **32(12)**, 3801-3809.

Jang J.S.R., Sun C.T. (1995) Neuro-Fuzzy Modeling and Control. PrpceedingsofThe IEEE, **83(3)**, 378-406

Mazeika, G.G.&Swanson, R., (2007).*Respiratory Inductance Plethysmography, An Introduction.* Pro-Tech Services, Inc.

Ganong, W.F., (2003). *Review of medical physiology,* McGraw-Hill, p653-654.

Gaydecki, P. (2004). *Foundations of digital signal processing: theory, algorithms and hardware design (IEE circuits, devices and systems series).* The Institution of Engineering and Technology.

George, R., Chung, T.D., Vedam, S.S., Ramakrishnan, V., Mohan, R., Weiss, E. & Keall, P.J., (2006). Audio-Visual Biofeedback for Respiratory-Gated Radiotherapy: Impact of Audio Instruction and Audio-Visual Biofeedback on Respiratory-Gated Radiotherapy, *International Journal of Radiation Oncology Biology Physics,* **65(3),** 924-33

Geraghty, P.R., Kee, S.T., McFarlane, G., Razavi. M.K., Sze, D.Y., & Dake M.D., (2003). CT-guided transthoracic needle aspiration biopsy of pulmonary nodules: needle size and pneumothorax rate. *Radiology,* **229,**475–481

Gilbert, R., Auchincloss, J.H. Jr., Brodsky, J. & Boden, W., (1972). Changes in tidal volume, frequency, and ventilation induced by their measurement. *Journal of Applied Physiology,* **33(3),** 252-254.

HaasbeekC.J.A., Spoelstra F.O.B. and Lagerwaard F.J. *et al.*(2008) Impact of audio-coaching on the position of lung tumors, *International Journal of Radiation Oncology Biology Physics* **71**, 1118–1123

Hanley, J., Debois, M., Mah, D., Mageras, G.S., Raben, A., Rosenzweig, K., Mychalczak, B., Schwartz, L.H., Gloeggler, P.J., Lutz, W., Ling, C.C., Leibel, S.A., Fuks, Z& Kutcher, G.J., (1999) Deep Inspiration Beath-hold Technique For Lunf Tumours: The Potential Value Of Target Immobilization And Reduced Lung Density In Dose Escalation, *International Journal of Radiation Oncology Biology Physics,* **45(3),**603–611.

Hartikainen, J.&Särkkä, S., (2008),*Optimal filtering with Kalman filters and smoothers - aManual for Matlab toolbox EKF/UKF.*Department of Biomedical Engineering and Computational Science, Helsinki University of Technology, Espoo, Finland.

Hoisak, J., Sixel, K., Tirona, R., Cheung, P. & Pignol, J.(2004). Correlation of lung tumor motion with external surrogate indicators of respiration. *International Journal of Radiation Oncology Biology Physics,* **60(4),** 1298-306.

Hugo, G.D., Agazaryan, N. & Solberg, T.D., (2002). An evaluation of gating window size, delivery method, and composite field dosimetry of respiratory-gated IMRT, *Medical Physics*, **29(11),**2517- 2525.

Hugo, G.D., Agazaryan, N. & Solberg, T.D., (2003). The effects of tumour motion on planning and delivery of respiratory-gated IMRT, *Medical Physics,* **30(6),** 1052-1066.

Jiang, S.B., Pope, C., Al Jarrah, K.M., Kung, J.H., Bortfeld, T. & Chen, G.T., (2003). An experimental investigation on intra-fractional organ motion effects in lung IMRT treatments, *Physics in Medicine and Biology,* **48(12),**1773-1784.

Kakar, M., Nyström, H., Aarup, L.R., Nøttrup, T.J. & Olsen, D.R. (2005). Respiratory motion prediction by using the adaptive neuro fuzzy inference system (ANFIS).*Physics in Medicine and Biology,* **50**, 4721–4728.

Kay, J., Strange-PetersenE., and Vejby-Christensen H.(1975) Mean and breath-by-breath pattern of breathing in man during steady-state exercise. *J. Physiol. Lond.* **251**: 657-669.

Keall, P.J., Kini, V.R., Vedam, S.S.&Mohan, R., (2001). Motion adaptive x-ray therapy: a feasibility study, *Physics in Medicine and Biology,* **46(1),** 1-10.

Keall, P.J., Todor, A.D., Vedam, S.S., Bartee, C.L., Siebers, J.V., Kini, V.R. & Mohan, R., (2004).On the use of EPID-based implanted marker tracking for 4D radiotherapy, *Medical Physics,* **31,** 3492-3499.

Keall, P.J., Mageras, G.S., Balter, J.M., Emery, R.S., Forster, K.M., Jiang, S.B., Kapatoes, J.M., Low, D.A., Murphy, M.J., Murray, B.R., Ramsey, C.R., van Herk, M.B., Vedam, S.S., Wong, J.W. & Yorke, E., (2006). The management of respiratory motion in radiation oncology report of AAPM Task Group 76, *Medical Physics,* **33(10),** 3874-3900.

Kee, D., Steenbakkers, R.J.H.M., Nowak, P.H.C.M., Oral Simulation of the combined effect of delineation variation, setup error and organ motion, R*adiotherapy Oncology,***64(Suppl. 1)**,S115.

Kimura, T., Hirokawa, T., Murakami, Y., Tsujimura, Ohishi, Y., Nakashima, T., Yamada, K., Ohno, Y., Kenjo, M. & Kaneyasu, Y. (2004) Koichi Wadasaki, Katsuhide Ito, Reproducibility of organ position using voluntary breath-hold method with spirometer during extracranial stereotactic radiotherapy, *International Journal of Radiation Oncology,Biology,Physics,***57(2)**, S428

Kini V.R., Vedam S.S., Keall P.J., Patil, S., Chen, C. & Mohan, R., (2003). Patient training in respiratory-gated radiotherapy. *Medical Dosimetry,***28(1),** 7-11.

Klopotek, M.A., Wierzchon, S., & Trojanowski, K. (2005). *Intelligent information processing and web mining : proceedings of the international IIS: IIPWM'05 Conference held in Gdansk, Poland, June 13-16, 2005.* Springer.

Koch, N., Liu, H.H., Starkschall, G., Jacobson, M., Forster, K., Liao, Z., Komaki, R. & Stevens, C.W., (2004), Evaluation of internal lung motion for respiratory-gated radiotherapy using MRI: part I-correlating internal lung motion with skin fiducial motion,*International Journal of Radiation Oncology Biology Physics,***60(5),**1459-1472.

Kothary, N., Dieterich, S., Louie, J.D., Chang, D.T., Hofmann, L.V. & Sze, D.Y.,(2009). Percutaneous implantation of fiducial markers for imaging-guided radiation therapy. *American Journal of Roentgenology*, **192 (4),** 1090-1096.

Koshani, R., Balter, J.M., Hayman, J.A., Henning, G.T.& van Herk, M., (2006). Short-term and long-term reproducibility of lung tumour position using active breathing control (ABC).*International Journal of Radiation OncologyBiologyPhysics,***65(5),**1553–1559.

Kubo, H.D. &Hill, B.C., (1996). Respiration gated radiotherapy treatment: a technical study, *Physics in Medicine and Biology,***41(1),**83-91.

Kupelian, P.A., Forbes, A., Willoughby, T.R., Wallace, K., Manon, R.R., Meeks, S.L., Herrera, L., Johnston, A. & Herran, J.J.(2007). Implantation and Stability of Metallic Fiducials Within Pulmonary Lesions, *International Journal of Radiation Oncology, Biology, Physics,***69(3),** 777-785.

Laurent, F., Latrabe, V., Vergier, B., Montaudon, M., Vernejoux, J. M.&Dubrez, J., (2000). CT-guided transthoracic needle biopsy of pulmonary nodules smaller than 20 mm: results with an automated 20-gauge coaxial cutting needle. *Clinical Radiology,***55,**281–287.

Lung Cancer and Smoking - UK (2007), *CancerStats report*, Cancer Research UK, 61 Lincoln's Inn Fields, London.

Mageras, G.S., Yorke, E., Rosenzweig, K., Braban, L., Keatley, E., Ford, E., Leibel, S.A.& Ling, C.C., (2001). Fluoroscopic evaluation of diaphragmatic motion reduction with a respiratory gated radiotherapy system, *Journal of Applied Clinical Medical Physics,***2(4),**191-200.

Mah, D., Hanley, J., Rosenzweig, K., Yorke, E., Braban, L., Ling, C., Leibel, S. & Mageras, G., (2000). Technical aspects of the deep inspiration breath-hold technique in the treatment of thoracic cancer. *International Journal of Radiation Oncology, Biology, Physics,***48(4),**1175–1185.

Minohara, S., Kanai, T., Endo, M., Noda,K. & Kanazawa, M.,(2000). Respiratory gated irradiation system for heavy-ion radiotherapy.*International Journal of Radiation Oncology, Biology, Physics,***47(4),**1097–1103.

Murphy, M.J., Adler, J.R., Bodduluri, M., Dooley, J., Forster, K., Hai, J., Le, Q., Luxton, G., Martin, D. & Poen, J., (2000). Image-guided radiosurgery for the spine and pancreas. *Computer Aided Surgery,***5(4),**278–288.

Murphy, M.J., Jalden, J., and Isaksson, M., (2002) *Adaptive filtering to predict lung tumor breathing motion during image-guided radiation therapy*. Proceedings of the 16th International Congress on Computer-assisted Radiology and Surgery (CARS 2002), 539–544.

The diagnosis and treatment of lung cancer: Understanding NICE guidance-information for people with lung cancer, their families and carers, and the public (2005). National Institute for Clinical Excellence, CG24 NICE guideline.

Negoro, Y., Nagata, Y., Aoki, T., Mizowaki, T., Araki, N., Takayama, K., Kokubo, M., Yano, S., Koga, S., Sasai, K., Shibamoto, Y. & Hiraoka, M., (2001). The effectiveness of an immobilization device in conformal radiotherapy for lung tumour: reduction of respiratory tumour movement and evaluation of the daily setup accuracy. *International Journal of Radiation Oncology, Biology, Physics,***50(4),**889-898.

Neicu, T., Shirato, H., Seppenwoolde, Y. and Jiang. S.B., (2003). Synchronized moving aperture radiation therapy (SMART): average tumour trajectory for lung patients, *Physics in Medicine and Biology,***48(5),** 587.

Nuyttens, J.J., Prévost, J.B., Praag, J., Hoogeman, M., van Klaveren, R.J., Levendag, P.C. & Pattynama, P.M.,(2006). Lung tumour tracking during stereotactic radiotherapy treatment with the CyberKnife: Marker placement and early results. *Acta Oncologica,***45(7),**961-965.

Nyman, J., Johansson, K.A. &Hultén, U. (2006). Stereotactic hypofractionated radiotherapy for stage I non-small cell lung cancer—Mature results for medically inoperable patients. *Lung Cancer,* **51(1),** 97-103.

Okumura, T., Tsuji, H. & Hayakawam, Y.,(1994). Respiration-gated irradiation system for proton radiotherapy. Proceedings of the 11th International Conference on the Use of Computers in Radiation Therapy, Manchester: North Western Medical Physics Department Christie Hospital, pp 358-359.

Onishi, H., Araki, T., Shirato, H., Nagata, Y., Hiraoka, M., Gomi, K., Yamashita, T., Niibe, Y., Karasawa, K., Hayakawa, K., Takai, Y., Kimura, T., Hirokawa, Y., Takeda, A., Ouchi, A., Hareyama, M., Kokubo, M., Hara, R., Itami, J. & Yamada K. (2004). Stereotactic hypofractionated high-dose irradiation for stage I nonsmall cell lung carcinoma, *Cancer,* **101(7),** 1623 – 1631.

Onishi, H., Kuriyama, K.,Komiyama, T., Tanaka, S., Sano, N., Marino, K., Ikenaga, S., Araki T. & Uematsu, M. (2004).Clinical outcomes of stereotactic radiotherapy for stage I non-small cell lung cancer using a novel irradiation technique: patient self-controlled breath-hold and beam switching using a combination of linear accelerator and CT scanner, *Lung Cance*r,**45(1),** 45-55

Parkin, D.M., Pisani, P.& Ferlay, J., (1999). Global cancer statistics, *CA: A Cancer Journal for Clinicians,***49(1),**33-64.

*Prescribing, recording, and reporting photon beam therapy (Report 62).*1999. International Commission on Radiation Units and Measurements.Washington, DC.

Priban, I.P., (1963). An analysis of some short-term patterns of breathing in man at rest.*The Journal of Physiology,* **166(3),** 425-434.

PutraD., Haas O.C.L., MillsJ.A., Burnham K.J. (2008) A multiple model approach to respiratory motion prediction for real-time IGR Phys. Med. Biol. 53, 1651–1663

Rabiner, L.R., (1975).*Theory and application of digital signal processing,* Prentice Hall, Englewood Cliffs (N.J.).

Remouchamps, V.M., Vicini, F.A.,Sharpe, M.B., Kestin,L.L.,Martinez, A.A.&Wong, J.W., (2003). Significant reductions in heart and lung doses using deep inspiration breath hold with active breathing control and intensity-modulated radiation therapy for patients treated with locoregional breast irradiation. *International Journal of Radiation Oncology, Biology, Physics,***55(2),**392-406.

DeShazer D.J., Breban R., Ott E., and Roy R. (2001) Phys. Rev. Lett.**87**.**4**

Rosenblum M. G., Pikovsky A. S., and Kurths J., (1996)Phys. Rev.Lett. 76, 1804

Ritchie C. J., Hseih J., Gard M. F., Godwin J. D., Kim Y., and Crawford C. R. (1994) Predictive respiratory gating: A new method to reduce motion artifacts on CT scans. *Radiology***190(3)**, 847–852.

Rosenblum M. G., Pikovsky A. S., and Kurths J., (1996)Phys. Rev.Lett. **76**,1804

Rosenzweig, K.E., Hanley, J., Mah, D., Mageras, G., Hunt, M., Toner, S., Burman, C., Ling, C.C., Mychalczak, B., Fuks, Z. & Leibel, S.A., (2000). The Deep Inspiration Breath-hold Technique In The Treatment Of Inoperable Non–small-cell Lung Cancer,*International Journal of Radiation Oncology, Biology, Physics,***48(1),** 81–87.

SchslkoffR.J., (1989).*Digital Image Processing and Computer Vision,* John Wiley & Sons, Chichester.

SchweikardA., Glosser G., Bodduluri M., Murphy M. J., and AdlerJ. R.,

(2000) Robotic motion compensation for respiratory movement during radiosurgery.

Comput. Aided Surg. **5(4)**, 263–277.

Seiler, P.G., Blattmann, H., Kirsch, S., Muench,R. K., Schilling, C., (2000). A novel tracking technique for the continuous precise measurement of tumour positions in conformal radiotherapy, *Physics in Medicine and Biology,***45(9),** N103–N110.

Sentana, E. & Wadhwani, S., (1992). Feedback traders and stock return autocorrelations: evidence from a century of daily data. *The Economic Journal,* **102(411)**, 415–425.

Seppenwoolde, Y., Shirato, H., Kitamura, K., Shimizu, H., Herk, M.V., Lebesque, J.V.& Miyasaka, K., (2002). Precise and Real-Time Measurement of 3D Tumour Motion in Lung due to Breathing and Heartbeat, Measured During Radiotherary, *International Journal of Radiation Oncology, Biology, Physics,***53(4),** 822-834.

Sharp, G. C., Jiang, S.B., Shimizu, S., and Shirato,H. (2004). Prediction of respiratory tumour motion for real-time image-guided radiotherapy. *Phys Med Biol* **49(3)**,425–440.

Shimizu, S., Shirato, H., Ogura, S., Akita-Dosaka, H., Kitamura, K., Nishioka, T., K. Kagei, M. Nishimura, & K. Miyasaka, (2001). Detection of lung tumour movement in real-time tumour-tracking radiotherapy, *International Journal of Radiation Oncology, Biology, Physics,***512,** 304–310.

Shirato, H., Shimizu, S., Kunieda, T., Kitamura, K., van Herk M., Kagei, K., Nishioka, T., Hashimoto, D., Fujita, K., Aoyama, H., Tsuchiya, K., Kudo, K.&Miyasaka, K., (2000). Physical aspects of a real-time tumour-tracking system for gated radiotherapy, *International Journal of Radiation Oncology, Biology, Physics,***48(4),**1187–1195.

Shirato, H., Harada, T., Harabayashi, T., Hida, K., Endo, H., Kitamura, K., Onimaru, R., Yamazaki, K., Kurauchi, N., Shimizu, T., Shinohara, N., Matsushita, M., Dosaka-Akita, H.& Miyasaka, K., (2003). Feasibility of insertion/ implantation of 2.0 mm diameter gold internal fiducial markers for precise setup and real-time tumour tracking in radiotherapy, *International Journal of Radiation Oncology, Biology, Physics,***561,** 240–247.

Shirato, H., Shimizu, S., Shimizu, T., Nishioka, T.& Miyasaka, K., (1999). Realtime tumour-tracking radiotherapy, *The Lancet,***353(9161),** 1331–1332.

Shen, S., Duan, J., Fiveash, J.B., Brezovich, I.A., Plant, B.A., Spencer, S.A., Popple, R.A., Pareek, P.N. & Bonner, J.A., (2003). Validation of target volume and position in respiratory gated CT planning and treatment, *Medical Physics,* **30(12),**3196-205.

Shea, S.A. & Guz, A.,(1992). Personnalite ventilatoire: an overview. *Respiration Physiology*,**87(3),**275-91.

Shirato, H., Shimizu, S., Kitamura, K., Nishioka, T., Kagei, K., Hashimoto, S., Aoyama, H., Kunieda, T., Shinohara, N., Dosaka-Akita, H. & Miyasaka, K., (2000). Four-dimensional treatment planning and fluoroscopic real-time tumour tracking radiotherapy for moving tumour, *International Journal of Radiation Oncology, Biology, Physics,* **48(2),**435-42.

Shirato, H., Shimizu, S., Kunieda, T., Kitamura, K., van Herk, M., Kagei, K, Nishioka, T., ...(2000). Physical aspects of a real-time tumor-tracking system for gated radiotherapy, *International Journal of Radiation Oncology, Biology, Physics,* **48(4),**1187-1195.

Shirato, H.,Suzuki,K., Sharp, G.C., Fujita, K., Onimaru, R., Fujino, M., Kato, N., Osaka, Y., Kinoshita, R., Taguchi, H., Onodera, S. & Miyasaka, K. Speed and amplitude of lung tumor motion precisely detected in four-dimensional setup and in real-time tumor-tracking radiotherapy, *Int J Radiat Oncol Biol Phys,*(2006),**64(4)**, 1229–1236.

Shih, H.A., Jiang, S.B., Aljarrah, K.M., Doppke, K.P. & Choi, N.C., (2004). Internal target volume determined with expansion margins beyond composite gross tumor volume in three-dimensional conformal radiotherapy for lung cancer. *International Journal of Radiation Oncology Biology Physics,* **60(2),** 613-622.

Shimizu, S., Shirato, H., Ogura, S., Akita-Dosaka, H., Kitamura, K., Nish-Ioka, T., Kagei, K., Nishimura, M. &Miyasaka, K., (2001). Detecting of lung tumour movement in real-time tumour-tracking radiotherapy. *International Journal of*

*Radiation Oncology, Biology, Physics,***51(2),** 304–310.

Shimizu, S., Shirato, H., Ogura, S., Akita-Dosake, H., Kitamura, K., Nishioka, T., Kagei, K., Nishimura, M & Miyasaka, K. (2001). Detection of lung tumor movement in real-time tumor-tracking radiotherapy, *International Journal of Radiation Oncology, Biology, Physics,***51(2),** 304–310.

Slotman, B.&Faivre-Finn, C., (2007). Prophylactic Cranial Irradiation in Extensive Small-Cell Lung Cancer. *The New England Journal of Medicine.* **357,**664-672.

Sonke, J., Lebesque, J. & van Herk, M. (2008). Variability of four-dimensional computed tomography patient models. *International Journal of Radiation Oncology Biology Physics,* **70(2),** 500-598.

Starkschall, G., Forster, K.M., Kitamura, K., Cardenas, A., Tucker S.L. & Stevens, C.W., (2004). Correlation of gross tumor volume excursion with potential benefits of respiratory gating, *International Journal of Radiation Oncology Biology Physics,* **60(4),** 1291-1297.

Steenbakkers,R.J., Duppen, J.C., Fitton, I., Deurloo, K.E.I., Zijp, L., Uitterhoeve, A.L.J., Rodrigus, P.T.R., Kramer, G.W.P., Bussink, J., Jaeger, K.D., Belderbos, J.S.A., Hart, A.M., Nowak, P.J.C.M., van Herk, M. & Rasch, C.R.N. (2005). Observer variation in target volume delineation of lung cancer related to radiation oncologist-computer interaction: A "Big Brother' evaluation. *Journal of the European Society for Therapeutic Radiology and Oncology*, **77(2),** 182-190.

Stromberg J., Sharpe M, Kim L., Kini, V., Jaffray, D., Martinez, A. & Wong, J., (2000). Active breathing control (ABC) for Hodgkin's disease: Reduction in normal tissue irradiation with deep inspiration and implications for treatment. *International Journal of Radiation Oncology, Biology, Physics,***48(3),**797–806.

Tortora, G.J.& Derrickson, B., (2006). *Principles of Anatomy and Physiology*, John Wiley & Sons, Hoboken, pp866.

Tobin, M.J., Chadha, T.S., Jenouri, G., Birch, S.J., Gazerroglu, H.B. & Sackner, M.A., (1983a). Breathing patterns. 1. Normal subjects. *Chest,* **84(2),** 202-205.

Tobin, M.J., Chadha, T.S., Jenouri, G., Birch, S.J., Gazerroglu, H.B. & Sackner, M.A., (1983b). Breathing patterns. 2. Diseased subjects,*Chest,***84(3),** 286-294.

Topal, U. & Ediz, B., (2003). Transthoracic needle biopsy: factors effecting risk of neumothorax. *EuropeanJournal of Radiology,* **48(3),**263–267.

Tackling cancer in England: Saving more lives. Report by the comptroller and auditor general. 2004: National Audit Office, London

Tsunashima, Y., Sakae, T., Shioyama, Y., Kagei, K., Terunuma, T., Nohtomi, A. & Akine, Y., (2004). Correlation between the respiratory waveform measured using a respiratory sensor and 3D tumor motion in gated radiotherapy, *International Journal of Radiation Oncology Biology Physics,* **60(3),** 951-958.

Underberg, R.W., Lagerwaard, F.J., Cuijpers, J.P., Slotman, B.J., van Sörnsen de Koste, J.R.& Senan, S., (2004). Four-dimensional CT scans for treatment planning in stereotactic radiotherapy for stage I lung cancer, *International Journal of Radiation Oncology, Biology, Physics,***60(4),**1283-90.

Underberg, R.W.M., van Sörnsen de Koste, J.R., Legarwaard, F.J., Vincent, A., Slotman, B.J. & Senan, S. (2006). A dosimetric analysis of respiration-gated radiotherapy in patients with stage III lung cancer. *Radiation Oncology*, **1(8),** doi:10.1186/1748-717X-1-8.

van Herk M, Remeijer P, Rasch C, Lebesque JV. (2000). The probability of correct target dosage: dose-population histograms for deriving treatment margins in radiotherapy.*International Journal of Radiation Oncology, Biology, Physics*.**47(4)**:1121-35.

van Herk, M., Remeijer, P., Rasch, C. & Lebesque, J.V., (2002). The probability of correct target dosage: Dose–population histograms for deriving treatment margins in radiotherapy, *International Journal of Radiation Oncology, Biology, Physics,***47(4),**1121–1135.

Vedam, S.S., Kini, V.R., Keall, P.J., Ramakrishnan, V., Mostafavi, H. & Mohan, R.,(2003). Quantifying the predictability of diaphragm motion during respiration with a noninvasive external marker. *Medical Physics,***30(4),**505-513.

Vedam, S.S., Keall, P.J., Kini, V.R., Mostafavi, H., Shukla, H.P. & Mohan, R., (2004). Acquiring a four-dimensional computed tomography dataset using an external respiratory signal. *Physics in Medicine and Biology,***48(1),** 45-62.

Vedam, S. S., KeallP. J., DocefA., TodorD. A., Kini V. R., and Mohan R. (2004b) Predictingrespiratory motion for four-dimensional radiotherapy. Med Phys **31(8),** 2274–2283.

Vedam, S.,Docef, A. , Fix, M., Murphy, M., Keall, P. (2005) Dosimetric impact of geometric errors due to respiratory motion prediction on dynamic multileaf collimator-based four-dimensional radiation delivery. *Medical Physics.***32,** 1607-1620

Vedam, S., Archambault, L., Starkschall, G., Mohan, R.&Beddar, S., (2007). Determination of prospective displacement-based gate threshold for respiratory-gated radiation delivery from retrospective phase-based gate threshold selected at 4D CT simulation. *Medical Physics,***34(11),** 4247-4255

Wagman, R., Yorke, E., Ford, E., Giraud, P., Mageras, G., Minsky, B.&Rosenzweig, K., (2003). Respiratory gating for liver tumours: use in dose escalation, *International Journal of Radiation Oncology, Biology, Physics,***5(3),**659-668.

Wilson, E.M., Williams, F.J., Lyn, B.E., Wong, J.W. & Aird, E.G., (2003). Validation of active breathing control in patients with non–small-cell lung cancer to be treated with CHARTWEL. *International Journal of Radiation Oncology, Biology, Physics,* **57(3),**864–874.

Wolthaus J.W., Sonke J.J., van Herk M., Belderbos J.S., Rossi M.M., Lebesque J.V., Damen E.M. (2008) Comparison of different strategies to use four-dimensional computed tomography in treatment planning for lung cancer patients.*International Journal of Radiation Oncology, Biology, Physics.* **70(4)**:1229-38.

Wong, J.W., Sharpe, M., Jaffray, D., Kini, V., Robertson, J., Stromberg, J. & Martinez, A., (1999). The use of active breathing control (ABC) to reduce margin for breathing motion. *International Journal of Radiation Oncology, Biology, Physics,***44(4),**911-919.

Wulf, J., Hadinger, U., Oppitz, U., Olshausen, B. & Flentje, M.,(2000). Stereotactic radiotherapy of extracranial targets: CT-simulation and accuracy of treatment in the stereotactic body frame, *Radiotherapy Oncology,* **57(2),**225-236.

Yorke, E., Rosenzweig, KE., Wagman, R. & Mageras, G.S., (2005). Interfractional anatomic variation in patients treated with respiration-gated radiotherapy. *Journal of Applied Clinical Medical Physics,***6(2),**19-32.

Yu, C.X., Jaffray, D.A.&Wong, J.W.,(1998). The effects of intra-fraction organ motion on the delivery of dynamic intensity modulation, *Physics in Medicineand Biology,* **43,**91–104.

Yuen, S.G., Kesner, S.B., Vasilyey, N.V., Nido, P.J. & Howe, R.D. (2008) 3D Ultrasound-Guided Motion Compensation System for Beating Heart Mitral Valve Repair. *Medical Image Computing and Computer-Assisted Intervention – MICCAI,***5241,** 711-719.

Zhang, T., Keller, H. & O'Brien M.J., (2003). Application of the spirometer in respiratory gated radiotherapy, *Medical Physics,* **44(5),** 1165-1170.

Thank you for reading!